ADVANCED PHYSICS RESEARCH Open Access
www.advphysicsres.com

# Showcasing the Structure and Properties of Lanthanide-Doped $BaTiO_3$

*Takeshi Nakagawa, Melita Menelaou,* and Martina Vrankić**

**Two-dimensional (2D) ferroelectrics, especially lead-free materials such as barium titanate, $BaTiO_3$, hold significant promise for advanced electronics due to their unique nanoscale properties. Doping $BaTiO_3$ with lanthanides (Ln) can enable fine-tuning of electrical and dielectric properties by substituting $Ba^{2+}$ (A-site) or $Ti^{4+}$ (B-site) in the perovskite structure. A-site doping enhances dielectric properties, while doping the B-site changes the polarization and thermal stability. The site preference depends on the ionic radii and charge compensation mechanisms, which include oxygen vacancies and self-compensation processes. This research delivers the structural and microstructural aspects of $BaTiO_3$ doped with members of the Ln family from La to Lu, emphasizing their superior properties compared to undoped $BaTiO_3$. Notably, the Ln dopants significantly influence the ferroelectric, ferromagnetic, luminescent, and piezocatalytic properties, where the ionic radius, doping mechanisms, defect formation, and preparation methods play a role. Theoretical studies and advanced characterization data indicate that Ln dopants improve the performance of $BaTiO_3$ by stabilizing structural defects, affecting site occupancy, and improving insulation resistance. Understanding the defect chemistry and Ln ion distribution in Ln-doped $BaTiO_3$ systems can help optimize their functional properties for next-generation technologies and sustainable energy applications.**

## 1. Introduction

Because of their unique features on the nanoscale, two-dimensional (2D) ferroelectrics hold great promise for the electronics of the future. In general, 2D materials are a type of nanomaterial with a sheet-like structure and a high lateral size-to-thickness ratio.[1,2] The extraordinary physical and chemical features of 2D materials, such as their huge surface area and abundance of active sites, result from the confinement of electrons in two dimensions. As a result, 2D materials have become a bright spot in a number of industries, including electronics, energy storage, and catalysis.[3–6] Compared to 3D materials, low-dimensional materials (e.g., nanowires, nanosheets, nanorods) respond more strongly to weak mechanical energy and can generate a much higher piezoelectric potential under the same load.[7] This feature makes them particularly suitable for enhanced piezocatalytic performance. As a subclass of ferroelectrics, 2D lead-based piezoelectrics such as $Pb(Zr,Ti)O_3$ (PZT) are still very popular. However, the high concentration of hazardous lead severely restricts their commercial use in many countries. For this reason, various lead-free alternatives have been proposed, including barium titanate, $BaTiO_3$ (BTO). In order to achieve piezoelectric performance comparable to of leaded counterparts, many successful modification processes, such as doping and texturing, have been developed.[7] Through doping and phase engineering, the piezoelectric coefficient $d_{33}$ of BTO-based ceramics can be increased to 620 pC $N^{-1}$, which is equivalent to that of high-end PZTs.[8] Furthermore, its single-crystal form is expected to have a $d_{33}$ value of 1500 – 2000 pC $N^{-1}$, making it a promising candidate for piezoelectric devices. Dopants can narrow the band gap by introducing defective energy levels, providing more opportunities for electron excitation.[9,10] Additionally, some dopants improve the conductivity of the material and promote charge transfer at the interface.[11] Dopants can also cause local crystal deformation and reduced symmetry, resulting in increased piezoelectricity.[12] In addition, doping often leads to the formation of oxygen vacancies ($O_v$), which play a dual role in influencing the piezocatalytic properties of BTO.[13,15] On the one hand, $O_v$ defects introduce defective energy levels, which lower the energy required for charge carrier formation, and increase

T. Nakagawa
Center for High Pressure Science and Technology Advanced Research
10 Xibeiwang East Road, Haidian District, Beijing 100094, P.R. China
M. Menelaou
Department of Mechanical Engineering and Materials Science and Engineering
Cyprus University of Technology
30 Arch. Kyprianos Str., Limassol 3036, Cyprus
E-mail: melita.menelaou@cut.ac.cy
M. Vrankić
Division of Materials Physics
Ruđer Bošković Institute
Bijenička 54, Zagreb 10000, Croatia
E-mail: mvrankic@irb.hr

The ORCID identification number(s) for the author(s) of this article can be found under https://doi.org/10.1002/apxr.202500006



**DOI: 10.1002/apxr.202500006**

the charge carrier concentration.[16,17] On the other hand, they contribute to enhanced piezocatalytic performance by facilitating charge separation and transfer at the material interface.

BTO is an important target for 2D ferroelectrics, but the controlled synthesis of 2D BTO nanosheets, for example, is still a challenge. Hagiwara et al. demonstrated a simple solvothermal method to synthesize molecularly thin tetragonal BTO nanosheets from 2D $Ti_{0.87}O_2$ nanosheets.[18] The researchers successfully synthesized tetragonal BTO nanosheets with controlled thicknesses from 1.4 to 3.0 nm and investigated their ferroelectric properties up to the critical thickness. Notably, the study shows that 2D BTO nanosheets with water absorption exhibit bulk-like ferroelectricity at a thickness of 1.8 nm. Evidently, to reduce the thickness of the dielectric layers, the size of the BTO particles must be reduced. Submicron BTO particles have been synthesized by various techniques, including solid-state reactions, hydrothermal and solvothermal processes, microwave-assisted heating, flame spray pyrolysis, and sol-gel methods.[19–24] While these approaches produce BTO with different morphologies and topologies, they often result in low tetragonality. This is significant as tetragonal BTO ceramics exhibit superior dielectric properties compared to cubic ceramics – a phenomenon that is well-documented in the literature, although the underlying mechanisms remain the subject of ongoing debate.[25–27] In general, the dielectric constant of sintered BTO decreases with increasing average grain size.[9,28–30] As the particle size decreases, the dielectric constant also decreases. Thus, to compensate for this loss, in addition to the obvious effects of the synthesis methods on the dielectric characteristics, the doping of BTO with rare-earth (RE) elements has been intensively explored. In particular, different sintering temperatures and holding times lead to unique microstructures characterized by different grain sizes and morphologies, resulting in different dielectric, ferroelectric, and piezoelectric responses of the materials. This is why the complex (micro)structure-property correlation in materials must be adequately addressed in order to develop intelligent systems. The addition of donor dopants above the threshold concentration (0.2 ± 0.5 at%), which marks the transition between semiconductor and insulator, significantly limits grain development. In heavily doped ceramics, the grain size can be less than 1 mm. Therefore, the influence of grain/particle size on the crystal structure of BTO must be considered as a by-product of doping. It is well known that when the grain size of dense polycrystalline BTO is less than 0.7 mm, the structure changes from tetragonal to pseudocubic at RT.

The RE elements include the lanthanides together with yttrium (Y), scandium (Sc), and lanthanum (La). The lanthanides are a group of 15 elements from the periodic table with atomic numbers 57–71: lanthanum (La), cerium (Ce), praseodymium (Pr), neodymium (Nd), promethium (Pm), samarium (Sm), europium (Eu), gadolinium (Gd), terbium (Tb), dysprosium (Dy), holmium (Ho), erbium (Er), thulium (Tm), ytterbium (Yb), and lutetium (Lu). While most of these elements occur naturally, Pm is mainly formed as a by-product of radioactive decay. Due to their similar physiochemical properties, La, Sc, and Y are often associated with RE elements in mineral deposits. These elements are further subdivided into light Ln elements (atomic numbers 57–63: La, Ce, Pr, Nd, Pm, Sm, and Eu) and heavy Ln elements (atomic numbers 64–71: Gd, Tb, Dy, Ho, Er, Tm, and Yb).

BTO offers considerable flexibility within its perovskite $ABO_3$ structure, allowing the incorporation of various dopants. A-site doping, where common elements such as $La^{3+}$, $Al^{3+}$, $Bi^{3+}$, $Ce^{3+}$, $Pr^{3+}$, $Nd^{3+}$, and $Sm^{3+}$ replace $Ba^{2+}$, enables precise tuning of the physical and electrical properties of the material.[31] By selecting suitable A-site dopants and optimizing their concentrations, BTO can be tailored for a wide range of applications, including electronics, sensors, and energy-related technologies. However, to achieve the desired material properties and ensure stability, the doping process must be carefully controlled.[32] B-site doping involves the substitution of various elements at the $Ti^{4+}$ sites within the BTO lattice. The B-site dopants in particular can significantly alter the polarization behavior and Curie temperature ($T_c$) of BTO. Several aliovalent cations – including $Zn^{2+}$, $Cu^{2+}$, $Mg^{2+}$, $Mn^{2+/3+}$, $Fe^{2+/3+}$, $Ni^{3+}$, $Cr^{3+}$, $Co^{3+}$, $Sc^{3+}$, $Ga^{3+}$, $In^{3+}$, $Y^{3+}$, $Ho^{3+}$, $Dy^{3+}$, $Yb^{3+}$, $Nb^{5+}$, $Sb^{5+}$, and $W^{6+}$, can enter the B-sites, providing a versatile route to tailor the material properties.[31,33–35] In general, B-site doping affects the electrical properties of BTO and has a significant impact on thermal stability and phase transition behavior, improving stability and performance at elevated temperatures.[36] It is important to recognize the challenges and limitations associated with B-site doping. Precise regulation of dopant components, dopant concentrations and doping sites is essential to achieve optimal material performance and stability.

A comprehensive study is still needed to systematically investigate how the changes in charge balance mechanisms affect the electrical, dielectric and structural properties of Ln-doped BTO. Although BTO can be doped at both the A- and B-sites, specific criteria must be considered to determine the most suitable dopant for each site.[37,38] In BTO, divalent and trivalent ions with large ionic radii, and monovalent ions, usually replace $Ba^{2+}$ at the A-site. In contrast, divalent and trivalent ions with smaller ionic radii, and with tetravalent, pentavalent, and hexavalent ions, are usually introduced at the B-site to replace $Ti^{4+}$.[39–42] The terms "large" and "small" are defined relative to the ionic radii of $Ba^{2+}$ (1.61 Å, coordination number (CN) = 12) and $Ti^{4+}$ (0.605 Å, CN = 6).[43] According to Lu et al., the best-performing Y5 V ceramics (La- and Ce-doped BTO ceramics with compositions $x$ = 0.03–0.04, $y$ = 0.05) exhibited a maximum dielectric constant of more than 1000 over the frequency range of 1–100 kHz by co-doping BTO with $La^{3+}$ and $Ce^{3+}$.[44] Dunbar et al. investigated the site replacement of different Ln dopants in BTO using theoretical predictions and EPR measurements.[45] Their study identified $Yb^{3+}$ as a stable B-site dopant, independent of the Ba/Ti ratio, and $Dy^{3+}$ as an amphoteric B-site dopant, based on signal intensity behavior. $Gd^{3+}$ was confirmed as an amphoteric dopant, while $Eu^{2+}$ preferentially occupies the A-site. Furthermore, $Ce^{3+}$ was shown to act primarily as a dopant for the A-site, as its signal strength depends on the Ba/Ti ratio. When Ce was forced to occupy the B-site, it likely shifted to a $Ce^{4+}$, making it EPR-silent. Although EPR spectra were obtained for $Nd^{3+}$ and $Er^{3+}$, the site occupancy could not be definitively assigned based on these spectra alone, and no EPR signal was observed for Sm-doped BTO. In general, the metal vacancies correlate with the preferred position of the dopant: samples with A-site dopants (i.e., Ce, Nd, and Sm) have more $Ti^{4+}$ vacancies and fewer $Ba^{2+}$ vacancies than those with amphoteric dopants (i.e., Er and Dy). The permittivity of Ln-doped BTO is closely related to structural distortions and chemical defects surrounding the dopants.

The crystal structure and microstructure of BTO can be significantly altered even by low concentrations of dopant ions of different sizes. Many studies have investigated Ln-doping of BTO to improve its desired properties and thus expand its application potential in a variety of advanced technologies.[46–61] The Ln-doped BTO has attracted significant interest among researchers due to its improved electrical properties with $T_C$ values that can be found at lower temperatures.[39,44,62–65] Doping enables precise tuning of the electrical properties of BTO, and the incorporation of Ln has been shown to improve the performance of BTO-based multilayer ceramic capacitors (MLCCs) by increasing $T_c$, as a function of doping concentration. In addition, Ln doping stabilizes the vacancies in BTO, improving both the performance and reliability as well as the insulation resistance and lifetime of MLCCs.[66,67] Preventing grain growth, improving the temperature dependence of the dielectric constant, and improving reliability as resistance degrades are all properties required for MLCCs and high dielectric constant capacitors, and donor-type rare earths have proven their utility in these areas.

The effect of Ln-doping on the dielectric constant of BTO is still a topic of debate. Some studies report that Ln-doping significantly increases the dielectric constant, while others show lower dielectric constants. For example, $Er^{3+}$-doping was found to increase the dielectric constant of BTO while improving the capacitance.[66] In contrast, $Er^{3+}$-doping was also shown to decrease the dielectric constant of BTO ceramics. With increasing the $Er^{3+}$ concentration, the dielectric constant decreases significantly at 300 K.[68,69]

Most theoretical studies on Ln-doped BTO have focused on Ln selectivity and the interactions between Ln dopants and structural defects such as vacancies. A density-functional theory (DFT) study by Moriwake et al.[70] showed that the site selectivity of $Dy^{3+}$ and $Ho^{3+}$ depends on the thermodynamic conditions. With an excess of $Ba^{2+}$, the Ln dopants occupy $Ti^{4+}$ sites and are compensated, whereas with an excess of $Ti^{4+}$, they preferentially occupy $Ba^{2+}$ sites; the excess charge is compensated by the formation of electron carriers. Under reducing conditions, both $Dy^{3+}$ and $Ho^{3+}$ exhibit the same site preference with similar compensation mechanisms and low solution energy. Honda et al. further demonstrated that Ln dopants stabilize near the first and second closest $O^{2-}$ sites at the $Ba^{2+}$ and $Ti^{4+}$ positions, respectively.[71] More recently, a DFT study by Cheng et al. revealed that $La^{3+}$ and $Sm^{3+}$ occupy only $Ba^{2+}$ sites, while $Dy^{3+}$, $Ho^{3+}$, $Y^{3+}$, and $Yb^{3+}$ exhibit amphoteric behavior.[72] Larger $Ln^{3+}$ ions cannot be trapped, leading to a mismatch between binding energy and site occupancy. The effects of Ln-doping on dielectric constants and the local atomic structure of Ln-doped BTO remain an open question. Lee et al. have addressed this gap using first-principles calculations based on DFT and density-functional perturbation theory to investigate the microscopic structure and dielectric properties of Ln-doped BTO.[73] Ln dopants that are significantly removed from $Ba^{2+}$ sites for charge compensation, lead to off centre structures and this shift is more pronounced for elements with smaller ionic radii. Changes in the ionic dielectric constant are closely related to the Ln displacement and ionic radius. Wang et al. prepared pure and $La^{3+}$-doped BTO fibers by electrospinning which yielded fiber ceramics with low dielectric loss and high dielectric constant at low frequencies as well as a high tetragonal phase.[74]

To elucidate the complex physical and chemical properties of Ln-doped BTO materials, a comprehensive understanding of their structural and microstructural features is essential. The positions of the doping sites in BTO have been determined using a number of techniques, including electron paramagnetic resonance/electron spin resonance (EPR/ESR),[45,75,76] conductivity measurements, X-ray diffraction (XRD)[39,65,67,77,78] atomistic simulations,[79,80] and luminescence.[81] In addition, the mechanisms of Ln-doping and the defect chemistry of Ln-doped BTO have been studied separately in a number of papers.

Theoretical simulations based on tolerance factors have shown that the ion occupation correlates with the ion radius.[82,83] Larger Ln ions such as $La^{3+}$ (1.36 Å, CN = 12) and $Nd^{3+}$ (1.27 Å, CN = 12) prefer substitution on the A-site ($Ba^{2+}$), while smaller ions, such as $Yb^{3+}$ (0.868 Å, CN = 6), prefer the B-site ($Ti^{4+}$). Intermediate ions such as $Y^{3+}$ (0.9 Å, CN = 9) and $Er^{3+}$ (0.89 Å, CN = 6), can occupy both the A- and B-sites.[34,65,78,84–87] Specific doping also leads to chemical inhomogeneity. For example, partial replacement of the A-site by $La^{3+}$ can lead to Ti vacancies or Ti reduction.[88] These imperfections can significantly affect the dielectric properties of BTO-based ceramics. Guillemet-Fritsch et al. achieved a RT colossal permittivity in spark plasma-sintered $Ba_{0.95}La_{0.05}TiO_{3-x}$ ceramics, where $Ti^{3+}/Ti^{4+}$ acted as polaron carriers.[89] Chemical inhomogeneity often occurs alongside specific doping. For example, partial substitution of the A-site by $La^{3+}$ can lead to the formation of Ti vacancies or the reduction of Ti.[90] Low concentrations of Ln dopants can cause local atomic displacements in BTO, which can be computationally simulated. Local structural models developed computationally provide extremely useful information to rationalize experimental structural models obtained from ensemble data. Freeman et al. developed a model that captures the structural and kinetic features of BTO, and provides a self-consistent potential model for analyzing the energetics of defect chemistry in BTO.[91] The model was tested by simulating Ln-doping and considering five possible charge compensation schemes. These simulations were consistent with experimental studies and predicted that small Ln dopants preferentially substitute at the Ti-site, medium-sized Ln dopants occupy both Ti and Ba-sites, and larger Ln dopants exclusively favor the Ba-site. The calculations also indicate that electron compensation for Ba-site substitution is energetically less favorable than the creation of Ti vacancies. Buscaglia et al. found that Ln substitution in the BTO host lattice requires a compensatory mechanism to address the excess charge when replacing a $Ti^{4+}$ or the loss of charge when replacing a $Ba^{2+}$. Overall, these results have major implications for further scientific research in this area. Five alternative compensation schemes[80] are known in the literature (Schemes 1 − 5):

1. Substitution of $M^{3+}$ for $Ba^{2+}$ with conduction electron compensation:

$$M_2O_3+2Ba_{Ba} \rightarrow 2M^{\cdot}_{Ba}+1/2O_2+2e'+2BaO \quad (1)$$

$$2M_2O_3+4Ba_{Ba}+Ti_{Ti} \rightarrow 4M_{Ba} + V''''_{Ti}+3BaO + BaTiO_3 \quad (2)$$

3. Substitution of $M^{3+}$ for $Ti^{4+}$ with $O^{2-}$ vacancy compensation:

$$M_2O_3+2Ti_{Ti} + O_O \rightarrow 2M'_{Ti}+V^{\bullet\bullet}_O+2TiO_2 \quad (3)$$

4. Substitution of $M^{3+}$ for $Ba^{2+}$ and $M^{3+}$ for $Ti^{4+}$, which leads to self-compensation:

$$M_2O_3+Ba_{Ba}+Ti_{Ti} \rightarrow M_{Ba} + M'_{Ti}+BaTiO_3 \quad (4)$$

5. Substitution of $M^{3+}$ for $Ba^{2+}$ with $Ba^{2+}$ vacancy:

$$M_2O_3+3Ba_{Ba} \rightarrow 2M^{\bullet}_{Ba} + V''_{Ba}+3BaO \quad (5)$$

Both experimental and theoretical studies have shown that smaller Ln dopants such as $Lu^{3+}$ and $Yb^{3+}$, exclusively replace Ti atoms, with the charge being compensated by oxygen vacancies.[39,65] Simulations have indicated that Scheme 3 (see above) with $RE_{Ti}$ defects has an energy about 0.1 eV lower than the other schemes for the small RE ions. In contrast, the simulations of Lewis and Catlow,[92] and Buscaglia et al.[80] predicted self-compensation (i.e., Scheme 4) at this location using Ln dopants at both the Ti and Ba-sites. The medium-sized Ln ions, such as $Ho^{3+}$, $Eu^{3+}$, and $Gd^{3+}$, tend to substitute at both the Ti and Ba-sites, with the self-compensation scheme taking precedence.[92,93] The simulations agree and show that Scheme 4 is energetically more favorable for these three ions. The position of the RE ion is often determined by certain conditions, such as the sintering environment or the ion concentration; for example, the Ba/Ti ratio has a significant influence on the occupancy of the Gd site.[94] Previous classical simulations suggest that the self-compensation approach requires less energy for medium-sized Ln ions such as Gd. Theoretical simulations by Moriwake et al. did not consider incorporating self-compensation, but nevertheless showed, that depending on the environment, Ho can substitute either at the Ti-site, leading either to the formation of holes or oxygen vacancies, or at the Ba-site, leading to electron compensation and barium vacancies.[70] Simulations showed that Scheme 2 is the most energy-efficient, while Scheme 1 is the least efficient. For larger Ln ions, however, Scheme 1 proves to be more advantageous. The debate about the compensating mechanism for Ba substitution persisted, especially at low Ln concentrations. Furthermore, theoretical calculations showed the La substitution at the Ba-site in all situations except in the Ti-$TiO_2$ environment, where La-doping is energetically equivalent at both sites. Under oxidizing conditions, La compensation is achieved by creating Ti vacancies, while electron compensation is preferred in reducing environments. This is consistent with experimental reports on the two alternative compensation strategies.

The ability to accurately describe the defect chemistry and solid solutions of perovskites using classical methods opens the door to exploring a wide range of complicated systems and predicting the possible properties of many perovskite systems, which will be invaluable for future research. Understanding the defect chemistry of Ln-doped BTO systems and investigating the distribution of Ln ions in the BTO host is a long-standing problem in the field of functional perovskite oxides.[39,84] To accurately understand the distribution and influence of Ln ions in the BTO lattice, it is important to determine the preferred dopant site (Ba or Ti), the solubility limit at each site, and the influence of Ln concentration on these factors. An important aspect is to understand the atomic arrangement around the Ln ions and the neighboring BTO host ions, as well as the defects caused by charge-compensation mechanisms (e.g., cation and anion vacancies). However, investigating these features by experiments alone is challenging, due to low dopant concentrations and local distortions caused by mismatches in ion size and charge between the Ln ions and the $Ba^{2+}/Ti^{4+}$ host ions.

In this review, the effects of Ln incorporation into the BTO host on the structural and microstructural properties are closely correlated with the dielectric, ferroelectric, and piezoelectric properties of Ln-doped BTO-based materials. The primary goal of this review is to deliver tailored collection of research results to meet the needs of various research groups conducting both fundamental and applied research in the field of Ln-doped BTO chemistry.

## 2. Crystal Features of BTO Host

Depending on the temperature, BTO adopts different crystal structures. Its polymorphs show cubic, tetragonal, orthorhombic, rhombohedral, and hexagonal forms, which vary from high to low temperature (**Figure 1**).[95–103] With the exception of the cubic and hexagonal forms, which are paraelectric and have no polarization, all these phases exhibit ferroelectricity. With increasing temperature, BTO undergoes successive phase transitions from ferroelectric to paraelectric states, as shown in Figure 1. BTO has the classic $ABO_3$ perovskite structure (space group (s. g.) $Pm\text{-}3m$ , $a$ = 4.01914(1) Å, $\alpha = \beta = \gamma = 90°$, $V$ = 64.92 Å$^3$), with $Ba^{2+}$ at the A-site, $Ti^{4+}$ at the B-site, and $O^{2-}$ at the face centers as can be seen in Figure 1.[104,105] In the high-temperature cubic phase, $TiO_6$ octahedra share the corners to form a cubic network with oxygen vertices and Ti–O–Ti edges. At lower temperatures, phases with lower symmetry stabilize, causing the $Ti^{4+}$ to shift to off-center positions, which enhances the unique properties of the BTO lattice through the synergistic effects of $Ti^{4+}$ distortions.[106] As the temperature decreases, the cubic BTO undergoes successive phase transitions into three different ferroelectric phases (Figure 1). At −90 °C, BTO transitions from the paraelectric to the ferroelectric phase and adopts a tetragonal structure (s. g. $P4\,mm$, $a$ = 4.0149(3) Å, $\alpha = \beta = \gamma = 90°$, $V$ = 64.72 Å$^3$), but remains orthorhombic (s. g. $Amm2$, $a$ = 4.0094(3) Å, $b$ = 5.6214(9) Å, $c$ = 5.6386(3) Å, $\alpha = \beta = \gamma = 90°$, $V$ = 127.09 Å$^3$) between 4 °C and −90 °C and finally becomes rhombohedral (s. g. $R3mR$, $a$ = 4.0035(4) Å, $\alpha = \beta = \gamma = 89.84°$, $V$ = 64.17 Å$^3$ below −90 °C.[95,100,107] (Figure 1a,b). Each distortion can be considered as an extension of the cubic unit cell along certain directions: along an edge in tetragonal symmetry (i.e., [001] direction), along a face diagonal in orthorhombic symmetry (i.e., [011] direction) or along a body diagonal in rhombohedral symmetry (i.e., [111] direction). In these ferroelectric phases, the spontaneous polarization arises from the relative motion between the centers of negative ($O^{2-}$) and positive ($Ba^{2+}$ and $Ti^{4+}$) ions or the tilting of oxygen octahedra, which occurs without an external electric field or mechanical force.

BTO particles with a tetragonal structure have long been used as raw material for electrical devices. Since the 1970s, size and scaling effects in ferroelectric materials have sparked attention among researchers in nanoscience and nanotechnology. This interest has been driven by two main factors. The first is the fundamental question of whether there is a threshold size for ferroelectricity or whether ferroelectric order decreases due to confinement to a small volume. For epitaxial thin films, the critical thickness is 2–3 nm, while for ceramics the critical grain

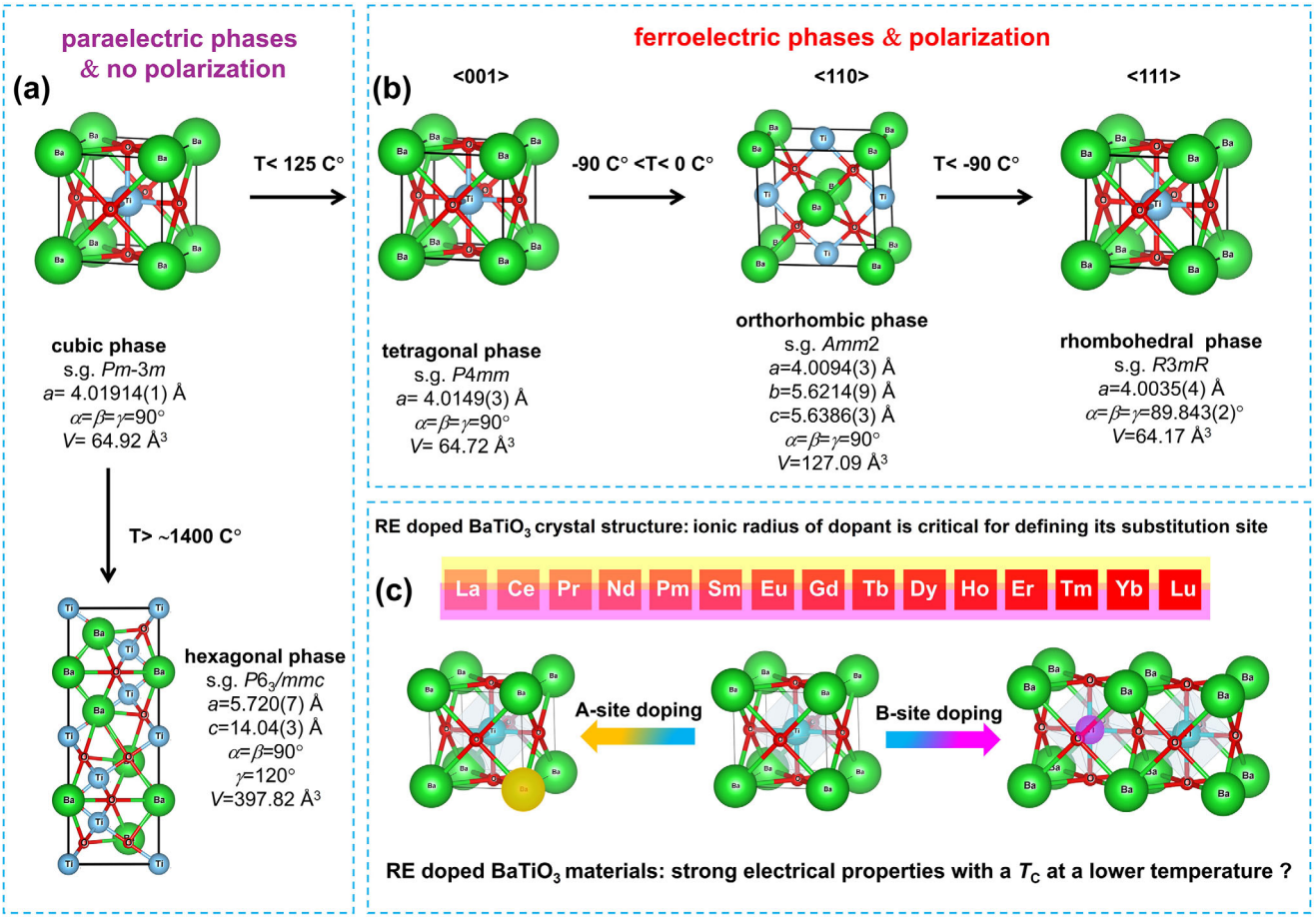


**Figure 1.** a) The cubic symmetry (s. g. *Pm*-3*m* ) of BTO defines an ideal perovskite structure.[105] The cubic phase transforms into a high-temperature hexagonal structure (s. g. $P6_3mmc$, above ≈1400 °C.[95] b) phase transition to a ferroelectric tetragonal symmetry (s. g. *P*4 *mm*) occurs at a temperature decrease, while further decrease leads to the formation of orthorhombic (s. g. *Amm*2) and rhombohedral phases (s. g. *R*3*mR*), and c) schematic representation of the substitution sites in Ln-doped BTO structures.[95,100,107]

size is 10–20 nm.[108–110] The miniaturization of electrical devices makes it necessary to reduce the size of components. This requires BTO particles with a size between 20 and 300 nm, which have a high dielectric constant. As the BTO particles become smaller, the unit-cell volume of tetragonal BTO increases.[97–99] For example, when the particle size is reduced from 430 to 140 nm, the $c/a$ ratio decreases and the particle size approaches a critical size at which the $c/a$ ratio becomes one. This shift probably explains the observed increase in the dielectric constant, which rises from 1550 to 5000 when the particle size is reduced from 430 to 140 nm. The ferroelectric order in materials is also significantly influenced by the particle shape.[108,111] Morozovska et al. predicted that elongated nanowires can maintain or even induce ferroelectricity at very small diameters compared to spherical particles of the same size, because the depolarizing field disappears and the surface tensions in nanowires are very high.[111] In contrast, the hexagonal structure of BTO is not ferroelectric (Figure 1a, bottom), and has a unit cell of six BTO units (s. g. $C6_3/mmc$, $a = 5.735$ Å, $c = 14.05$ Å, $\alpha = \beta = 90°$, $\gamma = 120°$, $V = 397.82$ Å$^3$).[112] It consists of six close-packed layers of $Ba^{2+}$ and $O^{2-}$, each layer containing one $Ba^{2+}$ for every three $O^{2-}$ in an ABCACB packing order.

The $Ti^{4+}$ occupies octahedral vacancies between these layers, and two-thirds of the $TiO_6$ octahedra are present in pairs that share a face and form $Ti_2O_9$ coordination groups. The compensatory distortion in the $Ti_2O_9$ groups increases the Ti–Ti distance by 0.33 Å, and decreases the O–O distance on the shared face by 0.38 Å. In general, various experiments continue to focus on decreasing the thickness of the dielectric layers, while increasing their dielectric constants.[113,114] A literature review shows that most studies in the Ln series focus on La-doped BTO. As the atomic number in the Ln series of the periodic table increases, the number of published articles based on the Scopus metrics decreases (**Figure 2**). The exceptions are promethium, Pr a radioactive and extremely rare element, and lutetium, Lu the last element in the Ln series, which is also the first element of the 6th-period transition metal.

### 2.1. The Case of La-Doped BTO

Lanthanum, La is undoubtedly the most studied dopant of the BTO host in the Ln series. Due to the grain size of the Ln-doped BTO, $La^{3+}$ is the most preferred. Compared to other Ln-doped

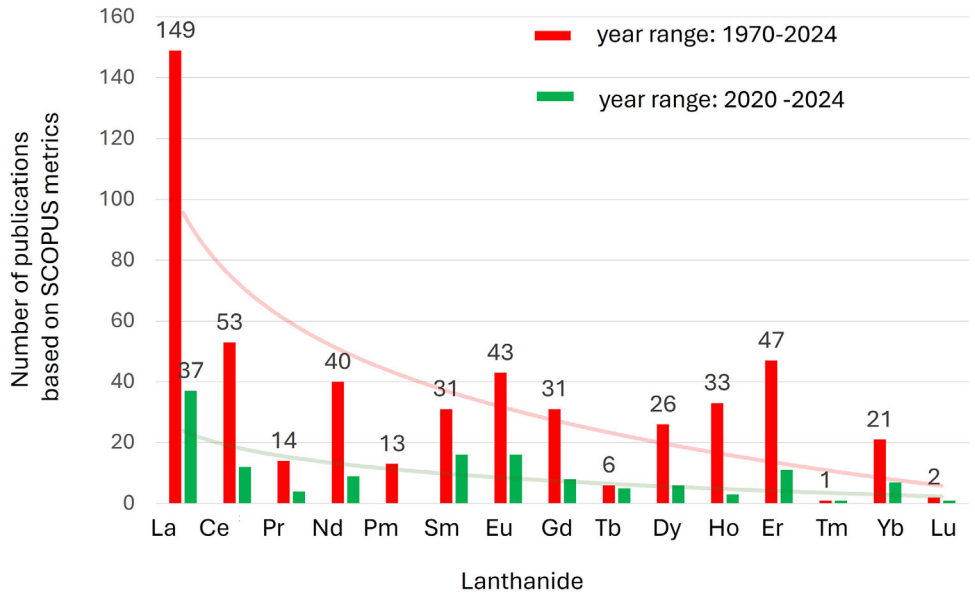


**Figure 2.** Number of publications on Ln-doped BTO based on Scopus metrics, divided into two data sets. Publications on Ln-doped and Ln-codoped BTO and BTO-based materials, are covered.

BTO samples the La-doped BTO has the smallest average grain size.[114] $La^{3+}$ in particular has an ionic radius almost equal to that of $Ba^{2+}$, which reduces lattice distortion and facilitates grain growth during sintering. Namely, the $La^{3+}$ replaces $Ba^{2+}$ over a wide range of doping levels compared to $Ti^{4+}$ as their ionic radii are similar. The concentration of $La^{3+}$ leads to a critical threshold beyond which the material changes from a semiconductor to an insulator. Specifically, in La-doped BTO, the resistivity reaches a minimum at ≈0.3 mol% La, with the transition from semiconducting to insulating properties occurring beyond 1.0 mol%.[87] This behavior is associated with charge-compensation mechanisms in which $La^{3+}$ replaces $Ba^{2+}$. In addition, the electrical properties of Ln-doped BTO, are sensitive to the level of doping. For example, studies have shown that BTO remains a semiconductor up to an Ln-doping of ≈0.3 at.% but becomes an insulator at higher concentrations. Various explanations have been provided for this behavior. MacChesney et al. attributed this to the occurrence of different defect configurations in different compositional regimes.[115] It was postulated that the charge compensation up to 0.25 at.% RE addition to BTO occurs by the conversion of $Ti^{4+}$ to $Ti^{3+}$, and beyond that by the formation of barium vacancies, as follows:

$$BaTiO_3 + xLa_2O_3{\times}TiO_2 \rightarrow Ba_{Ba} + 2xLa^{\bullet}_{Ba} + Ti_{Ti} + 2xTi'_{Ti} + (3+6x)\,O_o + (x/2)\,O_2 \quad (6)$$

$$BaTiO_3 + xLa_2O_3{\times}TiO_2 \rightarrow Ba_{Ba} + 2xLa^{\bullet}_{Ba} + xV''_{Ba} + (1+3x)\,Ti_{Ti} + (3+9x)\,O_o \quad (7)$$

Chan and Smyth proposed the following reactions for low and high doping levels, respectively:[118]

$$2La_2O_3 + 4TiO_2 \rightarrow 4La^{\bullet}_{Ba} + 4Ti_{Ti} + 12O_o + O_2 + 4e' \quad (8)$$

$$2La_2O_3 + 6TiO_2 \rightarrow 4La^{\bullet}_{Ba} + 6Ti_{Ti} + 18O_o + 2V''_{Ba} + 4e \quad (9)$$

Early research focused on minimal doping levels due to the excellent semiconducting properties of weakly doped materials and their temperature-dependent resistivity, which made them valuable for thermistor applications. The defect structures were mainly suspected at this stage. Saburi, for example, investigated the effects of minimal additions of Pr, Sm, Bi, Ce, Ta, Nb, Nd, Sb, La, and Ta on the electrical properties of BTO and suggested that Ln ions occupy the Ba-site.[116] In this model, charge compensation is achieved by a transition of Ti ions from the 4+ oxidation state to the 3+ oxidation state. However, significantly fewer studies have characterized the defect structure of BTO at higher doping levels.[117–119] Eror and Smyth proposed that in the reduced state, $La^{3+}$ occupies the $Ba^{2+}$ sites, with charge compensation occurring through the $Ti^{3+}$ formation. It has been shown that barium and titanium vacancies can form upon absorption of oxygen, that the donor dopant can shift within the cation site or that barium vacancies can form, leading to the precipitation of BaO.[118] Today, it is generally assumed that semiconducting La-doped BTO (< 0.3 mol% La) involves electronic charge compensation, releasing electrons, whereas insulating La-doped BTO (> 0.3% La) is associated with Ti vacancies.[86,120–123]

Nevertheless, further studies were required to systematically investigate the relationship between the changes in charge compensation mechanisms and the associated electrical, dielectric, and structural properties of La-doped BTO. The doping of BTO with donor ions can change the oxidation state of $Ba^{2+}$, making it semiconducting at room temperature (RT).[124] In $La^{3+}$-doped

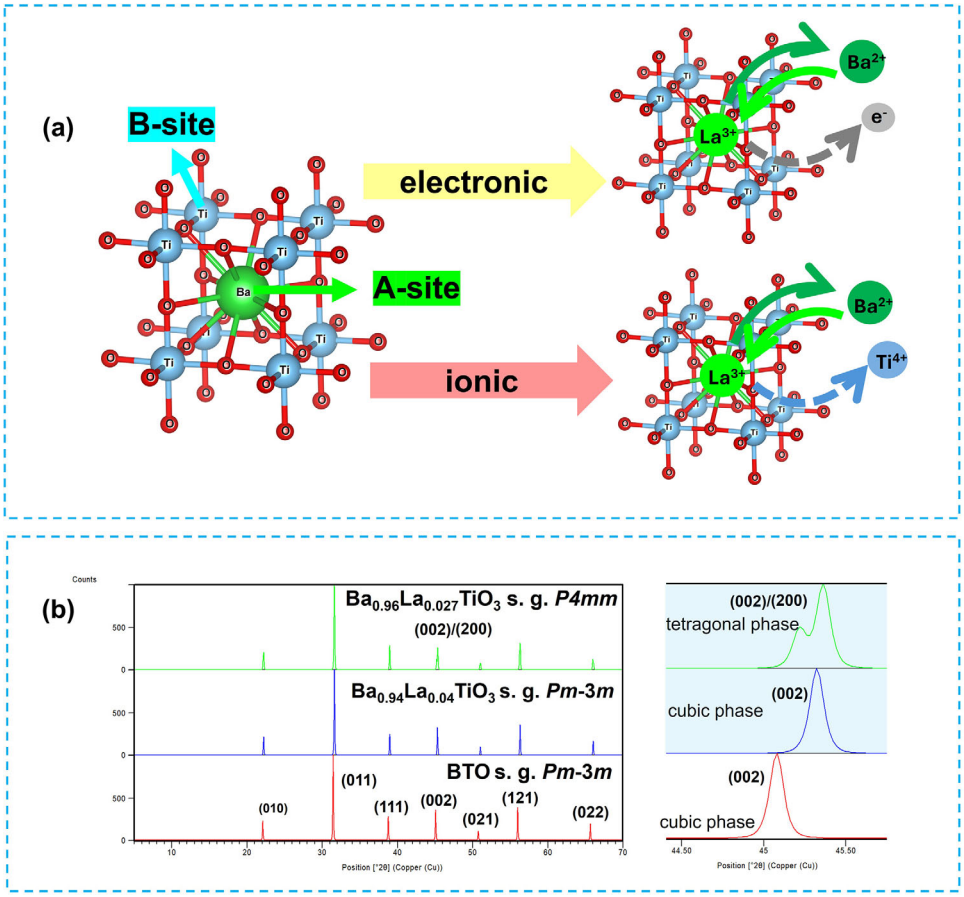


**Figure 3.** a) The potential charge compensation mechanisms based on the La-doping level and b) the shift and combination of (002) and (200) reflections showing the crystal structure gradually transforms from tetragonal to cubic as La-doping concentration increases.[134,135]

BTO, where $La^{3+}$ occupies the A-site ($Ba^{2+}$ sites), the main charge compensation mechanism shifts from electronic to ionic with increasing doping concentration, leading to changes in the volume of the unit cell (**Figure 3a**).[86,125] At low La-doping concentrations, the substitution of $Ba^{2+}$ by $La^{3+}$ at the A-site leads to additional holes, which are balanced by the release of electrons, as shown in Equation (10):

$$2La_2O_3+2TiO_2 \rightarrow 2La^{\bullet}_{Ba}+2Ti^{x}_{Ti}+6O^{X}_{O}+1/2O_2+2e' \quad (10)$$

$$2La_2O_3+3TiO_2 \rightarrow 4La^{\bullet}_{Ba}+3Ti^{x}_{Ti}+V''''_{Ti}+12O^{X}_{O} \quad (11)$$

When the $La^{3+}$-doping concentration exceeds a certain threshold, Ti vacancies are formed instead of free electrons (Equation 11).[126] $La^{3+}$ replaces $Ba^{2+}$ regardless of La-doping level; however, the resistivity changes due to different charge compensation processes.[127] According to Equations (10) and (11), the resistivity in La-doped BTO decreases at low La-doping levels due to electron compensation, while it increases at higher levels due to the formation of Ti vacancies.[128] At low La-doping levels, the charge is balanced before the resistance increases by adding more electrons at the $La^{3+}$ doping level, resulting in a sharp drop in resistivity (Equation 10). Once the La-doping concentration exceeds a critical level (where the upturn begins), Ti vacancies are created, increasing the resistivity again (Equation 11). Hwang et al. pointed out that La-doped BTO is electrically compensated up to about 0.4 mol% La, while doping concentrations above 0.4 mol% La result in ionic compensation by Ti vacancies.[127] Previously, Glinchuk et al. and Morrison et al. had found analogous increases in resistivity in La-doped BTO, which were attributed to a transition in charge compensation mechanisms from electronic to ionic.[86,129] It is important to note that the critical La-doping concentration at which the charge compensation mechanism changes varies in the different studies, which is probably due to the different synthesis methods.[127,130] Ganguly et al. reported that in $Ba_{1-x}La_{2x/3}TiO_3$ ($0 \leq x \leq 0.10$) synthesized by solid-state reaction, the dielectric constant improved with increasing La content.[131] A phase shift from the tetragonal to the cubic phase was observed with increasing La-doping level, as previously documented in the literature.[132,133] The study showed that higher La-doping levels lower the phase transition temperature.

Specifically, La-doped BTO samples with $x < 0.06$ exhibited a tetragonal phase, while those with $x \geq 0.08$ showed a cubic phase at RT. This indicates that with increasing substitution of $Ba^{2+}$ by $La^{3+}$ the tetragonality decreases, which means that the charge neutrality of the A-site is not maintained. In addition, the dielectric constant was found to decrease with increasing frequency, with higher values at lower frequencies—a trend al-

ready observed in studies focusing on the transition temperature with increasing La concentration.[136,137] For La-doping up to 0.3 mol%, the change in lattice metrics is negligible. The lattice parameters along the *a*-axis and the *b*-axis remain fairly constant, while the lattice parameter along the *c*-axis decreases steadily. At concentrations above 0.3 mol%, however, the lattice changes become more pronounced: the *a*-axis parameter increases with the La-doping concentration, and the *c*-axis decreases more strongly. In order to induce a local compressive strain along the *c*-axis, $Ba^{2+}$ ions are replaced by with slightly smaller $La^{3+}$.[64]

Despite these changes, La-doped BTO retains its tetragonal structure and remains ferroelectric at all doping levels at RT. To understand the physical basis for the different changes in lattice parameters above and below 0.3 mol% La-doping, it was necessary to investigate the change in lattice volume as a function of La concentration. Recently, Hwang et al. found that the lattice volume of La-doped BTO gradually decreases with increasing La concentration up to 0.3 mol% and the results showed that the loss of lattice volume increases once the La-doping exceeds 0.3 mol%.[127] Changes in charge compensation pathways also affect the microstructure of La-doped BTO. For example, the average grain size of La-doped BTO decreases significantly when the La-doping level reaches 0.2 mol%. However, the effect of the reduction in grain size caused by doping is negligible at 0.2 mol% La. Yamaji et al. and later Ávila et al. suggested that at 0.3 mol% La, ionic charge compensation occurs, forming Ti vacancies, which may have hindered the movement of grain boundaries required for grain growth.[138,139] In addition, the studies by Wang et al. and Hwang et al. showed that the standard deviation of the average particle size decreases with increasing La concentration.[127,140] For example, the average grain size of pure BTO was 29.4 µm, but 0.4 mol% La-doped BTO had a standard deviation of only 0.9 µm. Sumona et al. found that the tetragonal structure remained stable in Ln-doped BTO-based samples such as $Ba_{1-x}La_xTi_{(1-y)/x}Zr_yO_3$ ($x = 0.015$, $y = 0.15$, 0.25, 0.35), with La incorporation leading to the formation of Ti vacancies, that further hindered the grain growth.[125] Wongdamnern et al. showed that $Ba_{1-x}La_xTiO_3$ ($x =$ 0.005, 0.01, 0.02, 0.04, 0.08) sintered at 1400 °C exhibited tetragonal symmetry after doping.[141] The cubic structure was gradually formed, and the grain size decreased with increasing La concentration. The substitution of $La^{3+}$ at $Ba^{2+}$-sites in the BTO host stabilized the cubic structure and led to defects due to aliovalent substitution. With increasing La content, the temperature of the transition from cubic-to-tetragonal decreased due to lower tetragonality, while the peak of the transition broadened, indicating a diffuse phase transition. Mathiarasu et al. demonstrated that the ionic partial mechanism, involving Ti vacancy formation, is the most favorable pathway for doping in this system.[142] Apart from the phase transformation, La-doping significantly reduces grain formation, and increases lattice strain, as shown by the shift of the peak associated with the (200) and (002) Bragg reflections of the tetragonal phase in pure BTO (Figure 3b). This inverse relationship between the crystallite size and the lattice strain confirms the presence of dopants in the lattice. While pure BTO exhibits strong agglomeration, the La-doped BTO forms well-defined microspheres with distinct grain boundaries. The La dopant may have concentrated at the grain boundaries, limiting further expansion of the grains and resulting in smaller particles compared to pure BTO.[143]

### 2.2. The Case of Ce-Doped BTO

The $BaCe_xTi_{1-x}O_3$, in which $Ti^{4+}$ is partially replaced by $Ce^{4+}$, is a promising lead-free material for tunable capacitors, high capacitance MLCCs, and actuators, as the incorporation of Ce can increase the $d_{33}$ value.[144–149] The introduction of cerium (Ce) into BTO host leads to structural changes that vary with Ce concentration. The doping mechanism is complex; Ce ions can exist in the valance states $Ce^{3+}$ and $Ce^{4+}$, with radii of (1.01 Å, CN = 6; 1.34 Å, CN = 12) and 0.87 Å (0.87 Å, CN = 6; 1.28 Å, CN = 12), respectively.[149] Initially, $Ce^{3+}$ replace $Ba^{2+}$ at the A-site.[150] When the Ce concentration is low (Ce/Ba ratio < 0.6%), cation vacancies form due to the smaller ionic radius of $Ce^{3+}$ compared to $Ba^{2+}$, leading to a reduction in cell volume.[151] The charge compensation mechanism for this substitution is described as follows:

$$BaTiO_3 + xCe^{3+} \rightarrow Ba^{2+}_{1-x}\left(Ce_{Ba}\right)_x Ti^{4+}O_3{}^{2-} + xV''Ba \quad (12)$$

The Ce/Ba atomic ratio of 0.6% results in the highest $d_{33}$ in $BaCe_xTi_{1-x}O_3$. Beyond this ratio, $Ce^{4+}$ begins to replace for $Ti^{4+}$ at the B-sites[149] and $Ce^{4+}$ pulls six $O^{2-}$ ions out of the original cell, changing the structure from tetragonal to cubic. This structural shift increases the cell volume, and decreases both the spontaneous polarization and the $d_{33}$ values.[152,153] This mechanism can be expressed by the following formula:

$$BaTiO_3 + xCe^{3+} + yCe^{4+} \rightarrow$$
$$Ba_{1-x}{}^{2+}\left(Ce_{Ba}\right)_x\left(Ti_{1-y}{}^{4+}\left(Ce_{Ti}\right)_y\right)O_3{}^{2-} + xV''_{Ba} + yTi''''_{Ti} \quad (13)$$

The doping mechanism discussed above, indicates that the maximum output signals occur at a Ce concentration of 0.6%.[154] Canu et al.[155] found that $Ce^{4+}$ at the Ti-site significantly affects the phase transition temperatures and the polar arrangements: for $0.09 < x < 0.2$, a single rhombohedral-to-cubic transition appears, while higher $x$ values show relaxor behavior and a cubic structure. In $BaCe_xTi_{1-x}O_3$ ceramics ($x = 0.02$–0.30), a gradual evolution takes place with increasing $x$, transitioning from the long-range polar order of ferroelectric BTO to the short-range polar order of relaxors. The size difference of the ions $Ti^{4+}$ and $Ce^{4+}$ causes strong local stresses, which have a strong effect on the dielectric properties and phase transitions. Furthermore, an increase in Ce concentration leads to an increase in grain size from ≈1 µm ($x = 0.02$) to ≈5 µm ($x = 0.20$), followed by a reduction to 1.5 µm ($x = 0.30$). Dunbar et al. used point-charge calculations to predict the EPR spectrum of Ce at the A- and B-sites of air-fired Ce-doped BTO samples.[45] They found that $Ce^{3+}$ is primarily an A-site dopant, that depends on the Ba/Ti ratio, while Ce at the B-site tends to be in the 4+ state and is therefore, EPR silent. For $BaCe_xTi_{1-x}O_3$ samples with $x = 0.02$–0.30, prepared by solid-state methods, Canu et al. investigated and compared the macroscopic property measurements and average structure using XRD, pair distribution function (PDF) analysis, and Raman spectroscopy.[155] The study enabled the formulation of several important findings on phase transitions in $BaCe_xTi_{1-x}O_3$ over a broad composition ($x = 0.02$–0.30) and temperature range (100–450 K):

i. $BaCe_xTi_{1-x}O_3$ ceramics exhibit a high degree of local structural disorder, which increases with $x$ at all temperatures. This disorder arises from the integration of larger $CeO_6$ octahedra (14.2 Å$^3$) into the $TiO_6$ (10.7 Å$^3$) in BTO, where the mismatch can only be overcome by octahedral tilting and deformation, which redistributes the B–O bond lengths. High disorder leads to widespread phase transitions and a large permittivity peak at the ferro-to-paraelectric transition for $x > 0.05$.
ii. Compositions with $x = 0.20$ and 0.30 showed relaxor behavior. Raman scattering and PDF analysis showed a local rhombohedral arrangement, while the overall structure remained cubic, indicating polar nanoregions. Upon cooling to 238 K, the ceramic with $x = 0.20$ shifted from a relaxor-like short-range polar ordering to a mesoscale-range structure, possibly due to the merging of smaller polar clusters into a weakly polar long-range phase.
iii. Compositions showing a tricritical point ($x = 0.09 – 0.11$) and relaxor compositions ($x = 0.19 – 0.22$) in $BaCe_xTi_{1-x}O_3$ were mostly unaffected by the Ce cation itself. This indicates that a certain number of Ti–O–Ti bonds must be broken before a new ″state″ is formed. Since the $Ce^{4+}$ ions do not move out of the center, they do not contribute to the polar ordering. Therefore, the local strains and fields created by the insertion of larger $CeO_6$ octahedra between $TiO_6$ octahedra of BTO appear to have no effect on the onset of the relaxor state. Local stresses and disorganization have a strong affect on the $T_c$ reduction with $x$. For $Ce^{4+}$, the transition temperature decreases slowly up to $x = 0.10$ ($T_c = 382$ K) and faster for compositions with higher Ce concentrations ($T_c = 303$ K at $x = 0.175$).

Confalonieri et al. provided a comprehensive study of local distortions and octahedral tilts in $BaCe_xTi_{1-x}O_3$ ($x = 0.02 – 0.30$), synthesized by the solid-state method.[156] In terms of the average structure, the $x = 0.02$ composition exhibited the same polymorphic sequence as pure BTO: displaying rhombohedral (R) symmetry at 150 K, orthorhombic (O) at 270 and 350 K, and cubic (C) at 450 K. At 270 K, O and R phases coexist, with O being the dominant phase. At $x = 0.05$, R symmetry occurs at 200 K, O and R coexist at 300 K (O is dominant), and O and T coexist at 350 K (where T is dominant), while the cubic phase is stable at 380 and 420 K. For $x = 0.10$, the composition exhibited a rhombohedral structure at 100 and 200 K, suggesting that the addition of Ce reduces the rhombohedral distortion.[100] For compositions with $x = 0.20$ and 0.30 at 300 K, Canu et al. described the formation of a pseudocubic structure, which changes to an exclusively cubic symmetry at 400 K. Interestingly, the diffraction peaks shift to wider spacing with increasing $x$, indicating lattice expansion due to Ce incorporation. The broadening of the peaks and decrease in peak height with increasing $x$ indicate a broader distribution of bond lengths, a clear indication of an increasing level of disorder. According to Canu et al. the $Ce^{2+}$ substitution at the $Ba^{2+}$ site, if any, is minimal. Lu et al. estimated the $Ce^{3+}$ concentration at the $Ba^{2+}$ site to be about 0.2 at.% for $x$ values between 0.03 and 0.07.[157] Confalonieri et al. confirmed a similar trend discovered by Canu et al. that the strain induced by the large $CeO_6$ octahedra is responsible for both the occurrence of a very diffuse paraelectric/ferroelectric transition even at low Ce concentration ($x = 0.05$), and the almost constant $T_c$ value measured up to $x = 0.10$.[156] Although $Ce^{4+}$ is larger than $Ti^{4+}$, the average crystal structure of $BaCe_xTi_{1-x}O_3$ remains similar to that of undoped BTO. However, the difference between the $CeO_6$ and $TiO_6$ octahedra likely leads to deformations that result in a local structure that deviates significantly from the average.[100] The size difference between Ti and Ce causes stresses that are somewhat alleviated by the formation of volume defects, resulting in strong structural deformation at the atomic level. The disorder increases with Ce concentration at all temperatures. Thus, the local disorder has a significant impact on the average structure and material properties of Ce-doped BTO. Although BTO has no magnetic properties in the bulk, atomic defects induced by Ce-doping can lead to magnetic behavior.[158] Experimental studies have shown that ferromagnetism in BTO, as in other metal oxides such as $CeO_2$, $Al_2O_3$, ZnO, and $SnO_2$, is caused by oxygen vacancies.[159] In particular, only Ti and O vacancies were found to induce ferromagnetism between Ba, Ti, and O defects in BTO. Senthilkumar et al. investigated in detail the doping of BTO with Ce ions, which can occupy both Ba- and Ti-sites due to their high solubility.[160] The authors reported that the incorporation of $Ce^{3+}$ at $Ba^{2+}$- and $Ti^{3+}$-sites together with $Ce^{4+}$ at $Ti^{4+}$-sites is a crucial approach to modulate oxygen vacancies and thus improve the ferromagnetic properties of BTO. Ce-doped BTO nanoparticles were synthesized using $Ce(NO_3)_3{\cdot}6H_2O$ at concentrations of 2, 4 and 6 mol% and XRD revealed a pure tetragonal phase. The shift of diffraction peaks to higher angles in 4 mol% $Ce^{3+}$-doped BTO indicates the incorporation of $Ce^{3+}$ at $Ba^{2+}$ sites. In the BTO 6 mol% $Ce^{3+}$ doped BTO, a significant shift to the lower angles indicates a substitution of $Ce^{3+}/Ce^{4+}$ at the $Ti^{3+}/Ti^{4+}$ sites.[161,162] Moreover, the oxidation of $Ce^{3+}$ to $Ce^{4+}$ allows $Ce^{4+}$ to replace $Ti^{4+}$ at the Ti-sites.[163] These unusual features facilitate oxygen vacancies due to a large mismatch between $Ce^{3+}$ and $Ti^{3+}$ and $Ce^{4+}$ and $Ti^{4+}$ and the charge imbalance within the BTO lattice.[164] At a higher Ce concentration (6 mol%), the average size of the nanoassemblies drops (127 nm), since Ce limits grain development and causes grain boundaries to expand. This has a significant impact on electrical properties, since both saturation and remanence polarization are lowered by the depolarization field under Ce-rich conditions. Similar results were also reported by Verna et al.[163] These particular properties promote oxygen vacancies, caused by a significant difference in the ionic radii of $Ce^{3+}$ and $Ti^{3+}$ and $Ce^{4+}$ and $Ti^{4+}$, as well as a charge imbalance in the BTO lattice.[164] Furthermore, numerous studies have reported the incorporation of $Ce^{3+}$ at $Ba^{2+}$- and $Ti^{3+}$-sites, $Ce^{4+}$ at $Ti^{4+}$-sites, and the formation of oxygen vacancies.[163,165] Overall, an increase in oxygen vacancies upon Ce-doping enhances ferromagnetism in Ce-doped BTO.[160,162,166]

The change in $T_c$ has a significant impact on properties. In many practical applications, adjusting $T_c$ is absolutely necessary. Some ceramic capacitors and piezoelectrics, for example, require materials that are temperature stable. Some thermistors require a change in $T_c$ to change the switching temperature. Modulating $T_c$ through doping is an effective way to improve performance. Dopants incorporated at different points in the system, such as BTO, have been shown to have varying effects on $T_c$. In particular, Ce is a well-known Ln element that can occur as $Ce^{3+}$ and $Ce^{4+}$ as described above, and as such $Ce^{3+}$ can be incorporated at the A-site and $Ce^{4+}$ at the B-site in the BTO lattice when sin-

tered in air. However, there have been some inconsistent reports about how $T_c$ changes as $Ce^{4+}$ incorporates at B-sites. According to Chen et al., for a doping concentration of 0 – 50 mol%, increasing Ce content results in a decreased $T_c$ value.[167] Curecheriu et al. have also reported that at a doping level of 6 ~ 20 mol% Ce, $T_c$ decreases with increasing Ce content.[146] Hwang and Han and later Brajesh et al. found that Ce content has no influence on $T_c$ value when doping concentrations range from 0.5 to 3 mol% and 2 to 12 mol%, respectively.[168,169] The inconsistent reports might be due to Ce-doping at the A- and B-sites. Therefore, ensuring that Ce is effectively doped into the A- or B-site of BTO ceramics and independently exploring its influence on the $T_c$ is beneficial for understanding and improving the properties of these Ce-doped BTO ceramics. Liu et al. made a significant step forward in this field when they sintered BT-*x*Ce-A ($Ce^{3+}$-doped A-site BTO) and BT-*x*Ce-B ($Ce^{4+}$-doped B-site BTO) ($x$ = 2, 4, 6, 8 mol%) using a standard solid-state reaction at 1430 °C and 1500 °C, respectively.[170] It was demonstrated that the substitution of Ce dopants on the A- and B-sites had differing impacts on the phase transition, microstructure, and electrical properties of the BTO ceramic. The BT-*x*Ce-A and BT-*x*Ce-B ceramics have lower $T_c$ values compared to pure BTO, but each doping site shows a unique phase transition behavior. Compared to the BT-*x*Ce-A ceramics, the BT-*x*Ce-B ceramics show a higher $T_c$ value, a stronger behavior at the diffuse phase transition, and improved properties at maximum polarization and strain. The three factors that influence $T_c$ are discussed: the effect of average size, the effect of local strain field, and the local electric field. Of these three factors, the effect of average size and local electric field dominates in the BT-*x*Ce-A samples, and the $T_c$ decreases with increasing Ce content. For the BT-*x*Ce-B samples with a higher $T_c$ value than the BT-*x*Ce-A samples, the local electric field dominates, and the $T_c$ value increases abnormally with increasing Ce content. The higher $T_c$ value leads to improved ferroelectricity and polarizability, resulting in higher maximum polarization responses for the BT-*x*Ce-B. Therefore, the BT-*x*Ce-B samples show a larger difference between the maximum and remnant polarization and a higher strain compared to the BT-*x*Ce-A samples.

The maximum dielectric constant of BT-*x*Ce-A ceramics tends to increase from 10 120 to 15 039, while that of BT-*x*Ce-B ceramics increases from 6560 to 6919. Considering the practical application of ferroelectrics, the relative permittivity values were compared, which is related to the difference between $T_c$ and RT ($|T_c$-25 °C|). The greater this distance, the lower the energy barrier of the polarization response and the smaller the value of the relative permittivity. For the BT-*x*Ce-A ceramic, the $|T_c$-25 °C| values are 37.05, 8.09, 29.29, and 53.21 °C, while the corresponding values for the relative permittivity are 3986, 6765, 5354, and 3332, respectively. Analogously, for the BT-xCe-B ceramic, the $|T_c$-25 °C| values are 53.98, 54.65, 60.12, and 71.56 °C, respectively, and the corresponding permittivity values are 3674, 3488, 3380, and 2511, respectively. In addition, both the maximum dielectric constant and the relative permittivity of the BT-*x*Ce-A ceramic are higher than those of the BT-*x*Ce-B ceramic. The higher dielectric constant for the BT-*x*Ce-A ceramic could be due to its larger grain size. Namely, from a microstructural point of view, the grain size of the BT-*x*Ce-A ceramic increases with increasing Ce content and ranges from 0.5 μm to 1.5 μm. In contrast, the grain size of the BT-*x*Ce-B ceramic varies only slightly with increasing Ce concentration (about 0.3 μm) and is smaller than that of the BT-*x*Ce-A ceramic.

When it comes to the rapid development of electronic technology toward miniaturization, ferroelectric refrigeration based on the electrocaloric effect (ECE) is a popular choice for microelectronic systems due to its advantages such as easy miniaturization, high conversion efficiency, low cost, and environmental friendliness.[171–174]

Doping with different Ln elements diffuses the first-order phase transition of BTO and changes its ferroelectric and ECE properties, as shown by Fan et al.[176] Xie et al. systematically investigated the ECE property with Ce-doping at A-site ($Ba_{1-x}Ce_xTiO_3$) or B-site ($BaCe_xTi_{1-x}O_3$) ($x$ = 0.01, 0.02, 0.03, 0.04) prepared by the solid-state method at 1400 °C and showed that Ce-doping can significantly improve the sintering activity of BTO.[175] All samples formed a pure perovskite lattice with additional phases, as illustrated in **Figure 4**. With increasing Ce content, the reflections (002) and (200) gradually overlap, regardless of whether the doping occurs at the A- or B-sites, indicating that the tetragonal distortion of the BTO lattice becomes weaker (Figure 4a,b). However, doping at the A-site causes the reflections to move to a higher angle, leading to lattice contraction, while doping at the B-site has a slightly opposite effect, and leads to lattice expansion. The reason for this is that the Ce ion at the A or B position of the perovskite lattice has different valence states and radii. The different fluctuations in the lattice metrics (Figure 2c) indicate that the Ce ions enter the A-site of $Ba_{1-x}Ce_xTiO_3$ or the B-site of $BaCe_xTi_{1-x}O_3$. The variation of the valence states and the radii of the Ce ions in the A or B-sites of the perovskite lattice explains this phenomenon. The $Ce^{3+}$ at A-sites has a smaller radius than the $Ba^{2+}$, but the $Ce^{4+}$ at B-sites has an ionic radius of 0.87 Å and thus exceeds that of the $Ti^{4+}$. Overall, all sintered samples have a pure perovskite phase, regardless of whether Ce is doped at A- or B-sites, however the characteristics differ. The $T_c$ value in A-site doped $Ba_{1-x}Ce_xTiO_3$ progressively reduces because the $Ce^{3+}$ dopants have a smaller radius than $Ba^{2+}$ ions, while the phase transition diffuses and the latent heat diminishes. The phase transition in B-site doped $BaCe_xTi_{1-x}O_3$ is more diffuse, but the $T_c$ value scarcely varies, resulting in a depressed but not shifted ECE peak. In addition, the $Ba_{1-x}Ce_xTiO_3$ samples exhibit a solid morphology (Figure 4d–j) without intercrystalline pores, except at $x$ = 0.01. The grain size increases visibly with increasing Ce content from 0.2 μm to 3μm. The morphology of the $BaCe_xTi_{1-x}O_3$ sample is dense, but the grain size is considerably larger (2–3 μm), which increases slightly with Ce-doping. This trend shows that doping with Ce can effectively increase the sintering activity of BTO ceramics.

### 2.3. The Case of Pr-Doped BTO

Compared to BTO doped with La and Ce, the amount of research on BTO doped with praseodymium, Pr, is significantly lower. In general, Pr has rarely been considered by chemists and physicists as a dopant for BTO in the dielectric region. Only $Ba_{1-x}Pr_xTiO_3$ ($x$ = 0.003) ceramic has been reported to exhibit semiconducting behavior, which is due to a widespread positive temperature coefficient of resistance effect in BTO doped with lower amounts of Pr dopants (< 0.5%).[116,177] Researchers have used $Pr^{3+}$ to im-

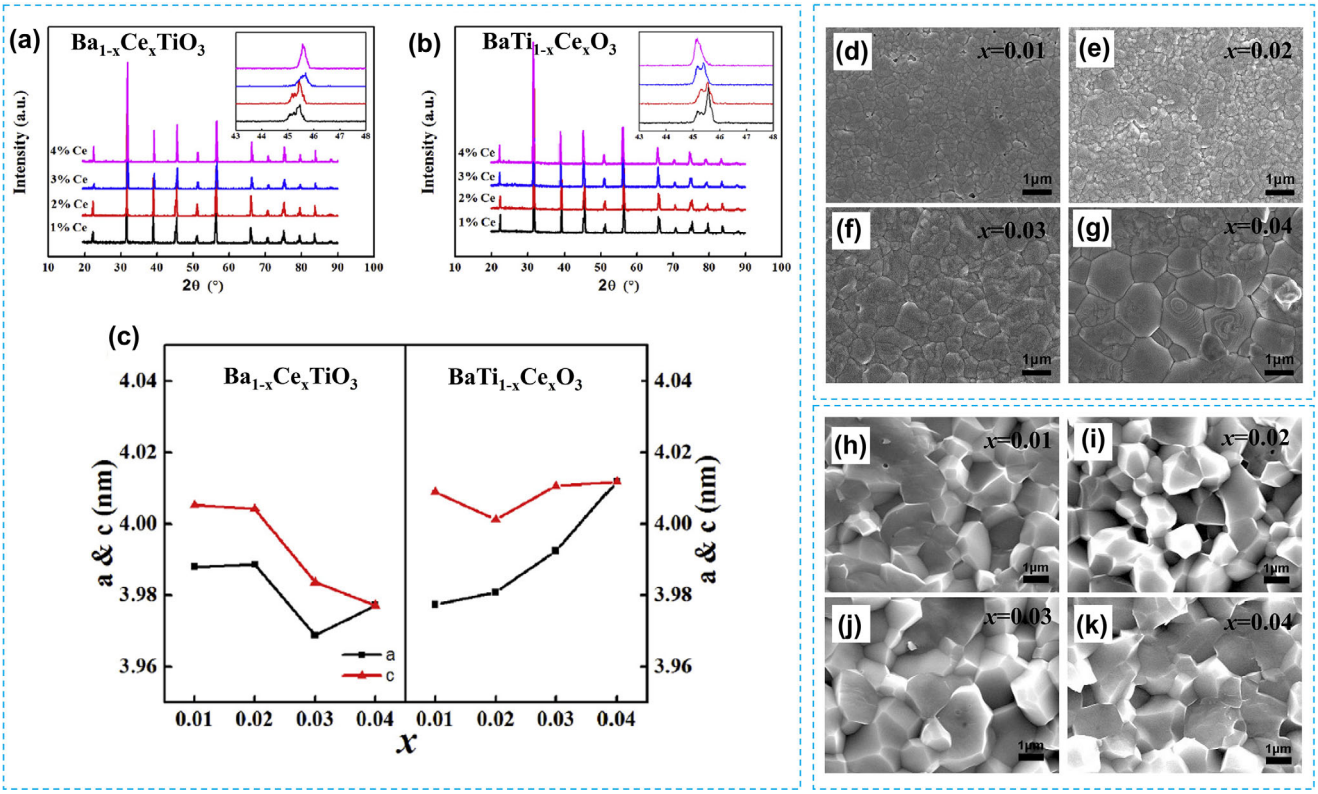


**Figure 4.** Cascade XRD patterns of a) $Ba_{1-x}Ce_xTiO_3$ and b) $BaCe_xTi_{1-x}O_3$ with insets showing the enlarged region around 45° 2$\theta$, c) the variation of lattice parameters with the amount of Ce-doping in A- or B-sites and scanning electron microsocpe (SEM) micrographs of d–g) $Ba_{1-x}Ce_xTiO_3$ and h–j) $BaCe_xTi_{1-x}O_3$. Modified with permission.[175] Copyright 2017, Elsevier.

prove the piezoelectric, optical, and photoluminescent properties of ferroelectrics such as $BaSrTiO_3$, $(Ba_{1-x}Ca_x)TiO_3$ and BTO ceramics.[178–182]

However, the microstructure and optical properties of Pr-doped BTO have only been studied to a limited extent. The structural features, especially the preferential doping sites of Pr dopants in the BTO host, have been complementarily investigated by XRD measurements and X-ray photoelectron spectroscopy (XPS), as recently reported by Chabungbam et al.[183] The authors showed that the crystal structure of the Pr-doped BTO thin films exhibits a crystalline character, with diffraction peaks consistent with the tetragonal structure of BTO (**Figure 5a,b**). The slight shift of the (110) peak to a higher angle was attributed to the substitution of $Ba^{2+}$, which has a larger radius, by $Pr^{3+}$, which is characterized by a smaller radius (0.99 Å, CN = 6) at the A-site, leading to a decrease in the interplanar crystal spacing and lattice contraction.[43,184]

XPS also revealed the existence of lattice oxygen associated with the perovskite BTO structure ($O_L$), oxygen vacancies ($O_V$), and oxygen atoms adsorbed on the surface ($O_{OH}$) (Figure 5c–f). When some of the $Ti^{4+}$ ions in BTO are converted to $Ti^{3+}$ ions, the increased number of oxygen vacancies is compensated by the higher $Ti^{3+}$ concentration of doped BTO compared to pure BTO. The high $Ti^{3+}$ concentration also indicates that the Pr ion replaces the Ba-site, resulting in free electrons.[185] In addition, the occurrence of $Ti^{3+}$ and $O_V$ states indicates the presence of flaw sites on the surface.[186] The XPS verified the existence of $Pr^{3+}$ in BTO at a concentration of ≈0.96 at.%. Iriani et al. also reported the formation of tetragonal Pr-doped BTO phase, i.e., sol–gel prepared $Ba_{1-x}Pr_xTiO_3$ thin films, using the doping method.[187] The addition of Pr dopants to BTO thin films leads to a shrinkage of lattice parameters, unit cell volume, and a decrease in crystallite size. In contrast, Pr-doping leads to changes in tetragonality and lattice strain as well as an increase in crystallite size.[188]

The $Pr_6O_{11}$ is a stable praseodymium oxide commonly used for the synthesis of Pr-doped BTO and contains two $Pr^{3+}$ ions and four $Pr^{4+}$ ions. It is well known that trivalent light Ln ions tend to occupy $Ba^{2+}$-sites, while $Pr^{4+}$ ions favor $Ba^{2+}$ -sites over $Ti^{4+}$ sites in BTO co-doped with Pr and Zr as well as Pr and Ca. Pr ions were found to enter $Ti^{4+}$ sites as metastable $Pr^{4+}$ (0.85 Å, CN = 6), comparable to $Ce^{4+}$.[189–192]

When $Pr_6O_{11}$ is used as a dopant in a BTO host the probability of different site occupancies and the mixed valence of $Pr^{3+}/Pr^{4+}$, together with the lower stability of $Pr^{4+}$ compared to $Ce^{4+}$ complicate the defect chemistry of Pr-doped BTO.[188,193,194] Lu et al. prepared Pr-doped BTO ceramics, i.e., $(Ba_{1-x}Pr_x)Ti_{1-x/4}O_3$ ($x$ = 0.02, 0.03, 0.04, 0.05), by cold pressing. It was shown that Pr-doping can inhibit grain formation, resulting in a fine-grained ceramic, with the average grain size of Pr-doped BTO being approximately 0.8–0.9 μm. Furthermore, it was assumed in this study that the original $Pr_6O_{11}$ undergoes a complete reduction from $Pr^{4+}$ to $Pr^{3+}$ during long-term sintering in air, leading to compensation of Ti defects.

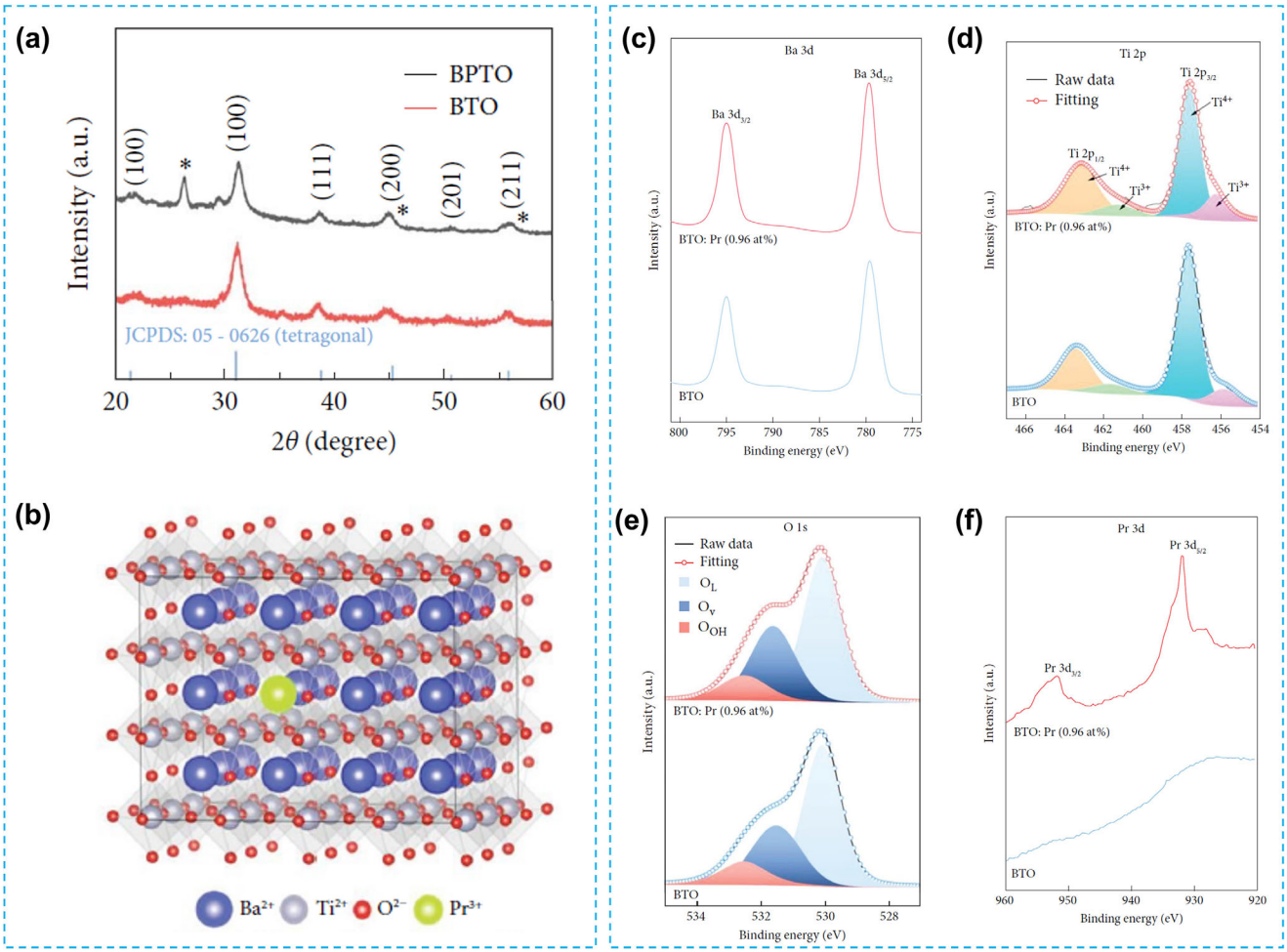


**Figure 5.** a) XRD patterns of BTO and Pr-doped BTO (BPTO) on mica substrates, b) schematic representation of the BPTO perovskite crystal architecture, c) high-resolution XPS spectra of c) Ba 3*d*, d) Ti 2*p*, e) O 1s, and f) Pr 3*d* in the undoped BTO and BPTO samples. Modified with permission.[183] Copyright 2024, Wiley-VCH.

It has been shown that the structure exhibits tetragonal symmetry when doped up to $x = 0.04$, whereas when $x$ is increased to 0.05, the two peaks merge into a symmetric (200) reflection characteristic of a cubic perovskite structure (**Figure 6**).

In the tetragonal range of $x = 0.02$–$0.04$, the parameter $a$ decreases slowly, and $c$ decreases rapidly with $x$. When $x$ is increased to 0.05, $a$ equals $c$. The $V_0$ decreases as $x$ grows up to 0.04 and stays constant between 0.04 and 0.05, where a major structural change occurs. The $c/a$ ratio decreases linearly up to the cubic phase ($x = 0.05$). Furthermore, the Pr-doped BTO exhibited a slight diffuse phase transition and its dielectric-peak temperature decreased rapidly at a rate of −22 °C at%$^{-1}$ Pr. The EPR signal, corresponding to the preservation history of the cubic sample with $x = 0.05$, provided evidence for the presence of a very modest amount of $Pr^{4+}$ at $Ti^{4+}$-sites. In the Ba-rich case, $Pr^{4+}$ ions enter $Ti^{4+}$-sites, in part because the ionic radius of $Pr^{4+}$ is slightly smaller than that of $Ce^{4+}$ and $Ce^{4+}$ ions favor $Ti^{4+}$-sites.[43,144,167] Investigation of the influence of free electron radicals on the EPR signals revealed that the higher intensity of the $g = 2.002$ signal at RT is less related to free electron radicals in Pr-doped BTO than to a high-spin system originating from a charge transfer state [$Pr^{4+}$-$Pr^{3+}$], which is strongly associated with a shift of the valence state of Pr ions at Ti-sites. In general, Pr ions can generate an intervalence charge-transfer state [$Pr^{4+}$-$Pr^{3+}$] by transferring electrons from $Pr^{3+}$ to $Pr^{4+}$.[195,196] However, this transformation cannot occur at Ba-sites in Pr-doped BTO due to the Ba-site valence state and the larger difference in ionic radius between $Pr^{4+}$ and $Ba^{2+}$. A dynamic equilibrium describes the intervalence charge-transfer state, which can only occur at Ti-sites.

$$Pr'_{Ti} \rightarrow Pr_{Ti} + e^{-} \tag{14}$$

The above equation is based on the finding that Pr-doping is more likely to result in electrical conductivity in BTO than La-doping, as indicated by $x = 0.05$. Furthermore, the $Pr^{4+}$ ions at the Ti-sites preferentially capture electrons when the valence state is reversed from a metastable ($Pr^{4+}$) to a regular valence state ($Pr^{3+}$). Pr-doping at the Ti-sites causes a much larger lattice deformation, which can be reduced by the following three cases:

1) A self-compensation mode of $Pr^{\bullet}_{Ba} \rightarrow Pr'_{Ti}$ that does not result in electrical conductivity.

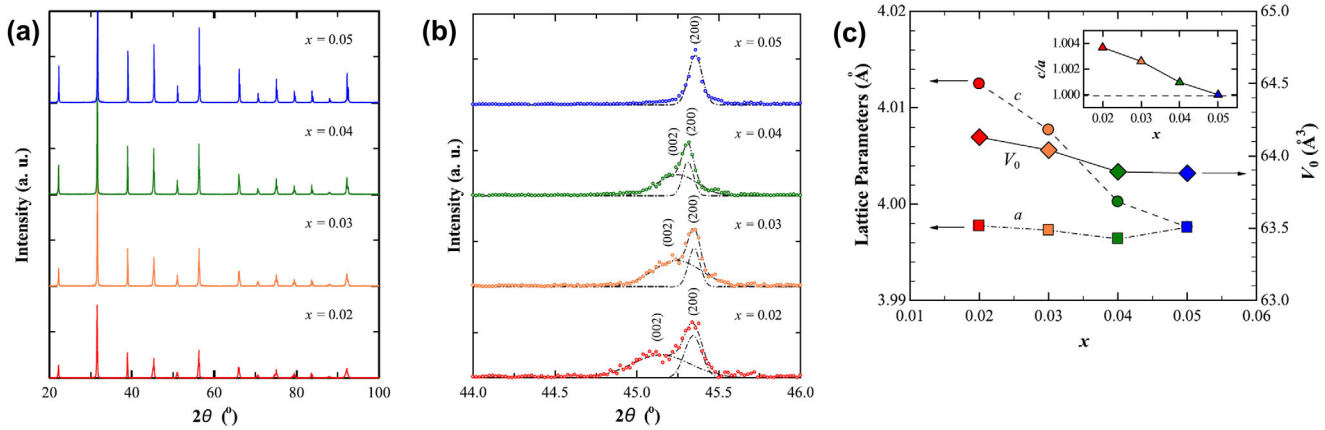


**Figure 6.** a) XRD patterns of $(Ba_{1-x}Pr_x)Ti_{1-x/4}O_3$ ($x = 0.02, 0.03, 0.04, 0.05$), b) evolution of ≈45° peaks with $x$, c) variations of lattice metrics as a function of $x$ for Pr-doped BTO. The dashed lines in (b) are from the Gaussian fit to the peaks. The inset in (c) shows the $c/a$ ratio as a function of $x$. Modified with permission.[188] Copyright 2014, Elsevier.

2) Mixed-valence mode of $Pr^{3+}/Pr^{4+}$ in the Ti-site. Equation (14) indicates that $Pr^{3+}$ is more stable than the metastable $Pr^{4+}$ and that the $Pr^{4+}$ in the Ti-site has a smaller ionic size than $Ti^{4+}$, leading to a dynamic equilibrium.
3) In La- and Ce-codoped BTO, the Ti vacancies are often located near one or more $CeO_6$ octahedra to compensate for the substitution of $Ti^{4+}$ ions by $Ce^{4+}$ ions.[44,149] Similarly, Ti vacancies may exist near $Pr^{4+}$ in $PrO_6$ octahedra. It is assumed that the charge-transfer state [$Pr^{4+}$-$Pr^{3+}$] prolongs the spin-lattice relaxation time and leads to an excited state that is thermally accessible. The signal at $g = 3.77$ is therefore detected. According to the previous studies, the high spin system could originate from exchange-coupling defect clusters – intervalence charge-transfer state [$Pr^{4+}$-$Pr^{3+}$]. The high strength signal at $g = 2.002$ in Pr-doped BTO was attributed to this high-spin system originating from the exchange-coupling defect clusters and not from free radicals, independent $Pr^{3+}$ non-Kramers ions, and metastable $Pr^{4+}$ ions.

The complementary studies by Lu et al. have indicated that Pr ions predominantly replace Ba-sites as $Pr^{3+}$ and induce Ti-vacancy defects. In the solid solution formation of Pr-doped BTO sintered in air, the reduction of $Pr^{4+}$ to $Pr^{3+}$ in the starting $Pr_6O_{11}$ has the priority over the entry of $Pr^{4+}$ ions at the Ti-sites of the perovskite lattice, since $Pr^{4+}$ ions are unstable compared to $Pr^{3+}$ ions. The majority of $Pr^{4+}$ ions in $Pr_6O_{11}$ are initially reduced to $Pr^{3+}$ ions.

$$2Pr_6O_{11}+TiO_2 \rightarrow 12Pr^{\bullet}_{Ba}+3V''''_{Ti}+9Ti_{Ti}+36O_O+2O_2 \quad (15)$$

The presence of Ti vacancies can lead to a small number of $Pr^{4+}$ ions entering $Pr_6O_{11}$ without reduction at Ti-sites.

$$2Pr_6O_{11}+5BaO \rightarrow 5Ba_{Ba}+4Pr^{\bullet}_{Ba}+8Pr_{Ti}+V''''_{Ti}+27O_2 \quad (16)$$

In addition, the authors have shown that the amount of Pr ions substituted at the Ti-sites cannot exceed 1%. The Pr ions in $Pr_6O_{11}$ cannot fully enter Ti-sites. Therefore, the increase in volume generated by a very small number of Ti-site $Pr^{4+}$ ions was not detectable by XRD. As explained in Equation (14), Ti-site $Pr^{4+}$ can be reduced to $Pr^{3+}$ by the influence of a Ba-site $Pr^{3+}$ donor. When $x$ is lower ($x = 0.02$–$0.04$), the intervalence charge-transfer state and the capacity of Mn impurities to trap electrons become more apparent. Pr-doped BTO can retain its insulating properties. When $x$ is increased to a higher concentration ($x = 0.05$), the inhibition threshold of electrical conductivity is broken, resulting in Pr-doped BTO becoming a semiconductor. The Pr-doped BTO ceramics require a high sintering temperature of 1480 °C due to their sensitive ceramic density. It is well known that BTO can lose a small amount of oxygen at high temperatures, resulting in semiconducting behavior. The EPR signal associated with oxygen vacancies is reportedly too weak to be detected at ambient temperature.[197] So it was believed that assessing oxygen vacancies in Pr-doped BTO would be challenging. Samples with $x = 0.02$–$0.04$ showed strong insulating behavior (>$10^8$ Ω cm) and reduced tan$\delta$ (< 0.05) below 120 °C. This observation shows that oxygen vacancies that can cause electrical conductivity can be excluded, which means that modest Pr ions can prevent the development of volume $V_0$.

When the doping level reaches a certain threshold value, such as $x = 0.05$, it can be concluded that the semiconducting nature and the increased tan$\delta$ were mainly caused by the Ba-site $Pr^{3+}$-doping behavior. In this situation, the increased concentration of Ti vacancies increased the probability of $Pr^{3+}$ ions entering Ti-sites and forming the charge-transfer state [$Pr^{4+}$-$Pr^{3+}$] with higher intervalence. The latter also contributed to the electrical conductivity. Thus, the sample behaved semiconducting at $x = 0.05$ and a thermally accessible $g = 3.77$ EPR signal attributable to the Ti-site $Pr^{4+}$ was successfully detected. The primary defects in Pr-doped BTO are Ba-site $Pr^{3+}$ ($Pr^{\bullet}_{Ba}$) and Ti vacancies ($V'''_{Ti}$), with a very small amount of Ti-site $Pr^{4+}$ ($Pr_{Ti}$) and Ti-site $Pr^{3+}$ ($Pr'_{Ti}$). The low mixed valence and amphoteric behavior of the Pr ions in BTO is due to their valence state and site occupancy. The study on defect chemistry by Lu et al. concludes that Pr ions primarily substitute for Ba-sites as $Pr^{3+}$, inducing Ti-vacancy defects; a negligible amount of Pr ions enter Ti-sites as $Pr^{4+}$, creating an intervalence charge-transfer state [$Pr^{4+}$–$Pr^{3+}$].

### 2.4. The Case of Nd-Doped BTO

In contrast to BTO systems doped with Ce cations, neodymium, Nd can replace $Ba^{2+}$ and $Ti^{4+}$ in the BTO host and improve its structural characteristics.[51,198–203] It can also improve the dielectric and ferroelectric properties of BTO ceramics. In the early stages of research on Nd-doped BTO, Shaikh et al. showed that the addition of neodymium oxide to BTO drastically lowers the $T_c$ value; less than 3 mol% $Nd_2O_3{\cdot}3/2TiO_2$ shifts the $T_c$ value below RT.[204] Also, ferroelectric phase transformation becomes diffuse with doping of 3 mol% $Nd_2O_3{\cdot}3/2TiO_2$ and higher. Yao et al. reported the traditional solid-state reaction of $Ba_{1-x}Nd_xTiO_3$ ($0 \leq x \leq 0.10$) and proposed that the replacement of $Ba^{2+}$ by $Nd^{3+}$ (0.983 Å, CN = 6) alters the Ti valence state.[43,205] Earlier, Hirose et al. found that the replacement of $Ba^{2+}$ and $Ti^{4+}$ by Nd broadens the permittivity peak at 127 °C in stoichiometric BTO and shifts it to lower temperatures with increasing Nd-doping level.[206] Namely, the authors have prepared $Ba_{1-x}Nd_{2x}Ti_{1-x}O_3$: $0 \leq x \leq 0.12$ at 1300 °C and $0 \leq x \leq 0.14$ at 1400 °C. With increasing $x$, the symmetry changes from tetragonal to cubic at $x = 0.09$. The pronounced permittivity peak at 127 °C in stoichiometric BTO expanded rapidly with increasing $x$ and shifted to lower temperatures; this phenomenon appears to be due to the substitution of Nd at Ti-sites, which hinders the formation of ferroelectric domains due to the presence of dipole-inactive $Nd^{3+}$ at Ti-sites. Murugaraj et al. and Shaikh et al. have shown that the addition of Nd dopant to the BTO host leads to a decrease in $T_c$ and the appearance of lattice vacancies, resulting in a diffuse phase transition.[204,207] Additionally, there have been recent reports on the use of Nd-doped BTO to achieve a colossal dielectric constant at RT and low temperatures.[51,208] In these studies, the ferroelectric properties of $Ba_{1-x}Nd_xTiO_3$ ($x = 0 - 0.08$) ceramics, the evolution of the structure and dielectric properties of $Ba_{1-x}Nd_xTi_{0.97}Mn_{0.03}O_3$ ($x = 0.01 - 0.06$) ceramics by Nd-doping, and the role of oxygen vacancies in $Ba_{1-x}Nd_{2x/3}TiO_3$ ceramics at $x = 0$ and $x = 0.04$ were revealed.[209–211] However, higher Nd concentrations have hardly been achieved. Although Nd-doped BTO ceramics have been studied[204,206–208,212] the mechanism for their enhanced permittivity remained rather unclear until a few years ago, when Sun et al. reported the investigation of the structure, defect chemistry, and RT colossal permittivity of series of $x$Nd-doped BTO nanoparticles ($x = 0$–3.0 mol%).[51] By systematically analyzing the chemical composition, crystalline structure and defect chemistry, the authors were able to demonstrate the substitution mechanism involving the occupation of $Nd^{3+}$ at the $Ba^{2+}$-site associated with the generation of Ba and O vacancies for charge compensation. All samples exhibited a tetragonal phase, and their tetragonality gradually decreased with increasing Nd concentration. Shoulder peaks at high binding energy rule out the evolution of reductive $Ti^{3+}$ ions while revealing the potential coexistence of Ba and O vacancies. Additionally, the EPR and photoluminescence (PL) measurements, revealed the presence of Ba and O vacancies. From this it can be deduced that the introduction of Nd into BTO leads to simultaneous formation of Ba and O vacancies in order to balance the charge, as the following equation explains:

$$2Nd + 2Ba_{Ba} + 2Ti_{Ti} + 6O_O \rightarrow 2Nd^{\bullet}_{Ba} + 2V''_{Ba} + V^{\bullet\bullet}_{O} + 2BaTiO_3 \quad (17)$$

So far, such an occupancy mechanism has been considered in the study of Ln-doped BTO ceramics. However, the presence of Ba vacancies generated by donor-doping mechanisms has never been experimentally demonstrated due to the mixing of $Ba_{1-y}La_yTi_{1-y/4}O_3$ and other Ti-rich phases, such as $Ba_6Ti_{17}O_{40}$.[34] Sun et al. showed that the formation of Ba vacancies can be favored by hydrothermal conditions, where Ba deficiency can be easily produced by the introduction of protons.[51,213] Dunbar et al. used EPR to investigate the dopant site occupancy of BTO doped with 1% selected Ln (i.e., Ce, Nd, Sm, Gd, Dy, Er, Yb) in Ba- and Ti-rich (Ba/Ti = 1.01, 0.99) BTO.[45] However, it was not clear from the EPR spectra which sites were occupied by $Nd^{3+}$ions. Nevertheless, the metal vacancies correlated with the preferred position of the dopant. Samples with A-site dopants (Ce, Nd, Sm) contained more Ti vacancies and fewer Ba vacancies than samples with amphoteric dopants (Er, Dy). Wang et al. used a traditional solid-state reaction to synthesize the $Ba_{1-x}Nd_{2x/3}TiO_3$ ceramic ($x = 0$–0.2).[203] At 1450 °C, the Nd dopant can enter completely into the perovskite lattice. For $Ba_{1-x}Nd_{2x/3}TiO_3$ ceramics with $x \leq 0.06$, which has a coexistence of tetragonal (T) and pseudocubic phaseC, Rietveld refinement showed that Nd substitution can reduce the volume of the unit cell and prevent the formation of the pseudocubic phase (**Figure 7** and **Table 1**). When the $x$ value is above 0.08, a cubic (c) single phase was also detected.

The XPS investigations indicated that the incorporation of Nd leads to an increased presence of Ba and O vacancies. An appropriate amount of Nd can yield a fine-grained and dense microstructure, whereas an excessive Nd addition results in pronounced grain development and decreased relative density. A similar trend was previously reported by Yao et al. and Sun et al. and later by Hamidi et al.[51,205,214] When the amounts of $V''_{Ba}$, $Nd^{\bullet}_{Ba}$, and $V^{\bullet\bullet}_{O}$ defects formed were minimal, the pinging effect prevailed, which inhibits grain development; conversely, as the concentration of defects increases, the mass diffusion rate is significantly increased, which promotes grain growth. Recently, Hamidi et al. investigated the role of Nd-doping on the structural, morphological and optical properties of hydrothermally synthesized BTO nanoparticles and confirmed the incorporation of $Nd^{3+}$ into the BTO and the amphoteric substitution of $Nd^{3+}$ at the Ba- and Ti-sites at 6 and 10 wt%, while all powders crystallized in a cubic symmetry with nanosized crystallites.[214]

### 2.5. The Case of Sm-Doped BTO

Doped BTO ceramics containing acceptor ions hinder the increase of charge carrier concentration in a reducing environment and thus influence the conduction behavior, leading to favorable dielectric properties. In the Ln family, the samarium, Sm, has an average ionic radius like that of $Ba^{2+}$ and $Ti^{4+}$ (1.24 Å, CN = 12 and 0.958 Å, CN = 6).[43] Therefore, $Sm^{3+}$ can replace the A/B-sites and influence the crystal structure as well as the dielectric and electrical properties of BTO. The Sm-doped BTO ceramics exhibit a considerable positive temperature coefficient at low doping levels (< 1 mol%).[215,216] Moreover, doping with Sm significantly improves the thermal stability of BTO ceramics while maintaining a high dielectric constant.[217] Furthermore, doping BTO with Sm can tune the ferroelectric properties and improve

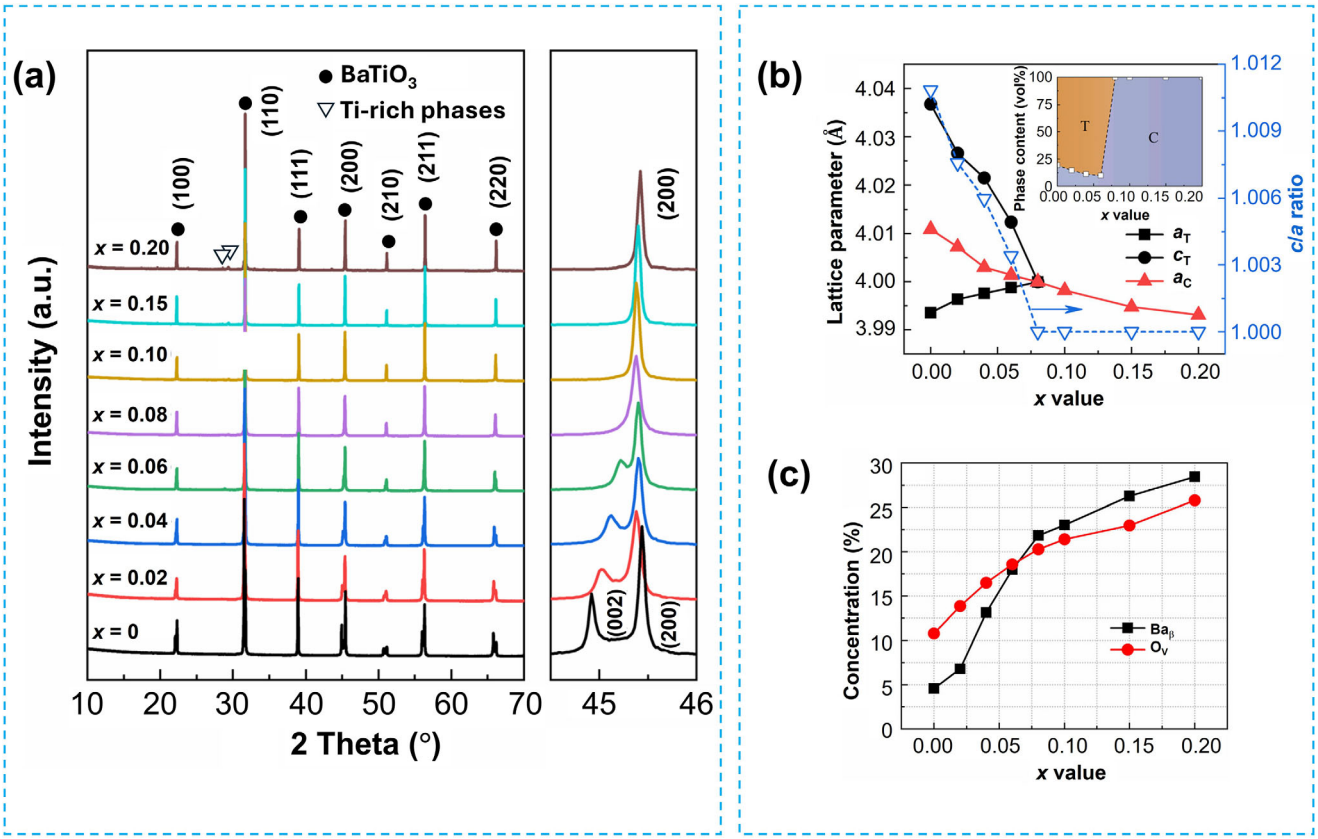


**Figure 7.** a) PXRD patterns of sintered $Ba_{1-x}Nd_{2x/3}TiO_3$, together with the enlarged PXRD patterns at ≈45° 2$\theta$, b) curves of the lattice parameters and the $c/a$ ratio as a function of the $x$ in $Ba_{1-x}Nd_{2x/3}TiO_3$ (the inset shows the phase compositions as a function of the $x$), c) calculated defect concentrations for the $Ba_{1-x}Nd_{2x/3}TiO_3$. Modified with permission.[203] Copyright 2023, Springer Nature.

spontaneous polarization.[218] Thakur et al. reported an increase in the RT value of the dielectric constant and a decrease in the transition temperature when the Sm concentration in BTO was increased, while Jo et al. discovered a significant relationship between the $T_c$ and the unit cell volume.[219,220] Dongsheng et al. reported that the incorporation of Sm into BTO reduced the resistivity of BTO powders with increasing temperature.[221]

The conductivity and dielectric characteristics of BTO ceramics are strongly influenced by the exchange site of Sm at the A/B-site and by defects, which is why there are different opinions on this subject.[222,223] Indeed, it has been shown that the powders prepared by the homogeneous precipitation method have small particle size, homogeneous distribution of dopants, and strong sintering activity, which are advantages over the powders prepared by the solid-state reaction.[224,225] BTO is the main material in the dielectric layer of MLCCs, prepared with base metal electrodes to reduce the production cost. However, base metal electrodes are susceptible to oxidation during the sintering process. Therefore, a reducing atmosphere is required during the sintering process.[226,227] As mentioned in the text, Dunbar et al. performed point charge calculations to estimate the EPR spectra of the individual Ln dopants in the A- and B-sites of BTO samples fired in reducing atmospheres and compared them with XRD data.[45] Namely, when $Ce^{3+}$, $Sm^{3+}$, $Dy^{3+}$ and $Yb^{3+}$ ions are used as dopants, the EPR spectra for the A- and B-site substitution are different. No signal from any site was observed in Sm-doped samples. In general, the metal vacancy levels were traced with respect to the preferred position of the dopant. It was found that samples with A-site dopants ($Ce^{3+}$, $Nd^{3+}$, and $Sm^{3+}$) contained more Ti and fewer Ba vacancies than samples with amphoteric dopants ($Er^{3+}$ and $Dy^{3+}$). During the sintering of BTO in a reducing environment, the O atoms within the lattice are expelled, leading to the formation of electrons and oxygen vacancies, as shown in the following equation:

$$O_O \rightarrow V_O^{\bullet\bullet} + 2e' + 1/2O_2 \quad (18)$$

$$BaTiO_3 + xH_2 \rightarrow BaTi^{4+}_{1-2x}Ti^{3+}_{2x}O_{3-x} + xH_2O \quad (19)$$

The simultaneous increase of $Ti^{3+}$ leads to the semiconductor-like properties of BTO (Equation 19).[228–230] Ohnuma et al. investigated the local structure of Sm-doped BTO solid solutions. These investigations showed that Sm is soluble in both the A- and B-sites of BTO (*i.e.*, $(Ba_{1-x}Sm_x)(Ti_{1-x}Sm_x)O_3$, $x = 0.050$).[231] In addition, $Sm^{3+}$ ions can act as both a donor and an acceptor, in BTO, which enables the control of electrical properties by substitutions with precise ionic radii. Recently, Wang et al. investigated $x$Sm-doped BTO powders ($x$ = 0.5 – 7 mol%) prepared by precipitation and sintered in air and reducing atmospheres (**Figure 8**).[185] The effects of Sm with different doping levels and in dif-

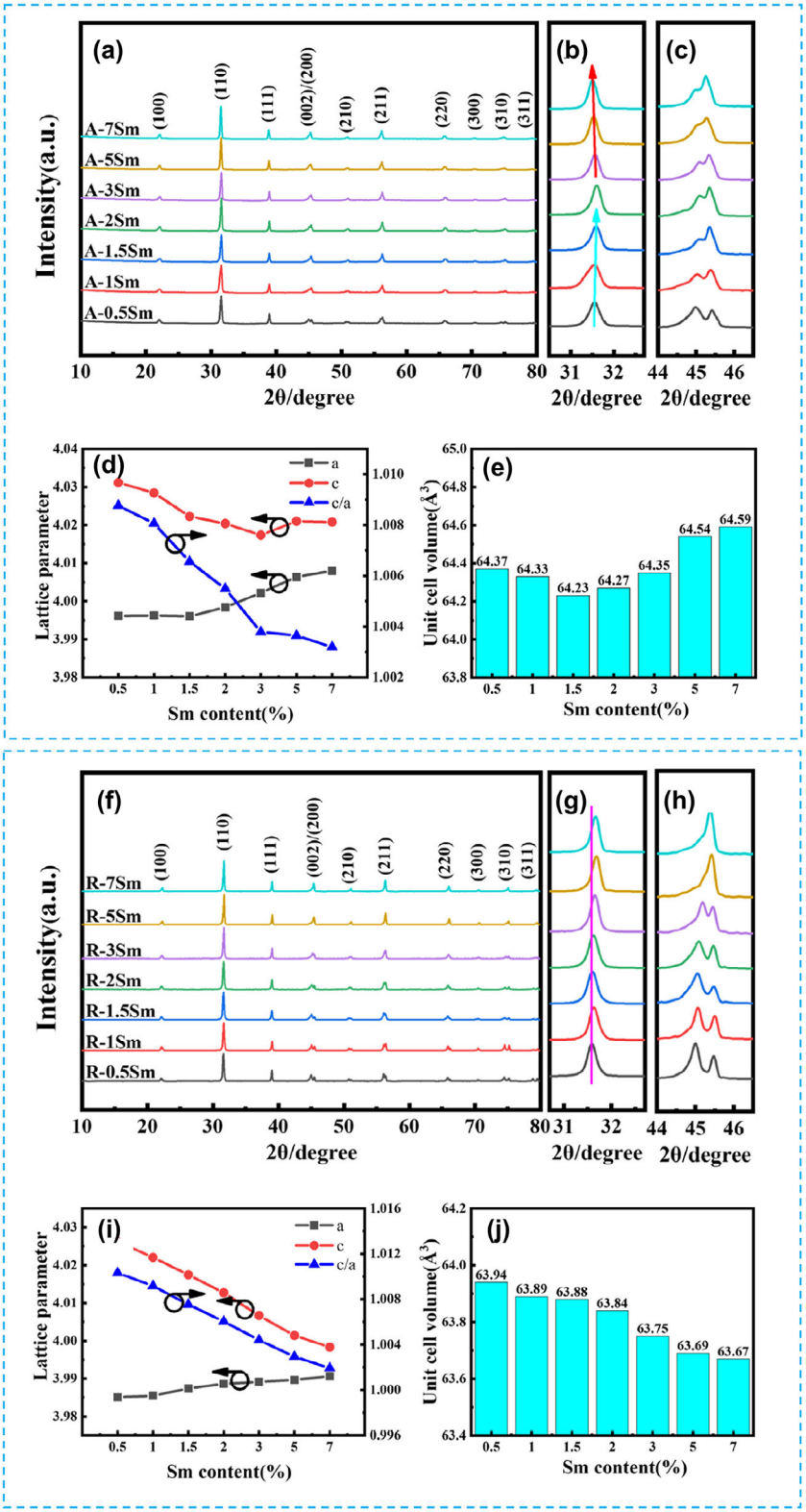


**Figure 8.** a) Cascade PXRD patterns of A-*x*Sm samples, b,c) the enlarged PXRD patterns of A-*x*Sm ceramics in selected $^{\circ}2\theta$ range, d) lattice parameters of A-*x*Sm samples as a function of Sm-doping level, and e) unit cell volume of A-*x*Sm samples as a function of Sm-doping level, f) cascade PXRD patterns of R-*x*Sm samples, g,h) the enlarged PXRD patterns of R-*x*Sm ceramics in selected $^{\circ}2\theta$ range, i) lattice parameters of R-*x*Sm samplesas a function of Sm-doping level and j) unit cell volume of R-*x*Sm samples as a function of Sm-doping level. Modified with permission.[185] Copyright 2023, Elsevier.

**Table 1.** List of space groups, lattice parameters, cell volumes, phase compositions, and theoretical densities of $Ba_{1-x}Nd_{2x/3}TiO_3$.[203]

| x | s. g. | Lattice metrics [Å] | | c/a | $V_{cell}$ [Å$^3$] | Phase composition [vol%] | Theoretical density [g cm$^{-3}$] |
|---|---|---|---|---|---|---|---|
| | | a = b | c | | | | |
| 0 | P4mm | 3.9936 | 4.0368 | 1.0108 | 64.3815 | T: 80.65 | 6.015 |
| | Pm3m | 4.0109 | | 1.0000 | 64.5247 | C: 19.35 | 6.002 |
| 0.02 | P4mm | 3.9963 | 4.0266 | 1.0076 | 64.3076 | T: 85.47 | 6.001 |
| | Pm3m | 4.0073 | | 1.0000 | 64.3488 | C: 14.53 | 5.997 |
| 0.04 | P4mm | 3.9976 | 4.0214 | 1.0060 | 64.2648 | T: 89.00 | 5.984 |
| | Pm3m | 4.0029 | | 1.0000 | 64.1415 | C: 11.00 | 5.995 |
| 0.06 | P4mm | 3.9988 | 4.0124 | 1.0034 | 64.1589 | T: 90.29 | 5.978 |
| | Pm3m | 4.0014 | | 1.0000 | 64.0660 | C: 9.71 | 5.981 |
| 0.08 | Pm3m | 4.0000 | | 1.0000 | 63.9986 | C: 100.00 | 5.966 |
| 0.10 | Pm3m | 3.9982 | | 1.0000 | 63.9146 | C: 100.00 | 5.952 |
| 0.15 | Pm3m | 3.9947 | | 1.0000 | 63.7480 | C: 100.00 | 5.914 |
| 0.20 | Pm3m | 3.9931 | | 1.0000 | 63.6703 | C: 100.00 | 5.868 |

ferent atmospheres on the microstructure, defect development and electrical characteristics of BTO ceramics were studied. With increasing Sm concentration, the phase structure of the ceramics sintered in air (A-*x*Sm) (Figure 8a–e) and in a reducing atmosphere (R-*x*Sm) (Figure 8f–j) shifted from tetragonal to cubic, with R-*x*Sm ceramics exhibiting a stronger cubic phase. It was found that the environment has a significant impact on Sm replacement sites and that defect evolution varies with the level of doping. $Sm^{3+}$ replaces the $Ba^{2+}$ ions and generates electrons that promote the transition from $Ti^{4+}$ to $Ti^{3+}$, thereby increasing the dielectric constant ($> 10^4$) and producing semiconductor-like properties. With increasing doping, $Sm^{3+}$ replaces the $Ti^{4+}$ ions, which leads to oxygen vacancies that trap space charges and lower the $Ti^{3+}$ concentration (Equation 18).

At the same time, the test of thermally stimulated depolarization currents confirms that the oxygen vacancies mainly trap space charges, with only a small fraction of the O vacancies forming defect dipoles $[2Sm'_{Ti} - V^{\bullet\bullet}_{O}]$. The R-*x*Sm ceramic differs from the A-*x*Sm ceramic in that Sm has no obvious substitution behavior for the $Ti^{4+}$-site. Since oxygen is easily ejected in a reducing environment, numerous oxygen vacancies and free electrons are created. The R-*x*Sm ceramic has a smaller cell volume compared to the A-*x*Sm ceramic, as more oxygen vacancies are created.

$$Sm_2O_3 \rightarrow 2Sm'_{Ti} + 3O_{o+}V^{\bullet\bullet}_{O} \quad (20)$$

$$Sm_2O_3 \rightarrow 2Sm_{Ba} + 2O_{o+}2e' + 1/2O_2 \quad (21)$$

Structural and defect analysis of Sm-doped BTO ceramics sintered in different atmospheres showed the preferential replacement of the Ba-site by Sm ions in air. With increasing doping, Sm ions eventually replace the Ti-sites. However, in a reducing environment, Sm ions largely replace the Ba-site in all samples (Equation 21). The O vacancy absorbs the electrons generated by the Sm ions, which replace the Ba-site, resulting in a decrease in the percentage concentration. The complex impedance test showed that the change in resistivity of the A-*x*Sm ceramics is mainly due to the effects of Sm-doping on the grain rather than the grain boundary of BTO. Donor doping and a reducing environment led to a significant $Ti^{3+}$ concentration in R-*x*Sm ceramics, giving them semiconductor-like properties.

Feng et al. investigated the effects of $Sm^{3+}$-doping on the defect structures, ferroelectric polarization, and electrocaloric properties of $(Ba_{1-1.5x}Sm_x)TiO_3$ ceramics ($x = 0.00 - 0.06$) prepared by solid-state sintering.[232] In $Sm^{3+}$-doped BTO at A-sites, the Ba/Ti ratio is less than 1, and the mechanisms of charge balance mainly depend on the Ba/Ti ratio. As the Ba/Ti ratio approaches 0.99, the primary charge balance occurs through electrons (Equation 22).[40] As the doping concentration increases, the Ba/Ti ratio decreases and Ba vacancies are formed for charge balance (Equation 23). It should also be noted that a small amount of $Sm^{3+}$ may have entered the B-sites. Substitution of the $Ti^{4+}$-sites with $Sm^{3+}$ reduces the positive charge and increases the volume at the same time. In this case, O vacancies are created to balance for the charge (Equation 24). The O vacancies can also occur during the sintering process (Equation 25). **Figure 9a** depicts a schematic

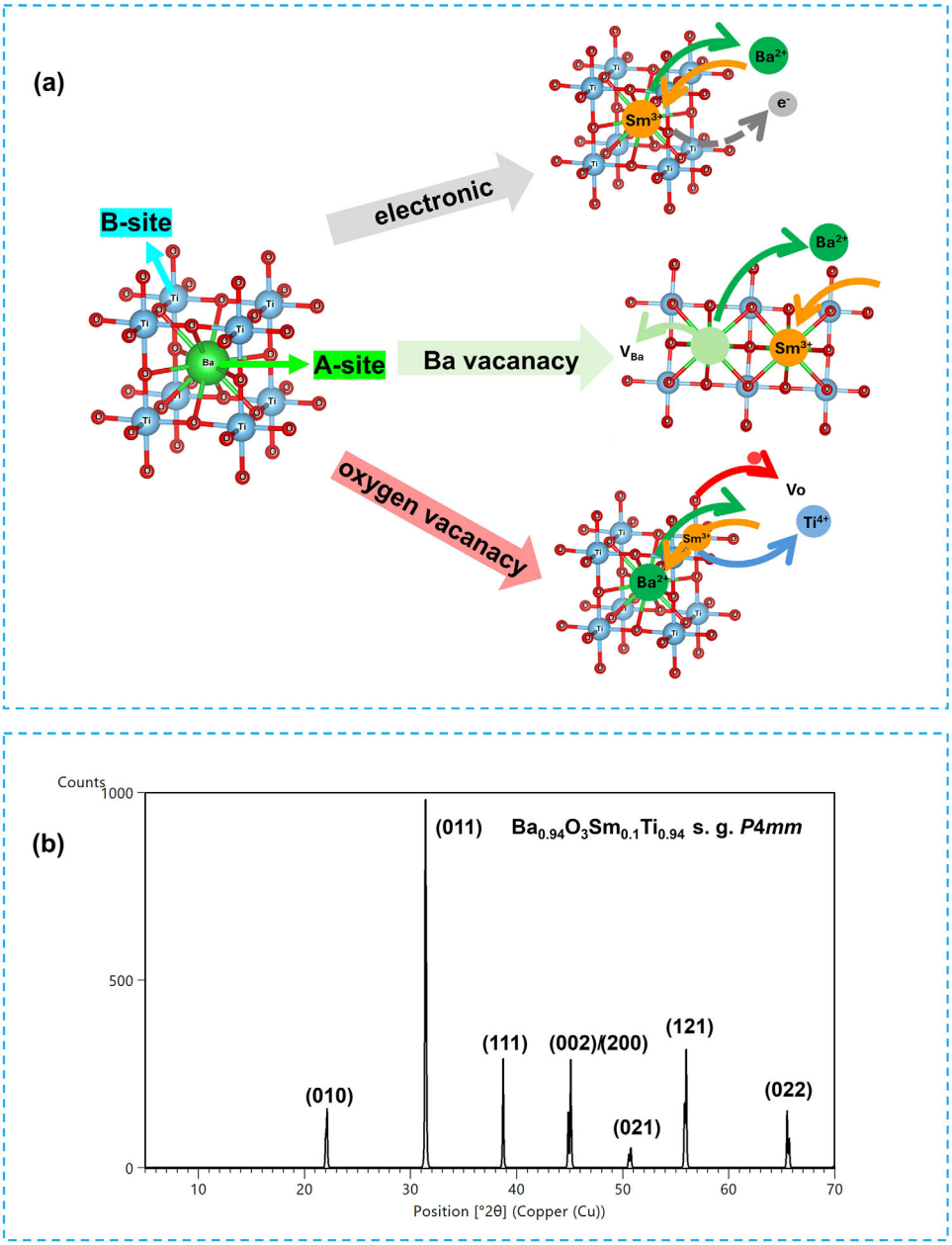


**Figure 9.** a) Charge compensation mechanisms depending on the $Sm^{3+}$-doping sites and b) tetragonal symmetry of $Ba_{0.94}O_3Sm_{0.1}Ti_{0.94}$ – $Sm^{3+}$ ions act as both a donor and acceptor in BTO.[231]

layout of the potential charge compensation mechanisms when $Sm^{3+}$ enters the BTO host.

$$Sm_2O_3+2TiO_2 \rightarrow 2Sm^{\bullet}_{Ba}+2Ti^{x}_{Ti}+6O^{x}_{O}+|1/2O_2+2e^{-} \quad (22)$$

$$Sm_2O_3+2TiO_2 \rightarrow 2Sm^{\bullet}_{Ba}+2Ti^{x}_{Ti}+6O^{x}_{O}+1/2O_2 + V'_{Ba} \quad (23)$$

$$Sm_2O_3+2BaO \rightarrow 2Sm'_{Ti}+2Ba^{x}_{Ba}+5O^{x}_{O}+V^{\bullet\bullet}_{O} \quad (24)$$

$$O^{x}_{O} \rightarrow 1/2O_2+V^{\bullet\bullet}_{O}+2e^{-} \quad (25)$$

All $(Ba_{1-1.5x}Sm_x)TiO_3$ samples exhibited a typical perovskite structure (Figure 9b), indicating that $Sm^{3+}$ has entered the BTO lattice. The diffraction peak around 45° 2$\theta$ showed split peaks at $x = 0.00 -0.03$, indicating the formation of a tetragonal phase. As $x$ increases, the split peaks gradually merge into a single peak at $x = 0.04–0.06$, indicating a phase transition from tetragonal to cubic symmetry. In addition, the position of the diffraction peak shifts to a higher angle ($x \leq 0.05$), suggesting a smaller cell volume. However, at $x = 0.06$, the diffraction peak changes back to a low angle, suggesting that additional $Sm^{3+}$ ions occupy the B-sites and increase the cell volume. According to Feng et al. the tetragonality ($c/a$) decreases with increasing $x$, which is

consistent with previous reports.[39,114,176,233–236] The cell volume decreased ($x < 0.05$) and then increased at $x = 0.06$, which is consistent with the XRD data and shows the tendency for substitution of $Sm^{3+}$ in the B-sites at this concentration. Furthermore, there was a significant correlation between the microstructure and level of doping. Pure BTO has a high grain size of about 64.6 μm at $x = 0.00$. However, the lattice distortion caused by $Sm^{3+}$-doping significantly reduces the grain size. For $x > 0.00$, the average grain size is about 0.68 μm at $x = 0.01$. The average grain size increases to ≈1.22 μm at $x = 0.02$ and ≈1.78 μm at $x = 0.05$. This is likely due to the change from electron compensation to Ba-vacancy compensation. The resulting vacancy defects could increase ion mobility during the sintering process and promote grain development. However, the formation of more defects could limit grain growth.[237] If $x = 0.06$, the average grain size is reduced to ∼1.06 μm. At this doping concentration, O vacancies form when more $Sm^{3+}$ ions occupy the B-sites. This leads to a larger lattice distortion and ultimately to a decrease in grain size, as the lattice distortion inhibits the migration of the grain boundaries. The incorporation of $Sm^{3+}$ at $Ba^{2+}$-sites generates an excess positive charge. The charge compensation can be achieved by generating electrons (Equation 22), Ba vacancies (Equation 23), and reducing the concentration of O vacancies. However, the incorporation of $Sm^{3+}$ at $Ti^{4+}$-sites leads to an excess of negative charge, resulting in O vacancies. Sakaguchi et al. also reported on the O defect chemistry of $(Ba_{1-x}Sm_x)TiO_3$ and showed that there is a significant reduction in O vacancies when $Sm^{3+}$ is incorporated at the B-sites of the BTO host.[238] Park and Han demonstrated a significant correlation between the preparation method and the crystal structures of the nominal composition of $(Ba_{1-x}Sm_x)TiO_3$.[223] The standard procedure, in which the starting powders are combined and calcined several times, did not lead to the expected nominal composition, in which $Sm^{3+}$ predominantly occupies Ti-sites, even at the Ba-deficient composition (Ba/Ti < 1). In contrast, $Sm^{3+}$ occupies the Ba-site in the samples synthesized by the liquid mixture method. Kang et al. also investigated how the addition of $Sm_2O_3$ affects the dielectric and energy storage properties of BTO.[239] It was discovered that in BTO ceramics prepared by a solid-state reaction and having varying amounts (0.25, 0.5, 1.0, and 2.5 mol%) of $Sm_2O_3$, increasing the degree of Sm-doping resulted in a reduction in tetragonality and very slight grain development. The tetragonality and grain development decreased, lowering the $T_c$ value and increasing the dielectric constant at RT. The sample with 2.5 mol% $Sm_2O_3$ has the best dielectric properties and more than twice the dielectric constant of pure BTO. This is because smaller $Sm^{3+}$ ions and O vacancies can cause lattice contraction, which decreases the lattice constant. Furthermore, oxygen vacancies can promote atomic volume diffusion. The increased addition of $Sm_2O_3$ improves the sinterability and at the same time increases the density and particle size. In general, the influence on the grain size is determined by the concentration of the Sm used for doping. At low concentrations, Sm can promote grain growth, while at higher concentrations it can affect grain size in different ways, depending on the type of ceramic matrix, Sm content, and synthesis conditions. Overall, $Sm^{3+}$ dopants can have a significant impact on the microstructure and morphology of BTO ceramics, which is reflected in grain growth, reduced grain size, optimal concentration, and sintering conditions.

### 2.6. The Case of Eu-Doped BTO

The Ln series places europium, Eu, between Sm and Gd, suggesting that it may also have a small amphoteric property like that of Gd. For a CN = 12, $Ba^{2+}$ has an ionic radius of 1.610 Å, while $Ti^{4+}$ has an ionic radius of 0.605 Å for CN = 6. For CN = 6 and CN = 9, the intermediate radius of $Eu^{3+}$ is 0.947 Å and 1.12 Å, respectively.[43] With these values, $Eu^{3+}$ can theoretically occupy both sites. Nevertheless, the distribution of Eu dopants in the lattice remains a topic of discussion. Some studies suggest that $Eu^{3+}$ ions occupy the $Ba^{2+}$-sites, while others conclude that it occupies both $Ba^{2+}$- and $Ti^{4+}$-sites based on electrical measurements, luminescence analysis, and XRD data.[84,240–242] There is no question that valence also influences site occupancy and defect chemistry. It is also known that Eu ions can exist in both +3 and +2 metastable states.[241] However, there is no evidence that the amphoteric character of Eu is affected by a change in valence.[243] These two valence states, $Eu^{2+}$ and $Eu^{3+}$, can coexist at A-sites. When $Ba^{2+}$ is replaced by $Eu^{3+}$, a charge imbalance occurs. In order to achieve charge neutrality, this charge imbalance must be balanced either by the formation of vacancies or by the formation of electrons. The formation of vacancies/electrons can change the local symmetry or conductivity of the BTO host. These changes are often reflected in the structural, optical, and dielectric properties.

Recently, Padalia et al. provided the mechanisms underlying the introduction of $Eu^{3+}$ into the BTO host as $Ba_{1-3x/2}Eu_xTiO_3$ ($x = 0$, 0.005, 0.015 and 0.025) prepared by solid-state route.[243] The XRD and optical spectroscopy experiments revealed the substitution of $Ba^{2+}$ by $Eu^{3+}$ at the A-site, leading to a contraction of the cubic lattice metric. Moreover, dielectric analysis revealed the coexistence of $Eu^{2+}$ and $Eu^{3+}$ at the A-sites in a metastable state. From a microstructural point of view, it was observed that the infusion of $Eu^{3+}$ improves the microstructure of BTO, increases the grain size, and reduces the impedance at the grain boundaries. Better grain boundary quality enables smoother polarization processes and lower dielectric losses, resulting in a stable dielectric constant over a wide frequency range. The presence of Eu dopants can either hinder or accelerate grain development, depending on the amount, processing conditions, and environment during sintering. It should not be disregarded that changes in grain size are also dictated by the sintering temperature and time, since these parameters usually impact grain formation independently of doping. The $Eu^{3+}$ ions can occupy lattice sites or form vacancies and thus influence the diffusion pathways and energy barriers for grain development. For example, Sasikumar et al. reported the decrease in grain size with the increase in $Eu^{3+}$-doping level of $Ba_{1-x}Eu_xTiO_3$ ($x = 0.00$, 0.02, 0.04, 0.06) prepared by mixed oxide solid-state sintering.[244] In contrast, Maneeshya et al. found that grain growth increased with doping concentration in (0–5 wt%) $Eu^{3+}$-doped BTO thin films produced on quartz substrates using magnetron sputtering.[245] In their study, Lu et al. found that $Ba_{1-x}Eu_xTi_{1-x/8}O_3$ ($x = 0.01$–0.05) prepared by standard ceramic processing had low porosity and a grain size ranging from 0.7 to 1.0 μm.[242]

Rabuffetti et al. investigated the local structure of $x$Eu:$BaTiO_3$ nanocrystals ($x = 0$–5 mol%) prepared by sol-gel chemistry, while the solubility limit of $Eu^{3+}$ in the BTO host was expected to be ≈4 mol%.[84] The incorporation of 1 mol% Eu led to a decrease in the

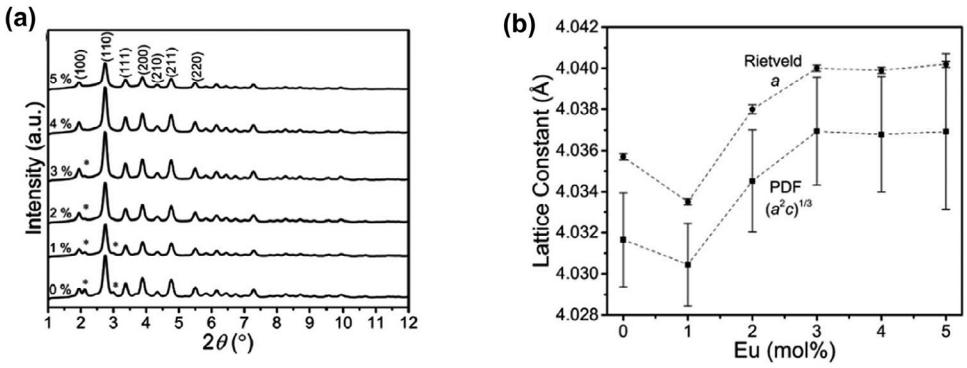


**Figure 10.** a) Cascade XRD patterns of Eu-doped BTO nanocrystals, showing cubic symmetry, along with the nominal Eu concentrations indicated on the left, b) evolution of lattice constants $(a^2c)^{1/3}$ and $a$ according to PDF and Rietveld analysis, respectively. Modified with permission.[84] Copyright 2014, The Royal Society of Chemistry.

volume of the perovskite unit cell, while concentrations between 1 and 3 mol% led to an increase. Namely, the perovskite phase was indexed to a unit cell with cubic *Pm*-3*m* symmetry with $a$ ≈4.03 Å. On the other hand, the local crystal structure of Eu-doped BTO was investigated by PDF analysis of X-ray total scattering data. The experimental PDFs were modeled in the range of interatomic distances of 1.5–20 Å using the non-centrosymmetric, tetragonal s. g. *P*4*mm*, since previous structural studies of BTO nanocrystals below 10 nm revealed the presence of local tetragonal distortions due to an off-centered Ti atom.[246,247] $Eu^{3+}$-doping showed a non-centrosymmetric, ninefold coordination environment. The mean Eu–O distance and Eu CN decreased from 2.46 Å and 9.9 to 2.42 Å and 8.6 for Eu concentrations of 1 and 5 mol%, respectively. Analysis of these results showed that the local crystal structure of the Eu-doped BTO was characterized by a tetragonal *P*4*mm* symmetry. The parameters of the tetragonal unit cell and the degree of Ti off-centering remained quite stable over the whole range of Eu concentration. The average lattice constant $(a^2c)^{1/3}$ showed a clear correlation with the Eu content (**Figure 10**).

Figure 10b clearly shows three regimes. At nominal concentrations in the range of 0 – 1 mol%, the introduction of Eu leads to a contraction of the perovskite unit cell. The addition of increasing amounts of Eu up to 3 mol% leads to an enlargement of the unit cell metrics. A similar tendency was observed when the average crystal structure of Eu-doped BTO nanocrystals was refined using the Rietveld method with the centrosymmetric cubic symmetry (s. g. *Pm*3*m* ). The strong correlation between the PDF analysis (**Table 2**) and the Rietveld refinement indicates that the variations of the lattice constant are unaffected by the structural model and length scale used in the refinement.

The measured volume changes showed that Eu was integrated into the BTO host within the concentration range of 0 – 3 mol%. The change in unit cell volume with Eu concentration is consistent with the substitution of $Eu^{3+}$ for $Ba^{2+}$ by the formation of a $Ti^{4+}$ vacancy at concentrations below 1 mol% and with the substitution of $Eu^{3+}$ for both $Ba^{2+}$ and $Ti^{4+}$ at concentrations between 1 and 3 mol%. Finally, the volume of the unit cell remains relatively stable at concentrations above 3 mol%, suggesting that Eu does not enter the BTO host. In addition, the results of X-ray total scattering, steady-state PL, and X-ray absorption spectroscopy (XAS) measurements were examined in relation to the distribution of $Eu^{3+}$ dopants in the BTO bulk in the context of the defect chemistry models established by Freeman and colleagues.[88,91]

Freeman et al. demonstrated that the size and charge mismatch between the Ln and alkaline earth and the simultaneous formation of a $Ti^{4+}$ vacancy, lead to significant structural relaxations of the perovskite lattice surrounding the Ln ion.[91] The inability of the smaller Ln ion to fulfill the twelvefold coordination of the larger $Ba^{2+}$ leads to a ninefold coordination with a reduced average Ln–O distance. The structural trends were found to be consistent with the substitution of $Ba^{2+}$ by $Eu^{3+}$ via the creation of a $Ti^{4+}$ vacancy at low Eu concentrations (<1 mol%) and with the substitution of $Ba^{2+}$ and $Ti^{4+}$ by $Eu^{3+}$ at high Eu concentrations (1–3 mol%).

**Figure 11a** shows a ternary composition triangle indicating the different ionic compensation mechanisms available and the position of the corresponding solid solutions as follows:[248]

i. $(Ba_{1-3x}Eu_{2x})TiO_3$, with the formation of $Ba^{2+}$ vacancies and the occupation of $Ba^{2+}$-sites by $Eu^{3+}$ ions.
ii. $(Ba_{1-x}Eu_x)Ti_{1-x/4}O_3$, with formation of $Ti^{4+}$ vacancies and $Eu^{3+}$ ions occupying $Ba^{2+}$-sites.
iii. $(Ba_{1-x}Ti_{1-x}Eu_{2x})O_3$, with double substitution of $Eu^{3+}$ at both $Ba^{2+}$- and $Ti^{4+}$-sites.
iv. $Ba(Ti_{1-x}Eu_x)O_{3-x/2}$, with the formation of O vacancies and the occupation of $Ti^{4+}$ sites by $Eu^{3+}$ ions.

To date, however, no precise studies have been described that distinguish between these compensation processes and the associated defect structures. In addition to these ionic compensation mechanisms, it is crucial to investigate electronic compensation mechanisms in which the valence state of Ti and/or Eu could change depending on the synthesis conditions. Serna-Gallén et al. investigated the $Eu^{3+}$-doped BTO ceramics with dopant concentrations between 0 and 10 mol%, prepared by sol–gel synthesis based on the nominal compositions $(Ba_{1-3x}Eu_{2x})TiO_3$ and $Ba(Ti_{1-x}Eu_x)O_{3-x/2}$, where two possible substitution mechanisms were studied (**Table 3**).[248] In particular, the XRD patterns of the heated samples exhibited a tetragonal symmetry (Figure 11b,c). According to the values of the ionic radii, the volume of the unit cell shrinks when $Eu^{3+}$ occupies the $Ba^{2+}$-site, while it increases when it occupies the $Ti^{4+}$-site.[39]

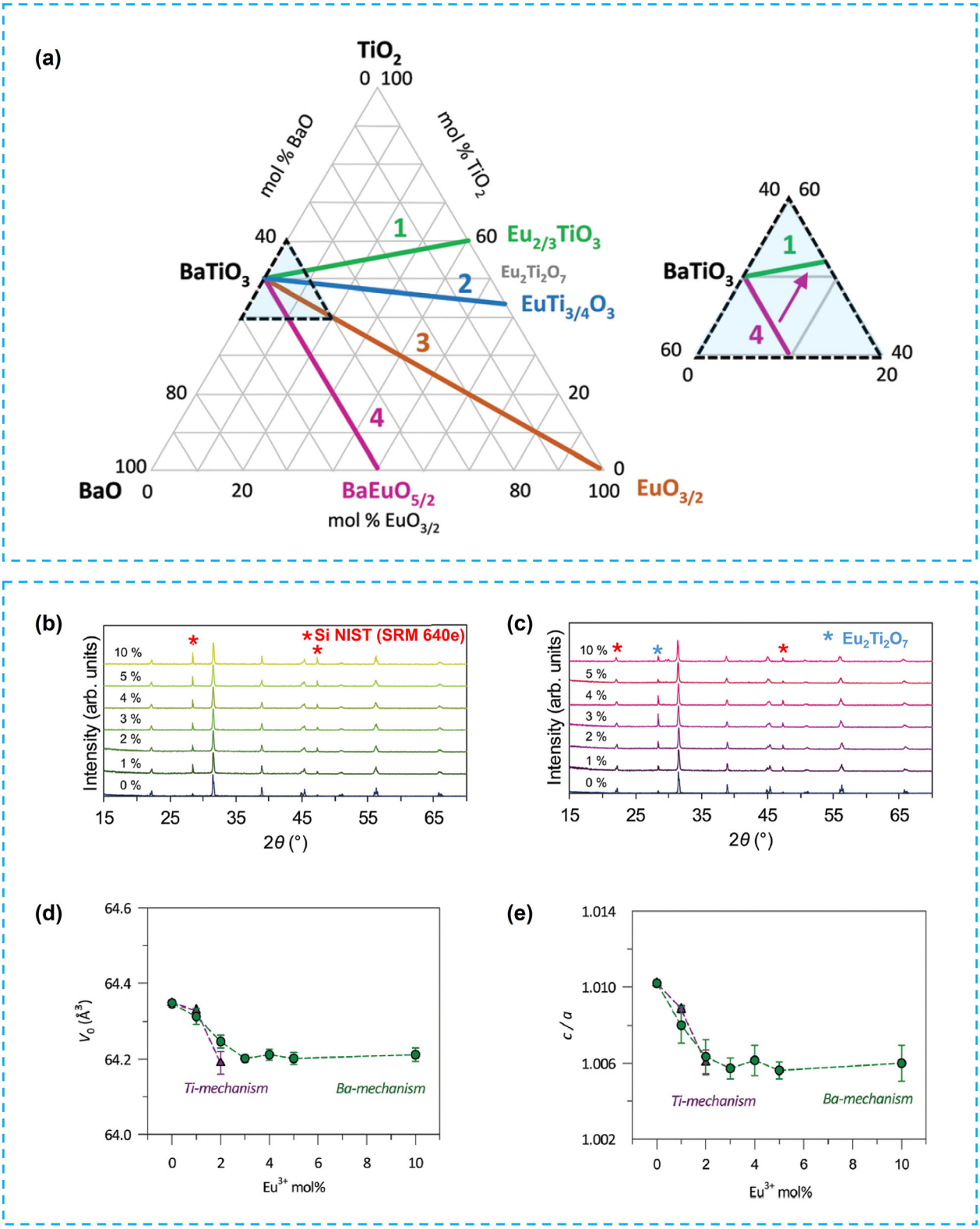


**Figure 11.** a) A ternary composition triangle illustrating the locations of potential ionic compensation processes, cascade XRD patterns of b) Ba-mechanism and c) Ti mechanism, evolution of c) $V_0$ and d) $c/a$ with $Eu^{3+}$ concentration for Ba and Ti-mechanisms. The inset in (a) depicts a possible method for obtaining samples from join 4 towards join 1. Modified with permission.[248] Copyright 2019, The Royal Society of Chemistry.

**Table 2.** Structural parameters of Eu-doped BTO nanocrystals from PDF analysis.[84]

| $x$ [Eu mol%] | Lattice metrics [Å] | | $c/a$ | $V_{cell}$ [Å$^3$] | $d_{Ti}$ [Å] | $R_w$ [%] |
|---|---|---|---|---|---|---|
| | $a = b$ | $c$ | | | | |
| 0 | 4.014(2) | 4.067(5) | 1.0132(14) | 65.53(11) | 0.134(19) | 13.7 |
| 1 | 4.013(2) | 4.065(5) | 1.0131(12) | 65.47(10) | 0.141(16) | 14.8 |
| 2 | 4.017(3) | 4.069(6) | 1.0130(15) | 65.79(13) | 0.141(19) | 14.3 |
| 3 | 4.020(3) | 4.071(6) | 1.0128(16) | 65.78(14) | 0.14(2) | 14.1 |
| 4 | 4.020(3) | 4.071(6) | 1.0126(17) | 65.78(14) | 0.14(2) | 14.3 |
| 5 | 4.020(4) | 4.071(9) | 1.013(2) | 65.79(19) | 0.15(3) | 17.4 |

The evolution of the volume and tetragonality with $Eu^{3+}$ concentration follows the same trend (see **Table 4** and Figure 11d,e). These results indicate that $Eu^{3+}$ ions have a solubility limit of ≈3 mol% in compositions with Ba-mechanisms, which is consistent with previous studies.

The Ba-mechanism shows a decrease in volume up to 3 mol% $Eu^{3+}$, indicating that the $Eu^{3+}$ dopants occupy the $Ba^{2+}$-site. The volume remains constant at ≥ 3 mol% concentrations, indicating that no new dopant enters the BTO host. In the samples of the Ti-mechanism, join 4, a progressive decrease in volume of up to 2 mol% was observed, demonstrating the affinity of Eu ions for the $Ba^{2+}$-site. However, the Ti-mechanism should lead to an increase in volume and not to a decrease in volume, as in the case described by Serna-Gallén et al. In addition, Ba losses have been reported in the literature when doping perovskite-type structures with the general formula $ABO_3$.

Apart from the studied solubility limit of $Eu^{3+}$ ions in BTO samples and the preference of $Eu^{3+}$ to occupy $Ba^{2+}$-sites, regardless of the nominal composition and substitution mechanism, Serna-Gallén et al. highlighted the amphoteric behavior of $Eu^{3+}$ in BTO, but with the proviso that the substitution occurs mainly at the Ba-site. The literature shows that significant changes in the electrical and magnetic properties of the material depend on the site occupation of the dopants. The presence of multiple crystallographic sites for $Eu^{3+}$ ions can significantly influence both the optical properties of BTO ceramics and their diverse electrical properties and applications in devices.

It should be emphasized that pure BTO has a temperature-dependent optical bandgap, which is valuable for the development of novel thermometers based on the excitation intensity ratio (EIR).[249,250] However, to date, this property of BTO has not been exploited, despite the extensive studies on Ln-doped BTO for luminescence thermometry, e.g., $Eu^{3+}$:BTO.[251–253] Only recently, research on $Eu^{3+}$-doped BTO for EIR thermometry was conducted by Xing et al.[254] The $Ba_{1-x}Eu_xTi_{1-x/4}O_3$ ($x = 0$, 0.005, 0.01, 0.02, 0.03, and 0.04) was prepared by the high-temperature solid-state reaction and the influence of $Eu^{3+}$ concentration on the structural and optical properties was investigated in terms of an amphoteric substitution property of $Eu^{3+}$ for $Ba^{2+}/Ti^{4+}$-sites within the tetragonal *P4mm* lattice. The underlying mechanism was explained by the competitive absorption of the BTO host towards $Eu^{3+}$ ions due to the decreasing band gap with increasing temperature. The amphoteric nature of $Eu^{3+}$ dopants was attributed in part to the need for local charge compensation and a reduction in lattice energy. Alternatively, vacancies or interstitial species may develop to achieve local charge balance, leading to an increase in lattice energy. Xing et al. suggested that $Ti^{3+}$ as a co-dopant could facilitate the occupation of $Eu^{3+}$ ions at the $Ba^{2+}$-site, as $Ti^{4+}$-site is preferentially occupied due to its small ionic size.

Ferroelectric BTO has been observed to undergo a transition from insulating to metallic, semiconducting, or semimetallic after electron doping or the formation of O vacancies.[255] One example is the study by Aslla-Quispe et al., which showed that the addition of Eu at the Ba-site of the BTO lattice reduces the band gap energy.[256] Furthermore, Chi et al. reported the presence of a metal-insulator transition in Eu-doped BTO at low temperatures.[257] They proposed that significant electrical correlations and Eu–O–Ti hybridizations cause this behavior. Sim-

**Table 3.** Nominal compositions of the different synthesized materials in Ba- and Ti- mechanism and the abbreviations used according to Serna-Gallén et al.[248]

| Mechanism | Sample | Nominal formula | $x$ | $Eu^{3+}$ mol% |
|---|---|---|---|---|
| Ba-mechanism | 0%-BTO | $BaTiO_3$ | 0 | 0 |
| $(Ba_{1-3x}Eu_{2x})TiO_3$ | 1%-Ba | $(Ba_{0.985}Eu_{0.01})TiO_3$ | 0.005 | 1 |
| | 2%-Ba | $(Ba_{0.97}Eu_{0.02})TiO_3$ | 0.01 | 2 |
| | 3%-Ba | $(Ba_{0.955}Eu_{0.03})TiO_3$ | 0.015 | 3 |
| | 4%-Ba | $(Ba_{0.94}Eu_{0.04})TiO_3$ | 0.02 | 4 |
| | 5%-Ba | $(Ba_{0.925}Eu_{0.05})TiO_3$ | 0.025 | 5 |
| | 10%-Ba | $(Ba_{0.85}Eu_{0.10})TiO_3$ | 0.05 | 10 |
| Ti-mechanism | 1%-Ti | $Ba(Ti_{0.99}Eu_{0.01})O_{2.995}$ | 0.01 | 1 |
| $Ba(Ti_{1-x}Eu_x)O_{3-x/2}$ | 2%-Ti | $Ba(Ti_{0.98}Eu_{0.02})O_{2.990}$ | 0.02 | 2 |
| | 3%-Ti | $Ba(Ti_{0.97}Eu_{0.03})O_{2.985}$ | 0.03 | 3 |
| | 4%-Ti | $Ba(Ti_{0.96}Eu_{0.04})O_{2.980}$ | 0.04 | 4 |
| | 5%-Ti | $Ba(Ti_{0.95}Eu_{0.05})O_{2.975}$ | 0.05 | 5 |
| | 10%-Ti | $Ba(Ti_{0.90}Eu_{0.10})O_{2.950}$ | 0.1 | 10 |

ilarly, Chaudhuri et al. observed a metal-insulator transition in $Eu_{0.3}Ba_{0.7}Ti_{1-x}Nb_xO_3$ at $x = 0.1$ due to the shielding effect of localized Eu-4*f* electrons and band modulation.[258] However, ferroelectricity in BTO can be easily removed by pressure, electron doping, impurities, and defects or by surface effects of small particles and thin coatings.[259,260] Metallic conductivity can be achieved in Ln-doped BTO and can increase under high pressure. At high pressure, Ln-doped BTO can also exhibit ferroelectric, metallic, or semi-metallic properties. To answer these questions, it is crucial to understand the structural properties of Ln-doped BTO under high pressure, which have been relatively rarely studied.

Recently, Sahu et al. investigated the crystal structure and dielectric properties of $Ba_{1-x}Eu_xTiO_3$ ($x = 0.05$) synthesized by the conventional solid-state reaction route and performed XRD measurements up to 16 GPa (**Figure 12a**).[261] Eu-doped BTO crystallizes in tetragonal (s.g. *P*4*mm*) symmetry, at ambient pressure. Yet, the Rietveld refinements showed a coexistence of cubic (s.g. *Pm*-3*m* ) and tetragonal (s.g. *P*4*mm*) symmetries above 1.4 GPa. The reduction in the volume of the unit cell indicates a partial substitution of $Ba^{2+}$ by $Eu^{3+}$. Eu ions can occupy both Ba- and Ti-sites and possibly form self-compensating clusters of $Eu^{3+}$ at $Ba^{2+}$-sites and $Eu^{3+}$ at $Ti^{4+}$-sites within the BTO lattice, leading to an increased volume of the unit cell compared to undoped BTO (Figure 12b). A coexistence model resulted in a composition of 72% cubic and 28% tetragonal phases at 2 GPa (Figure 12c). In the tetragonal phase, the most notable change in crystal structure under pressure was the change in all six Ti–O bond lengths within the $TiO_6$ octahedra. The four corresponding in-plane (*xy*-plane) Ti–O bond lengths showed a linear decrease of −0.003 Å/GPa with increasing pressure up to the maximum pressure value.

In contrast, the other two Ti–O bond lengths along the *c*-axis showed opposite behavior under pressure. The substantial Ti–O bond distance along the *c*-axis decreased with pressure, showing a decrease from −0.03 Å/GPa to −0.015 Å/GPa at ≈3.1 GPa and −0.015 Å/GPa to −0.003 Å/GPa at ≈8.5 GPa. Conversely, the small Ti–O bond distance along the *c*-axis increased with pressure and exhibited remarkable slope variations of 0.019–0.009 Å/GPa and 0.009 to −0.0005 Å/GPa at ≈3.1 GPa and 8.2 GPa, respectively. The decrease in octahedral distortion was due to the pressure-driven decrease in tetragonality and was also confirmed by a decrease in the *c*/*a* ratio up to the same pressure. The decrease in octahedral distortion indicates a delocalization

**Table 4.** Unit cell parameters of $Eu^{3+}$-doped BTO samples.[248]

| Sample | Lattice metrics [Å] | | $V_{cell}$ [Å$^3$] |
|---|---|---|---|
| | $a = b$ | $c$ | |
| 0%-BT | 3.9937(3) | 4.0344(5) | 64.347(7) |
| 1%-Ba | 3.9959(12) | 4.0279(25) | 64.313(21) |
| 2%-Ba | 3.9967(12) | 4.0221(24) | 64.247(17) |
| 3%-Ba | 3.9966(8) | 4.0195(14) | 64.202(10) |
| 4%-Ba | 3.9962(12) | 4.0208(20) | 64.212(15) |
| 5%-Ba | 3.9967(5) | 4.0192(13) | 64.202(16) |
| 10%-Ba | 3.9964(14) | 4.0204(24) | 64.212(18) |
| 1%-Ti | 3.9951(3) | 4.0304(4) | 64.329(6) |
| 2%-Ti | 3.9959(9) | 4.0201(17) | 64.19(3) |

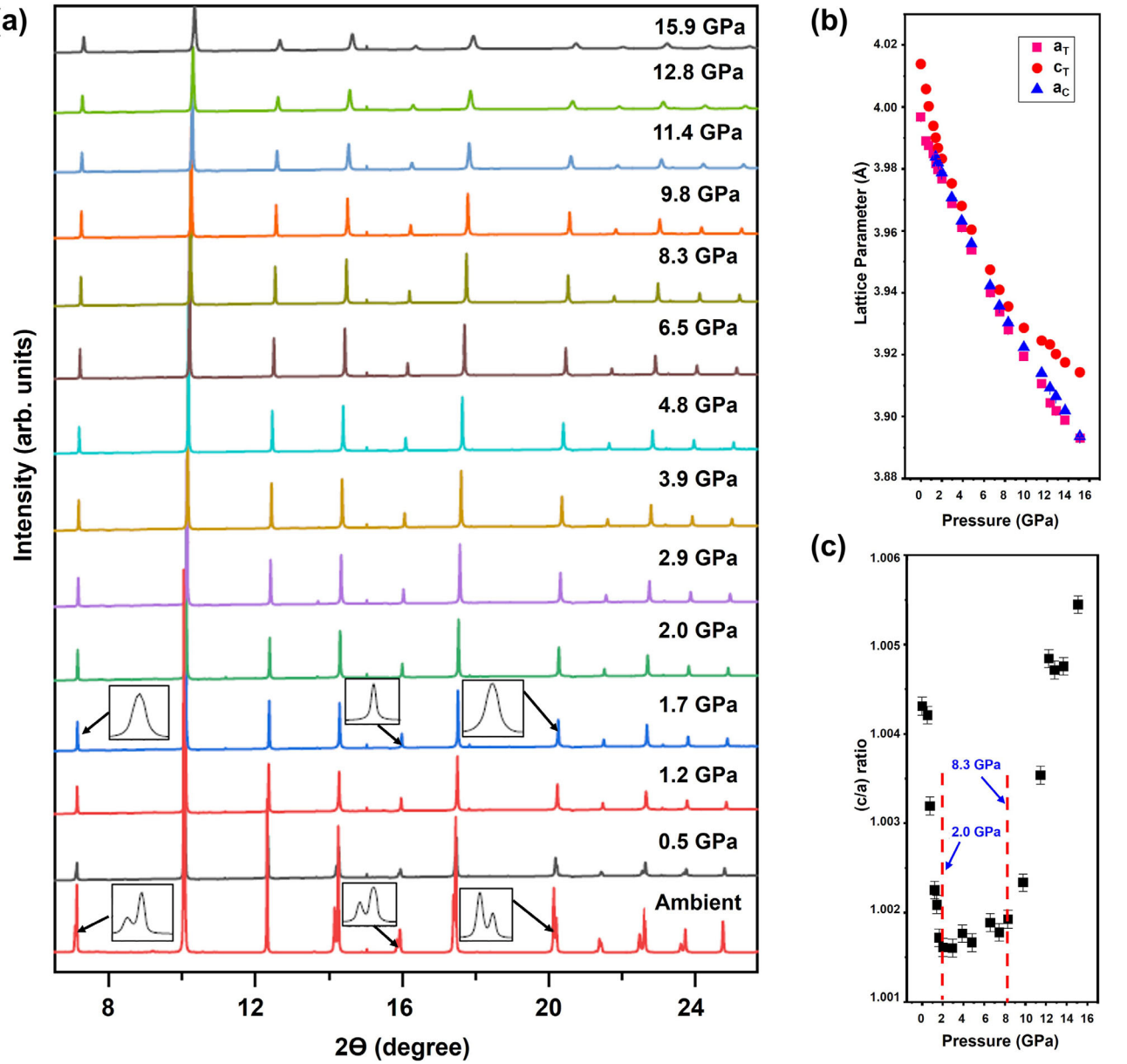


**Figure 12.** a) Cascade XRD patterns of Eu-doped BTO at selected pressures (insets show Bragg profiles indicating the transformation of the tetragonal phase into singlet at 1.7 GPa), b) evolution of the lattice parameters of Eu-doped BTO with pressure, c) pressure dependence of the *c*/*a* ratio. Modified with permission.[261] Copyright 2024, American Institute of Physics.

of charge in the system. It can be concluded that the octahedral distortion caused by the charge difference cannot be canceled by pressure, but that this distortion increases with pressure. The results of Sahu et al. show a ferroelectric-like semimetallic state in Eu-doped BTO at high pressure through detailed structural features at non-ambient conditions.

### 2.7. The Case of Gd-Doped BTO

While La-doped BTO has been intensively studied, the incorporation of gadolinium, Gd, into the BTO lattice has been little explored. In comparison, there are almost as many studies on Gd-doped BTO as on Sm- and/or Ho-doped BTO (see Figure 2). Gd is an amphoteric ion with a significant affinity for the A-site, as EPR and XRD studies have shown.[262,263] A reduced oxygen partial pressure during sintering further favors the occupation of A-site by amphoteric ions.[264] However, this property makes Gd less suitable for increasing the lifetime of MLCCs with base-metal electrodes. For example, Okamatsu et al. investigated the effects of Gd, Dy, Y, Yb, and Mg on the microstructure and reliability of BTO-based monolithic ceramic capacitors with Ni electrodes.[265] XRD analysis revealed that $Gd^{3+}$ (0.938 Å, CN = 6 and 1.107 Å, CN = 9) and $Dy^{3+}$ ions predominantly substi-

**Table 5.** Unit cell metrics and reliability factors of $BaTi_{1-x}Gd_xO_3$ ($0 \le x \le 0.06$) as obtained from the Rietveld refinement against PXRD data.[268]

| $x$ | 0.00 | 0.02 | 0.04 | 0.06 |
|---|---|---|---|---|
| s. g. | *P4mm* | *P4mm* | *P4mm* | *P4mm* |
| Unit cell metrics [Å] | $a = 3.99418(12)$<br>$b = 3.99418(12)$<br>$c = 4.03254(15)$ | $a = 3.99660(18)$<br>$b = 3.99660(18)$<br>$c = 4.02841(3)$ | $a = 4.00316(24)$<br>$b = 4.00316(24)$<br>$c = 4.01600(36)$ | $a = 4.00918(16)$<br>$b = 4.00918(16)$<br>$c = 4.01842(19)$ |
| $V_{cell}$ [Å$^3$] | 64.333(4) | 64.345(7) | 64.361(12) | 64.586(5) |
| Crystallite size [nm] | 38.47 | 41.23 | 45.93 | 40.25 |
| $c/a$ | 1.0096 | 1.0079 | 1.0032 | 1.0023 |
| Goldschmidt tolerance factor ($\tau$) | 1.0617 | 1.05819 | 1.0547 | 1.0512 |
| Theoretical density [gm cm$^{-3}$] | 6.012 | 6.155 | 6.234 | 6.218 |
| Ba1–O1 [Å] | 2.8246(2) | 2.8299(7) | 2.8336(7) | 2.8359(5) |
| Ti–O2 [Å] | 1.9992(4) | 1.9758(4) | 1.9642(9) | 1.9590(5) |
| < Ba–O–Ba > [°] | 161.13 | 162.84 | 163.42 | 164.20 |
| Reliability factors [%] | $R_p = 6.76$<br>$R_{wp} = 8.70$<br>$\chi^2 = 2$ | $R_p = 3.36$<br>$R_{wp} = 2.85$<br>$\chi^2 = 1.48$ | $R_p = 2.07$<br>$R_{wp} = 1.7$<br>$\chi^2 = 1.34$ | $R_p = 4.17$<br>$R_{wp} = 3.26$<br>$\chi^2 = 1.69$ |

tute at the $Ba^{2+}$-site, $Yb^{3+}$ ions exclusively at the $Ti^{4+}$-site, and $Y^{3+}$ ions occupy both sites. Tsur et al. studied $Gd^{3+}$-doped BTO ceramics and showed that $Gd^{3+}$ can occupy up to ≈5 at.% exclusively at the A-site and up to ≈3.75 at.% at the B-site or self-compensate up to ∼10 at.% at both sites.[39] They also observed anomalous trends in tetragonality (within the s.g. *P4 mm*), cell volume, and $T_c$ in A-site Gd-doped BTO ceramics compared to La-doped BTO. These deviations, which are due to the size discrepancy between Gd and Ba, are in contrast to the expected ionic radii and tolerance factors. Ben and Sinclair found that Ln dopants such as $Gd^{3+}$, $Ho^{3+}$, and $Er^{3+}$ induce lattice deformation that mitigates the decrease in $T_c$ associated with A-site size effects while acting as self-compensating dopants.[82] In particular, $Gd^{3+}$-doping of the A-site (i.e., in $Ba_{1-x}Gd_xTi_{1-x/4}O_3$) was shown to increase the $c/a$ ratio, cell volume, and $T_c$ value compared to $La^{3+}$-doping. The tetragonal $c/a$ ratio and cell volume of Gd-doped BTO were larger than those of La-doped BTO. In addition, the rate of $T_c$ decay was lower with $Gd^{3+}$ substitution (8 °C at%$^{-1}$) than with $La^{3+}$ substitution (24 °C at%$^{-1}$). Han et al. reported that Ln-doping at the Ba-site improves the ferroelectric properties of pure BTO by increasing the tetragonal ratio.[176] Similarly, Reddy et al. previously showed that the addition of $Gd^{3+}$ at the A-site of $Ba(Zr_{0.1}Ti_{0.9})O_3$ improves the dielectric properties of the BTO host.[266] Recently, Batoo et al. described co-doping of $Gd^{3+}$ and $Nb^{5+}$ at the $Ba^{2+}$- and $Ti^{4+}$-sites, respectively, which leads to improved dielectric properties due to the formation of defect dipoles and the self-compensation mechanism.[35] Additionally, Li et al. suggested that doping with $Gd^{3+}$ ions significantly improves the electrical properties of BTO, due to the charge compensation mechanism.[267]

More recently, Arshad et al. synthesized a series of $BaTi_{1-x}Gd_xO_3$ ($0 \le x \le 0.06$) nanostructures by sol-gel auto-combustion method.[268] As shown in **Figure 13**a,b, the most intense XRD peak gradually shifts to lower Bragg angles with increasing Gd-doping. This shift is explained by the difference in ionic radii: $Ti^{4+}$ in octahedral coordination has an ionic radius of 0.605 Å, whereas $Gd^{3+}$ in the same environment has a larger radius of 0.938 Å.[43] The unit cell metrics and structural parameters obtained from the Rietveld analysis of $BaTi_{1-x}Gd_xO_3$ ($0 \le x \le 0.06$) confirmed the presence of a tetragonal phase within the s.g. *P4mm* (see **Table 5** and Figure 13c–f). The slight increase in the volume of the unit cell is due to the substitution of elements with smaller ionic radius by elements with larger radius, such as $Gd^{3+}$, during doping. In addition, the tetragonal distortion ratio decreases slightly with increasing Gd content, resulting in less deformation of the octahedral geometry of $TiO_6$. XPS studies showed that more defects are present in the Gd-doped samples, likely due to the formation of O vacancies associated with the accumulation of $Gd^{3+}$ ions at the $Ti^{4+}$-site. The XPS analysis also identified a mixed valence state of $Ti^{3+}/Ti^{4+}$ in Gd-doped BTO. As far as the morphology concerns, the SEM measurements showed that the Gd-doped BTO ceramics have larger grains than the undoped ones. This indicates that the $Gd^{3+}$ ions promote the growth of the grains due to more defects in the doped nanostructures. The increase in grain size confirms the increase in O vacancies, which is also evident from the XPS studies. The authors suggest that it is also possible that there are a large number of pores between the grains through which various gasses can diffuse and the successive reaction takes place.

As already mentioned, simulation methods offer an interesting tool for analyzing local strain effects in Ln-doped BTO materials. These effects are often difficult to study experimentally due to the low dopant concentration and localized atomic displacements. For example, as mentioned above, Ben and Sinclair have shown that local strains are responsible for the unusual behavior of $T_c$ in Ln-doped BTO, where $T_c$ decreases more with larger La cations than with smaller Gd cations.[82] Recently, Ben et al. have investigated the relationship between the electrical properties of Gd-doped BTO ceramics and doping mechanisms using phase diagram studies and atomistic simulations.[269] Using $Gd_2O_3$, a representative Ln ion of medium size, they identified five key doping mechanisms (**Figure 14**): A-site doping (donor): ionic compensation through the creation of i) B-site or ii) A-site vacancies, leading to electrically insulating RT ceramics due to the immobile vacancies, or iii) electronic compensation through

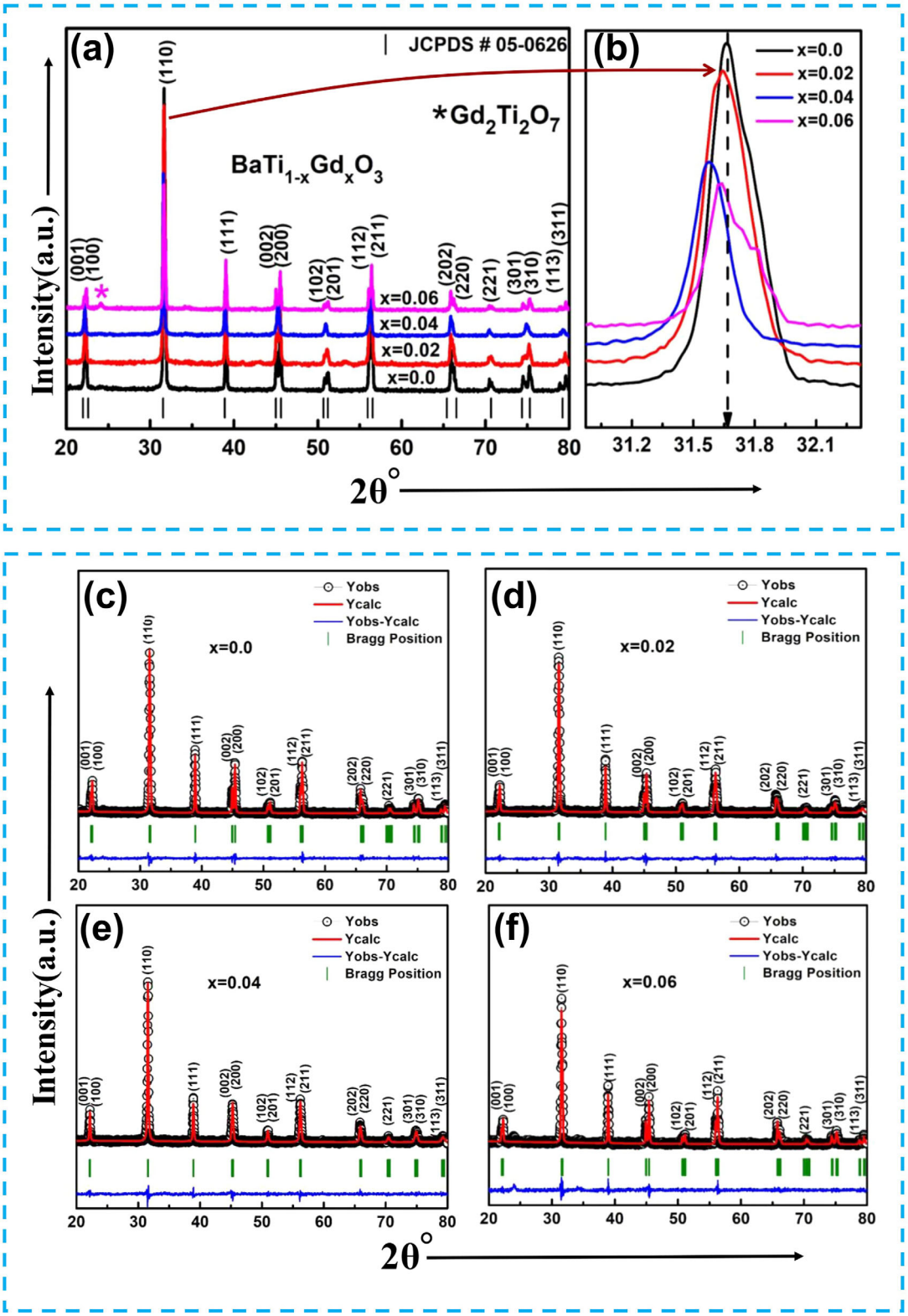


**Figure 13.** a) Cascade XRD patterns of $BaTi_{1-x}Gd_xO_3$ ($0 \le x \le 0.06$), b) enlarged view of reflection (110), c–f) Rietveld refined XRD patterns of $BaTi_{1-x}Gd_xO_3$ ($0 \le x \le 0.06$). Modified with permission.[268] Copyright 2024, Elsevier.

(a)

| doping site | compensation mechanism | | chemical formula |
|---|---|---|---|
| A-site | ionic | i | $2Gd_2O_3 + 4Ba^x_{Ba} + Ti^x_{Ti} \rightarrow 4Gd^{\bullet}_{Ba} + V''_{Ti} + 4BaO + TiO_2 + Ba_{1-x}Gd_xTi_{1-x/4}O_3$ |
| | ionic | ii | $Gd_2O_3 + 3Ba^x_{Ba} \rightarrow 2Gd^{\bullet}_{Ba} + V''_{Ba} + 3BaO + Ba_{1-3a/2}Gd_aTiO_3$ |
| | electronic | iii | $Gd_2O_3 + 2Ba^x_{Ba} \rightarrow 2Gd^{\bullet}_{Ba} + 2e' + 2BaO + 1/2O_2 + Ba_{1-b}Gd_bTiO_3$ |
| B-site | ionic | iv | $Gd_2O_3 + 2Ti^x_{Ti} + O^x_O \rightarrow 2Gd'_{Ti} + V^{\bullet\bullet}_O + 2TiO_2 + BaTi_{1-x}Gd_xO_{3-x/}$ |
| AB-site | self | v | $Gd_2O_3 + Ba^x_{Ba} + Ti^x_{Ti} \rightarrow Gd^{\bullet}_{Ba} + Gd'_{Ti} + BaO + TiO_2 + Ba_{1-y/2}Ti_{1-y/2}Gd_yO_3$ |

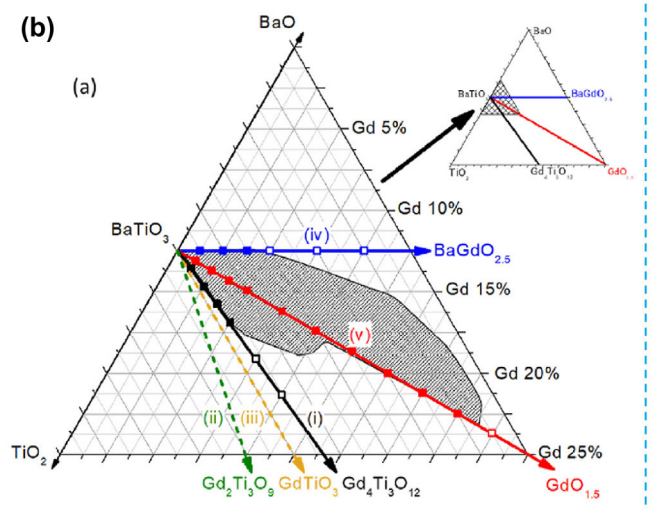


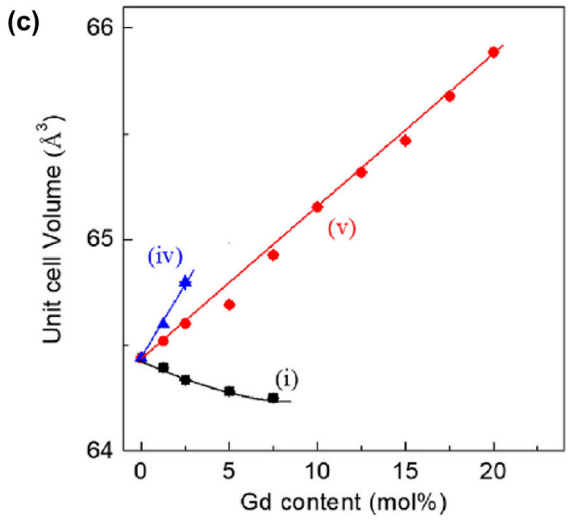


**Figure 14.** a) Possible pathways of charge compensation of Gd-doped BTO, (b) BaO–$TiO_2$-$GdO_{3/2}$ diagram showing single phase samples (filled symbols) and phase mixtures (open symbols) for samples prepared in air by mechanism (i) at 1450 °C and mechanisms (iv) and (v) at 1550 °C as detailed in (a), c) variation of cell volume versus Gd content for single-phase samples according to mechanisms (i), (iv), and (v) and c) schematics of unit cells of undoped BTO mechanisms (i), (iv), and (v). Modified with permission.[269] Copyright 2022, Elsevier.

the creation of conduction electrons, leading to n-type semiconducting ceramics at RT; B-site doping (acceptor) where O vacancies are introduced, leading to insulating p-type ceramics at RT based on the impurity-acceptor doping model (mechanism (iv)); self-compensation (A- and B-site co-doping), where ionic or electronic defects are compensated without introducing new defects, minimally affecting the conduction properties (mechanism (v)). Ben et al. have demonstrated the mechanisms ((i)–(v)) by preparing dense ceramic samples under different conditions: 1450 °C for A-site doping or 1550 °C for AB- and B-site doping. These results highlight the interplay of doping mechanisms in tailoring the electrical properties of Ln-doped BTO ceramics.

To draw a comparison, commercial BTO-based Ln-doped MLCCs have a heterogeneous microstructure. These are based on inner BTO grain cores and outer grain shells containing dopants (including Ln elements) to improve the temperature coefficient of capacitance. These microstructures are a feature of acceptor- and donor-codoped BTOs, especially at modest doping levels (≈1–10 mol%) due to the limited diffusion of the dopants. These results clearly demonstrate the influence of processing conditions on the electrical properties of Gd-doped BTO samples. The n-type semiconductor activity in the bulk $Ba_{1-x}Gd_xTi_{1-x/4}O_3$ ceramic processed in air is due to a small loss of oxygen during sintering at elevated temperature, as described in the literature for La-doped ceramics.[35,133] During cooling, the oxygen can diffuse across the grain boundaries into the ceramic, causing the grain boundaries to oxidize and become electrically insulating. The loss of oxygen can be suppressed by immersing the samples in flowing $O_2$. After being sintered at 1350 °C and cooled to RT in $O_2$, the samples displayed an insulating bulk reaction and no n-type semiconducting areas. These samples are electrically insulating, but their electrical microstructure exhibits significant variability, which is most likely owing to oxygen concentration gradients caused by incomplete oxidation.

Freeman et al. conducted simulations showing that Ln cations produce identical relaxations that deform the surrounding $TiO_6$

**Table 6.** Ionic radii of metal ions in CN=6 and C=12 and different oxidation states according to Shannon.[43]

| Ions | Coordination number (CN) | *r* [Å] |
|---|---|---|
| $Ba^{2+}$ | 12 | 1.61 |
| $Ti^{4+}$ | 6 | 0.605 |
| $Tb^{3+}$ | 12 | 1.203 |
| $Tb^{3+}$ | 6 | 0.923 |
| $Tb^{4+}$ | 6 | 0.76 |

octahedra in a manner similar to the tetragonal phase, but without the required dipole alignment.[88] This relaxation disrupts the tetragonal phase and lowers the transformation temperature to the cubic phase. These relaxations are more pronounced for the larger $La^{3+}$ cation, which remains more central in the dodecahedral A-site compared to the smaller $Gd^{3+}$ cation. As a result, $T_c$ drops faster with La-doping than with Gd.

Although Gd has many applications, Gd-doped BTO has unique properties in this context. Due to its high transmission coefficient in the visible solar spectrum, low band gap and chemical inertness, Gd is an excellent dopant for solar cell applications.[270,271] Moreover, the physicochemical properties of biomaterials play a crucial role in regulating the proliferation and differentiation of osteoblasts. Inspired by the electrical properties of natural bone, recent research has focused on electroactive composite materials, including functionalized Gd-doped BTO, for osteogenesis.[272] The dual-site substitution of Gd at the $Ba^{2+}$- and $Ti^{4+}$-sites of the BTO lattice highlights its potential for bone regeneration. These results show how promising Gd-doped functionalized BTO materials are for bone tissue engineering and strengthen their applications in regenerative medicine. These results show how promising Gd-doped functionalized BTO materials are for bone tissue engineering and their applications in regenerative medicine.

### 2.8. The Case of Tb-Doped BTO

Terbium, Tb, which lies between Gd and Dy in the periodic table, is a unique Ln element. It can exist as $Tb^{3+}$, the stable form at RT, or as metastable $Tb^{4+}$, which is characterized by a half-filled 4*f* shell. The significantly smaller ionic radius of $Tb^{4+}$ (0.76 Å, CN = 6) compared to $Tb^{3+}$ (0.923 Å, CN = 6) increases the likelihood of $Tb^{4+}$ occupying the $Ti^{4+}$-site (**Table 6**).[43] However, direct evidence for the presence of $Tb^{4+}$ at the $Ti^{4+}$-site in BTO remains elusive.[273] Several studies have suggested that Tb ions are incorporated as $Tb^{3+}$ at $Ti^{4+}$-sites in Ba-rich BTO.[65,78,80,274] Tsur et al. proposed that $Tb^{4+}$ could also occupy $Ti^{4+}$-sites in Ba-rich compositions. Due to its smaller ionic radius compared to Pr, Tb is more likely to be substituted at the B-site than Pr.[39] However, the lattice expansion observed in Ba-rich, Tb-doped BTO is less pronounced than in Ba-rich, Pr-doped BTO, reflecting differences in the incorporation and site preference of the two dopants. D. Y. Lu reported 5% Tb-doped BTO synthesized with different Ba/Ti ratios using the mixed oxide route.[273] The study showed that Tb ions exhibit a self-regulating amphoteric behavior, with mixed valence states of Ba-site $Tb^{3+}$ and Ti-site $Tb^{4+}$ contributing to the electroneutrality of the lattice. XRD analysis provided evidence for the occupation of $Ti^{4+}$-sites by Tb ions, while an EPR signal at $g \approx 6.5$ confirmed the presence of $Tb^{4+}$ at these sites.

The intensity of this signal increased with a higher Ba/Ti ratio, suggesting a higher concentration of $Tb^{4+}$ ions at the $Ti^{4+}$-sites. The Raman shift at 805–833 $cm^{-1}$ and an EPR signal at $g$ = 2.004–2.007 associated with ionized Ti vacancies demonstrate the presence of $Tb^{3+}$ at $Ba^{2+}$-sites. This double-sided occupancy emphasizes the amphoteric nature of $Tb^{3+}$ and $Tb^{4+}$. It was also found that grain size increases with increasing $x$, suggesting that Tb ions are not effective grain inhibitors. This trend, showing that Tb-doping cannot refine grains and suppress grain growth, was later confirmed by D. Y. Lu and Y. Y. Peng when they investigated $(Ba_{1-x}Tb_x)(Ti_{1-x}Tb_x)O_3$ ($x$ = 0.05, 0.10, 0.11, 0.12, 0.15, 0.20) prepared by a solid-state reaction.[275]

Recently, Cernea et al. investigated hydrothermally prepared $Ba_{1-x}Tb_xTiO_3$ ceramics ($x$ = 0.00, 0.01, 0.05).[276] As shown in **Figure 15a,b**, the sintered $Ba_{1-x}Tb_xTiO_3$ ceramics exhibited a coexistence of tetragonal and cubic BTO phases after sintering at 1325 °C for 3 h in air. The phase ratio of tetragonal (T) to cubic (C) phases, varied with the Tb-doping level (**Table 7**).

Cernea et al. observed that with increasing doping level up to 1 at% Tb, the lattice parameter $a$ decreased, while the parameter $c$ increased, indicating a successful incorporation of Tb into the BTO host lattice.[276] However, at 5 at% Tb, $a$ decreased further, and $c$ increased to values close to those of undoped BTO. The tetragonality of the synthesized ceramics reached its maximum at 1 at% Tb, but showed a lower value than that of undoped BTO at 5 at%. Although Carnea et al. did not address the specific doping mechanisms of Tb in doped BTO, most studies indicate that Tb-doping enhances the dielectric properties and PL of the BTO host. These improvements emphasize its potential for electronic applications. Cernea et al. also found that Tb-doping considerably affects the microstructure of BTO. The average grain sizes of $Ba_{1-x}Tb_xTiO_3$ powders were determined to be 160 nm ($x$ = 0.00), 135 nm ($x$ = 0.01), and 117 nm ($x$ = 0.05) – the decrease in average grain size with doping is a well-known feature of BTO ceramics, as previously described in the text, where both crystal and particle size decrease with increasing doping concentration. The difference between $Tb^{3+}$ dopants and $Ba^{2+}$ ions distorts the lattice, resulting in a lower crystallite size. Additionally, a number of previous studies have shown that the donor dopant preserves grain boundary mobility while suppressing grain growth. Furthermore, the electrical properties of Tb-doped BTO may be studied in terms of tetragonality, grain size, domain structure, sintered ceramic density, and Tb donor dopant-mediated charge compensation processes. The following conclusions can be drawn from the morphological and structural characterization of hydrothermally prepared $Ba_{1-x}Tb_xTiO_3$ ceramics: *i*) the tetragonality of $Ba_{1-x}Tb_xTiO_3$ reaches its maximum value at $x$ = 0.01; *ii*) the average size of the grains decreases with increasing Tb content; *iii*) the width of the ferroelectric domains decreases with increasing Tb content; and *iv*) the density of the ceramic is strongly dependent on Tb content.

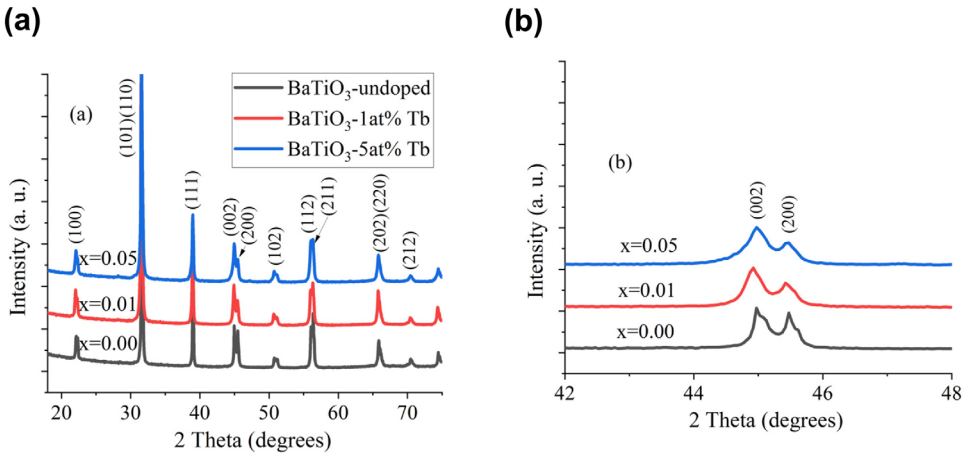


**Figure 15.** a) Cascade XRD patterns of $Ba_{1-x}Tb_xTiO_3$ ($x$ = 0.00, 0.01, 0.05) calcined at 1325 °C, for 3 h in air along with b) a zoomed-in view of the reflections (002) and (200). Modified with permission.[276] Copyright 2021, Elsevier.

### 2.9. The Case of Dy-Doped BTO

The incorporation of dysprosium, Dy, into BTO host has recently been intensively investigated for its potential in MLCCs.[277–280] However, there are relatively few studies in the literature that address the specific doping mechanisms of Dy when incorporated into the BTO lattice. Given the ionic radii of $Dy^{3+}$ (0.912 Å, CN = 6 and 1.083Å, CN = 9) compared to those of the BTO lattice atoms, it is assumed that $Dy^{3+}$ exhibits amphoteric character.[43] Culver et al. synthesized Dy-doped BTO with 0.4, 0.6, and 1.2 mol% Dy and attributed the increased permittivity of the materials to local disorder caused by aliovalent substitution.[281] Morrison et al. suggested that $Dy^{3+}$ could replace either the A-site, the B-site, or both sites in the BTO lattice.[282] Similarly, Rabuffetti et al. studied $Eu^{3+}$-doped BTO and reported that $Eu^{3+}$ preferentially substituted the A-site at concentrations of ≤ 1 mol%, with a transition to both A- and B-site substitution at concentrations of >2 mol%.[84] Given the comparable ionic radii of $Eu^{3+}$ and $Dy^{3+}$, these results suggest that $Dy^{3+}$ preferentially occupies the A-site at low doping levels, as observed by Culver et al. Conversely, Li et al. demonstrated the amphoteric nature of $Dy^{3+}$ in $Ba(Ti_{0.98}Dy_{0.02})O_3$ prepared by powder sintering, with $Dy^{3+}$ partially replacing $Ti^{4+}$ at the B-site and $Ba^{2+}$ at the A-site.[274] Overall, the Dy ions incorporated into the BTO host are generally recognized for their amphoteric behavior, attributed to their intermediate ionic radii among RE elements and their ability to choose either the A- or B-site during sintering depending on the Ba/Ti ratio.[39,40,283] Makovec et al. reported that the solubility of Dy at the Ba-site in Ti-rich BTO, when sintering in air is less than $x$ = 0.0155, resulting in Ti-vacant perovskite phases, such as $Ba_{0.986}Dy_{0.014}Ti_{0.9965}(V_{Ti})_{0.0035}O_3$, at 1400 °C.[93] At 1500 °C, the solubility of $Dy^{3+}$ increases at $Ti^{4+}$-sites in Ba-rich BTO, resulting in O vacant perovskite phases, such as $BaTi_{0.85}Dy_{0.15}O_{2.925}(V_O)_{0.075}$. Despite the progress, the dielectric properties and solubility of Dy in BTO under a self-compensation mechanism have not been sufficiently explored. Lu and Cui investigated Dy-doped BTO ceramics synthesized by a mixed oxide method at 1400 °C (**Figure 16**a,b).[284] They observed that the solubility of Dy in the self-compensation mode reached $x$ = 0.07 for $(Ba_{1-x}Dy_x)(Ti_{1-x}Dy_x)O_3$ and formed a single-phase tetragonal perovskite structure.

In terms of morphology, the grains had a bimodal grain size distribution at $x$ = 0.05, with big grains strewn between the small ones. Surprising grain growth was seen in the sample with $x$ = 0.03, which had an average grain size of 10 µm. As $x$ increased to 0.07, the grains gradually became smaller and more uniform. The microstructure of the fine grains was reached at 0.8 µm. With $x$ = 0.01, the grains of $(Ba_{1-x}Dy_x)Ti_{1-x/4}O_3$ had a bimodal grain size distribution and a grain size value that was the same as that of $(Ba_{1-x}Dy_x)(Ti_{1-x}Dy_x)O_3$. For the ceramic with $x$ = 0.015, tabular-shaped grains were found inside smooth, round grains on both the surface and inside the bulk of the material. Although it is not clear why the rectangular grains appear, there could be a small change in the amount of Dy that causes the grains to have

**Table 7.** Rietveld refinement results for $Ba_{1-x}Tb_xTiO_3$ ceramics calcined at 1325 °C, 3 h in air.[276]

| $x$ | 0.00 | | 0.01 | | 0.05 | |
|---|---|---|---|---|---|---|
| Phase | T-BTO | C-BTO | T-BTO | C-BTO | T-BTO | C-BTO |
| Phase content [wt%] | 94.50 | 5.50 | 94.70 | 5.30 | 93.70 | 6.30 |
| $a$ [Å] | 3.99570 | 4.01261 | 3.99148 | 4.03063 | 3.99151 | 4.02663 |
| $b$ [Å] | 3.99570 | 4.01261 | 3.99148 | 4.03063 | 3.99151 | 4.02663 |
| $c$ [Å] | 4.03296 | 4.01261 | 4.03244 | 4.03063 | 4.03460 | 4.02663 |
| $c/a$ | 1.00932 | 1 | 1.01026 | 1 | 1.01079 | 1 |
| Crystallite size [nm] | 455 | | 402 | | 385 | |

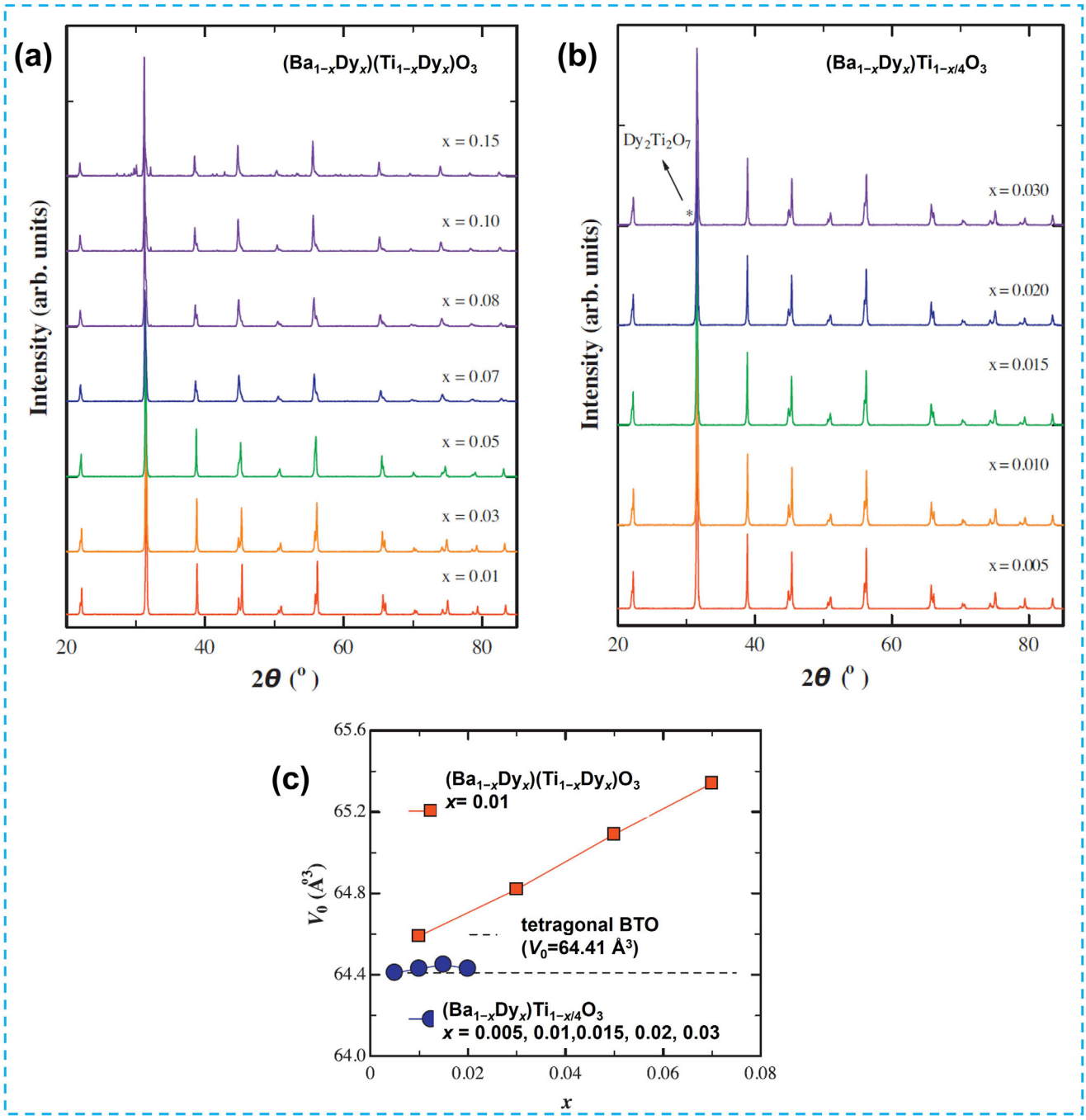


**Figure 16.** Cascade XRD patterns of a) $(Ba_{1-x}Dy_x)(Ti_{1-x}Dy_x)O_3$ ceramics ($x$ = 0.01–0.15), b) $(Ba_{1-x}Dy_x)Ti_{1-x/4}O_3$ ceramics ($x$ = 0.005–0.03), and c) plots of the unit-cell volume ($V_0$) as functions of $x$ for $(Ba_{1-x}Dy_x)(Ti_{1-x}Dy_x)O_3$ and $(Ba_{1-x}Dy_x)Ti_{1-x/4}O_3$. Modified with permission.[284] Copyright 2014, Elsevier.

different shapes, e.g., tabular and round. It is possible that the small difference in Dy content leads to the occurrence of grains with tabular and round morphology. At $x = 0.02$, the grains were uniform, round and smooth. At $x$ values less than or equal to 0.02, the $(Ba_{1-x}Dy_x)Ti_{1-x/4}O_3$ grains became smaller the higher $x$ was. This shows that the addition of more Dy dopant can stop grain growth. At higher Dy concentrations ($x \geq 0.08$), secondary phases occurred, the amount of which increased with increasing $x$. This higher solubility of Dy in the self-compensation mode was much higher ($x = 0.07$) than that in the Ba-vacancy mode ($x = 0.014$).[93] It is noteworthy that no oxygen defects ($V_O$) were observed during sintering at 1400 °C. The formation of $V_O$ is usually accompanied by a hexagonal perovskite structure related to smaller acceptors such as $Mn^{3+}$ (0.58 Å) or $Fe^{3+}$ (0.55 Å) compared to $Ti^{4+}$ (0.605 Å).[285–287] When larger $Dy^{3+}$ ions act as acceptors, sintering at higher temperatures of 1500 °C, leads to the

formation of $V_O$, and thus to a formation of $Ba(Ti_{1-x}Dy_x)O_{3-\delta}$ phase. At lower sintering temperatures (1400 °C) in air, the site preference of $Dy^{3+}$ in BTO is influenced by the Ba/Ti ratio. $Dy^{3+}$ tends to occupy both $Ba^{2+}$- and $Ti^{4+}$-sites simultaneously instead of occupying A-or B-sites. This dual-site substitution forms a self-compensating mechanism described as $Dy^{\bullet}_{Ba} - Dy'_{Ti}$. The Dy-doped BTO ceramics exhibit a single-phase tetragonal perovskite structure with *P*4*mm* symmetry. The relationship between the volume of the unit cell and the Dy concentration follows Vegard's law (Figure 16c). As $x$ increases, the dielectric behavior shifts from a first-order phase transition to a diffuse phase transition, which improves the dielectric temperature stability. A similar self-compensation mode was later confirmed by Sun et al. in BTO samples doped with 4 mol% Dy, further supporting the simultaneous occupation of Ba and Ti-sites as a key structural feature of Dy-doped BTO systems.[288] $Dy^{3+}$ has been shown to have little effect on the morphology of Dy-doped BTO nanopowders; however, excess $Dy^{3+}$ leads to the formation of $Dy(OH)_3$ impurities. Sun et al. reported that pure BTO has microscopic grains, while doped ceramics have grain sizes in the submicrometer range. In general, the grain size of BTO-based ceramics produced from nanopowders is much smaller than that of ceramic grains produced by solid-state processes. The abnormal grain development in pure BTO ceramics, on the other hand, could be due to the abnormally high sintering temperature of the sol-hydrothermally prepared BTO nanoparticles. When $Dy^{3+}$ ions are introduced into the lattice, vacancies are created to keep the charges in equilibrium. The lattice deformation caused by the formation of vacancies therefore requires a certain amount of energy. To conserve energy, $Dy^{3+}$ ions tend to accumulate at or near grain boundaries, which slows movement at grain boundaries and reduces grain growth. Pure BTO has an average grain size of 5 µm, which decreases to 500 nm with 1 mol% $Dy^{3+}$. As already reported by Lu and Cui, the grain size decreases with increasing concentration of $Dy^{3+}$ and the size distribution becomes narrower.[284] In addition, it is known that the diffusion of Dy in the sintering process is controlled by Mg, and an optimized Dy/Mg ratio affects the diffusion of Dy into the grain and the change in microstructure. Chun et al. correlated the energy dispersion spectroscopy results with the SEM images and found that the Dy mapping color increases and the grain size decreases with increasing Dy/Mg ratio because the combination of donor/acceptor inhibits the grain growth of BTO powder during the sintering process.[289]

Ln-based ferroelectric phosphors offer a unique combination of PL emission and ferroelectric functionality, opening up new possibilities for multifunctional ferroelectric and optical materials. However, the mechanism by which a ferroelectric host modulates the local structure (*e.g.*, lattice site, symmetry, stresses) of the Ln activator to tune PL emission has long been unclear. To address this gap, Xia et al., conducted a study on $Dy^{3+}$-doped BTO ceramics prepared by the solid-state method with $Ba_{1-x}Dy_xTiO_3$ ($0 \le x \le 0.07$) compositions.[290] The XRD patterns showed that $Dy^{3+}$ was successfully incorporated into the BTO lattice, while maintaining a tetragonal *P*4*mm* symmetry (**Figure 17**a–c,i,j). Rietveld refinements based on a structural model with $Dy^{3+}$ as a substitute for $Ba^{2+}$ confirmed this incorporation. As the doping level $x$ increased, the refined lattice parameters decreased (Figure 17c), which is consistent with the shift of the 2$\theta$ angle in the XRD patterns. These results are consistent with the observed $B_1$ and $A_1$ peaks in the Raman spectrum, which are characteristic of the tetragonal BTO phase (Figure 17d). It is noteworthy that the substitution of $Ba^{2+}$ by the smaller $Dy^{3+}$ causes stretching of the $TiO_6$ octahedra. Higher $Dy^{3+}$-doping led to a stronger octahedral distortion of $TiO_6$, resulting in a pronounced blue shift of the $A_1$ Raman signal. In addition, the streamline Raman spectra showed that the Raman peaks are uniformly distributed, confirming the phase uniformity of the material (Figure 17e).

Xia et al. have elucidated the interplay between temperature, structure, and PL mechanism in Dy-doped BTO (Figure 17k). With increasing temperature, BTO undergoes a structural phase transition from the tetragonal to the cubic phase. This structural change results from the change in the lattice environment of the dopants. In addition, the cubic phase has a significantly higher symmetry than the tetragonal phase. Consequently, the change in lattice symmetry profoundly alters the PL emission transition of $Dy^{3+}$. These results provide a viable PL-based method for detecting ferroelectric phase transitions and offer a practical tool for exploring the dynamic relationship between PL properties and polarization in ferroelectric materials.

### 2.10. The Case of Ho-Doped BTO

Holmium, Ho, is an important Ln dopant for BTO ceramics due to its pronounced densification effects and its importance for MLCC applications.[291,292] $Ho^{3+}$ shows a more amphoteric behavior (0.901 Å, CN = 6 and 1.12 Å, CN = 10) and occupies both $Ba^{2+}$- and $Ti^{4+}$-sites in the BTO lattice, depending on factors such as the sintering temperature, the environment and the Ba/Ti ratio.[39,40,43,93,291–293] For Ba/Ti = 1, core-shell structured ceramics with X7R stability are usually found at lower sintering temperatures. In such cases, $Ho^{3+}$ is mainly located in the shell phase enveloping the BTO particles instead of being fully incorporated into the BTO lattice.[292]

$Ho^{3+}$ occupation of $Ti^{4+}$-sites leads to the formation of O vacancies under two specific conditions:

i. Low-temperature sintering (1200 °C): in a reducing or weakly oxidizing atmosphere, the resulting temperature-stable ceramics $Ba(Ti_{1-x}Ho_x)O_{3-x/2}$ (Ba/Ti > 1) exhibit a lower dielectric constant and limited $Ho^{3+}$ solubility ($x < 0.03$).[294]
ii. High-temperature and long-term sintering (1400 °C): prolonged sintering in air increases the solubility limit of $Ho^{3+}$ and reaches $x = 0.15$ in $Ba(Ti_{1-x}Ho_x)O_{3-x/2}$. As the $Ho^{3+}$ content increases, the dielectric peak, which corresponds to the transition from the tetragonal to the cubic phase, broadens and shifts to lower temperatures.[93,295]

Xue et al. suggested replacing $Ho^{3+}$ with $Ba^{2+}$ during sintering in air at 1310–1350 °C.[65] Makovec et al. showed that the solubility limit of $Ho^{3+}$ at 1400 °C for $(Ba_{1-x}Ho_x)Ti_{1-x/4}O_3$ with Ti vacancies, is only $x = 0.014$.[93] According to Kishi et al., $Ho^{3+}$ dopants can occupy both $Ba^{2+}$- and $Ti^{4+}$-sites, depending on the Ba/Ti ratio.[291] Due to the amphoteric nature of $Ho^{3+}$, it is difficult to consider the possibility of single site occupancy. Lu et al. investigated the defect chemistry and PL properties of

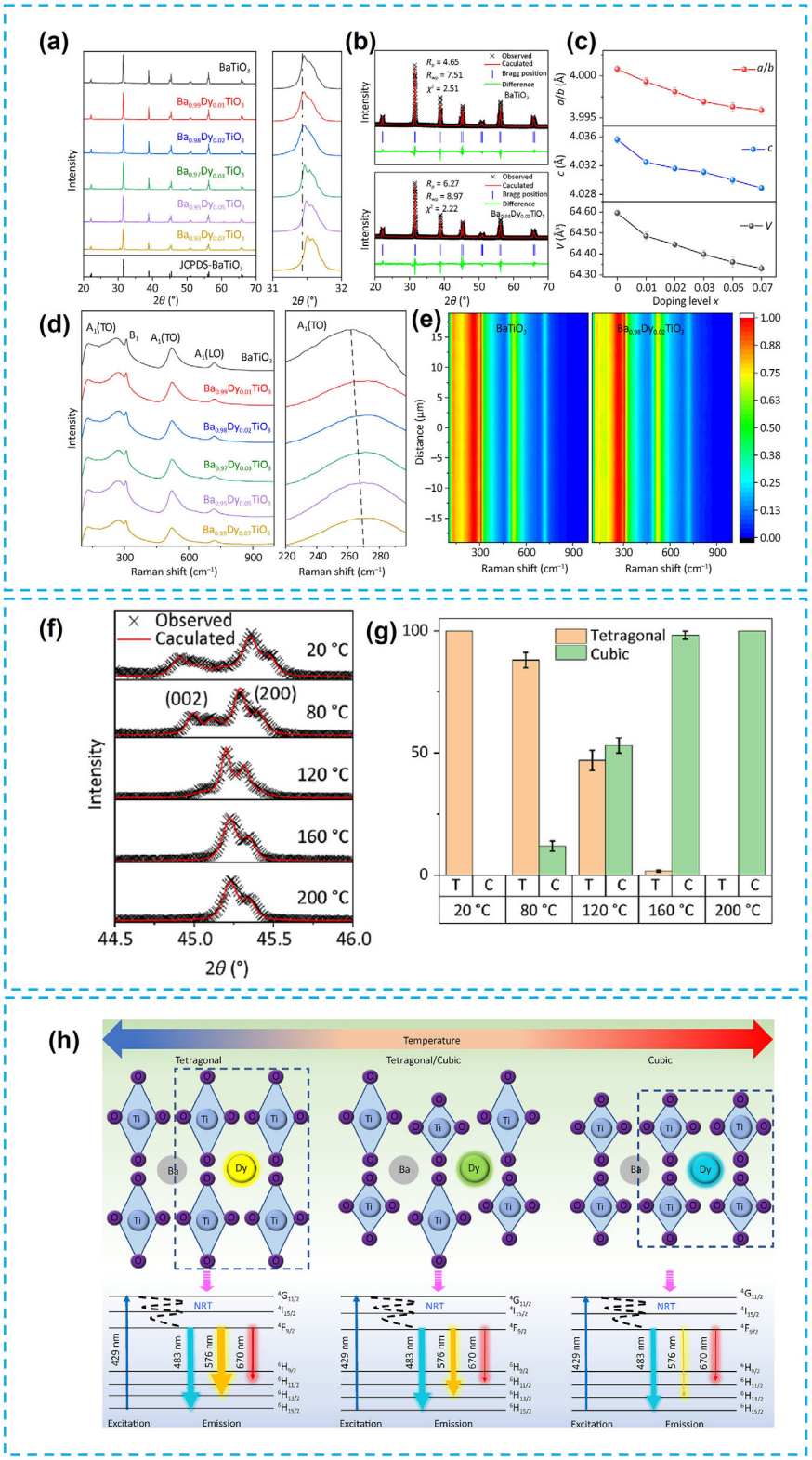


**Figure 17.** a) Cascade XRD patterns of $Dy^{3+}$-doped BTO, b) Rietveld refinements of pure BTO and $Ba_{0.98}Dy_{0.02}TiO_3$, c) unit cell metrics of $Dy^{3+}$-doped BTO, d) Raman spectra of $Dy^{3+}$-doped BTO, e) the 2D mapping images of BTO and $Ba_{0.98}Dy_{0.02}TiO_3$ obtained from the streamline Raman spectra, f) results of Rietveld refinements for variable temperature XRD data of $Ba_{0.98}Dy_{0.02}TiO_3$, g) phase content of $Dy^{3+}$-doped BTO at different temperatures, and h) schematic representation of temperature, structure and PL emission pathways, where NRT denotes a non-radiative transition. Modified with permission.[290] Copyright 2024, Elsevier.

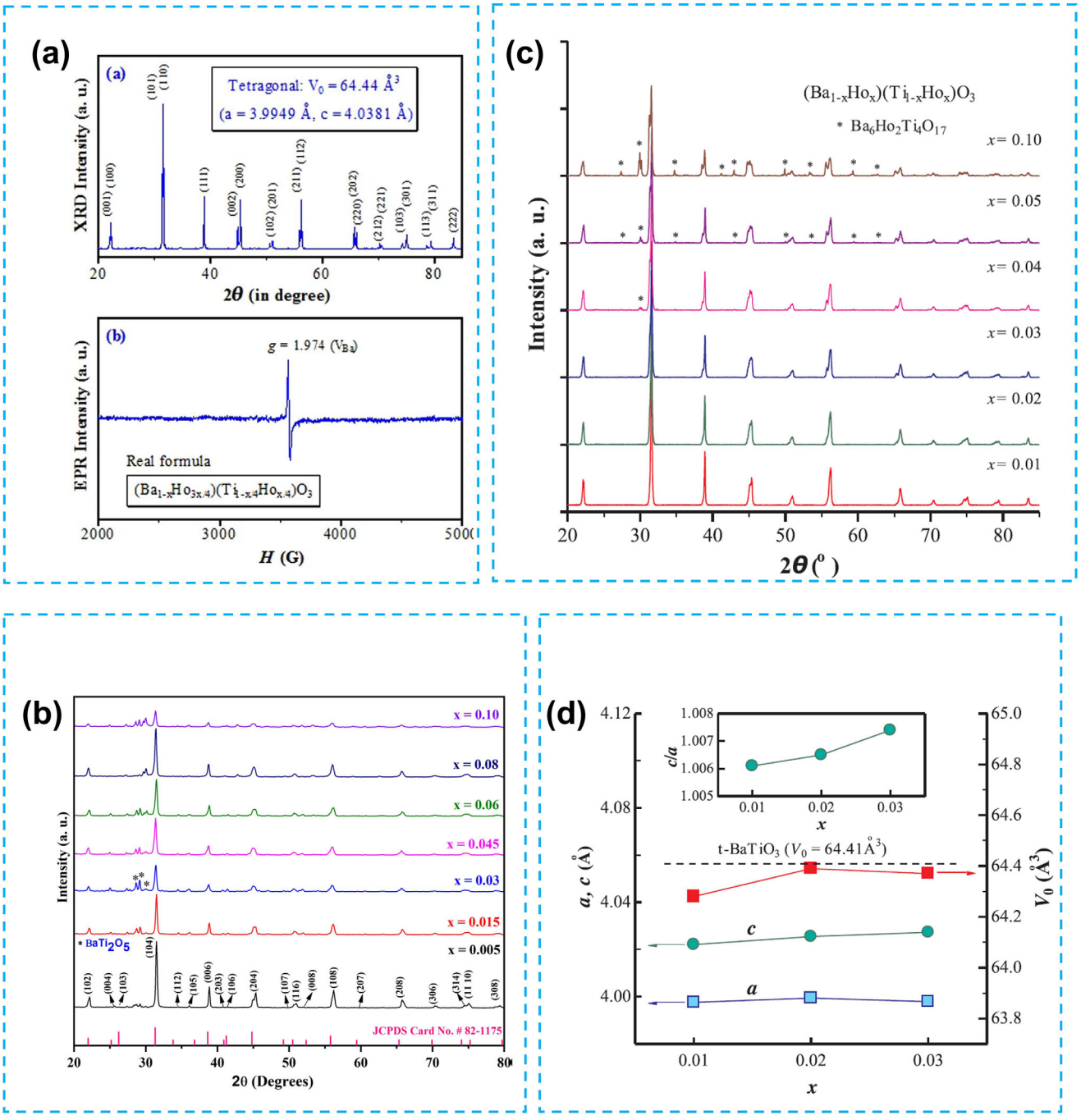


**Figure 18.** a) PXRD pattern (top) along with the EPR spectrum (bottom) of the $(Ba_{1-x}Ho_x)Ti_{1-x/4}O_3$ ($x = 0.01$) ceramic sintered at 1400 °C. Modified from open access articles.[296,298] The actual formula of the ceramic is determined as $(Ba_{1-x}Ho_{3x/4})(Ti_{1-x/4}Ho_{x/4})O_3$ with Ba vacancies ($V_{Ba}$), cascade PXRD patterns of b) $Ba_{1-x}TiO_3$:$xHo^{3+}$ phosphors. Modified with permissions.[297] Copyright 2024, Springer Nature. c) PXRD patterns of $(Ba_{1-x}Ho_x)(Ti_{1-x}Ho_x)O_3$ ($x = 0.01$, 0.02, 0.03, 0.04, 0.05, 0.10). Modified from open access articles.[296,298] and d) variations in unit cell metrics, as a function of $x$ for $(Ba_{1-x}Ho_x)(Ti_{1-x}Ho_x)O_3$ ($x = 0.01$, 0.02, 0.03, 0.04, 0.05, 0.10). The inset shows $c/a$ versus $x$. Modified from open access articles.[296,298]

$Ho^{3+}$-site occupancy in BTO and showed that $Ho^{3+}$ favors the $Ba^{2+}$-site.[296] Their results indicate that the actual formula of $(Ba_{1-x}Ho_x)Ti_{1-x/4}O_3$ ceramic sintered at 1400 °C (with $x = 0.01$) is more accurately represented as $(Ba_{1-x}Ho_{3x/4}(Ti_{1-x/4}Ho_{x/4})O_3$ with Ba vacancies. In particular, the $(Ba_{1-x}Ho_x)Ti_{1-x/4}O_3$ ceramic sintered at 1400 °C exhibited a single-phase tetragonal symmetry, with $Ho^{3+}$ partially occupying the $Ti^{4+}$-sites (**Figure 18a**). The EPR results revealed that the Ti vacancies in Ho-doped BTO are completely filled with $Ho^{3+}$, while the transfer of $Ho^{3+}$ from $Ba^{2+}$- to $Ti^{4+}$-sites causes the appearance of Ba vacancies. The EPR and XRD data provided quantitative insights into the $Ho^{3+}$-site occupancies in $(Ba_{1-x}Ho_x)Ti_{1-x/4}O_3$.

Amphoteric defects in this system include, $Ho^{3+}$ at the $Ba^{2+}$-site ($Ho^{\bullet}_{Ba}$), Ba vacancies ($V''_{Ba}$), and $Ti^{4+}$-site $Ho^{3+}$ ($Ho_{Ti}$), as proposed by Kröger and Vink in 1956.[299] The detailed process of point defect formation is as follows:

*i*) $Ho^{3+}$ dopants simultaneously occupy both $Ba^{2+}$- and $Ti^{4+}$-sites and form self-compensated defect complexes such as $Ho^{\bullet}_{Ba} - Ho'_{Ti}$, $Dy^{\bullet}_{Ba} - Dy'_{Ti}$ and $Er^{\bullet}_{Ba} - Er'_{Ti}$:[284,300]

$$Ho_2O_3 \rightarrow Ho^{\bullet}_{Ba} + Ho'_{Ti} + 3Oo \quad (26)$$

*ii*) The partial occupation of $Ti^{4+}$-sites by $Ho^{3+}$ dopants leads to a Ti-rich lattice environment. This induces Ba vacancies due to the exclusion of additional $Ba^{2+}$-sites $Ho^{3+}$ ($Ho^{\bullet}_{Ba} - Ho'_{Ti}$) in order to fulfill the requirement of electroneutrality of the lattice

$$Ho_2O_3 + 3TiO_2 \rightarrow 2Ho^{\bullet}_{Ba} + V''_{Ba} + 3Ti_{Ti} + 9O_O \quad (27)$$

The defect chemistry of $(Ba_{1-x}Ho_x)Ti_{1-x/4}O_3$ is identical to that of BTO doped with Dy and Er.[284,300] The $(Ba_{1-x}Ho_x)Ti_{1-x/4}O_3$ exhibits a strong EPR signal at $g = 1.974$, confirming the actual formula as $(Ba_{1-x}Ho_{3x/4})(Ti_{1-x/4}Ho_{x/4})O_3$, which involves substitution at two sites and compensation for Ba vacancy. At $x =$ 0.01, 0.75 at.% $Ho^{3+}$ substitutes at $Ba^{2+}$-sites, while 0.25 at.% $Ho^{3+}$substitutes at $Ti^{4+}$-sites. This behavior is similar to that of $(Ba_{1-x}Dy_x)Ti_{1-x/4}O_3$ ($x = 0.01$) reported by Lu and Cui. They attributed the formation of Ba vacancies to the $Dy^{\bullet}_{Ba} - Dy'_{Ti}$ self-compensation mode.[284] Tsur et al. identified $Ho^{3+}$ as the amphoteric Ln dopant in the BTO host lattice.[39]

Dy, which has a similar atomic number to Ho, exhibits a high degree of self-compensation with a higher solubility limit ($x = 0.07$) in $(Ba_{1-x}Dy_x)(Ti_{1-x}Dy_x)O_3$. This contributes to an improved dielectric temperature stability of Y7R and a higher dielectric constant.[299] While Ho and Dy both exhibit stable trivalent states and similar doping behavior on the A-site,[284,296] $Ho^{3+}$ shows a slight preference for $Ba^{2+}$-sites, as shown by Lu et al.[298] Ln dopants occupying double cation sites in BTO tend to lower the $T_C$, as in $Ba(Ti_{1-x}Ho_x)O_{3-x/2}$.[149,296] In this context, Lu et al. reported the solubility limit, abnormal shift regularities of $T_c$, and point defects of Ho-doped BTO, i.e., $(Ba_{1-x}Ho_x)(Ti_{1-x}Ho_x)O_3$ ($x = 0.01, 0.02, 0.03, 0.04, 0.05, 0.10$) ceramics with self-compensation mode. At $x \leq 0.03$, a tetragonal perovskite structure was retained, confirming the complete incorporation of the $Ho^{3+}$ dopants into the BTO lattice. At $x \geq 0.04$, a small amount of secondary phase $Ba_6Ho_2Ti_4O_{17}$ was formed (Figure 18c,d).

The solubility limit of $Ho^{3+}$ in $(Ba_{1-x}Ho_x)(Ti_{1-x}Ho_x)O_3$ was obtained to be $x = 0.03$, which is significantly lower than the values determined for $Dy^{3+}$ ($x = 0.07$) and $Tb^{3+}$ ($x = 0.12$) in BTO in self-compensation mode.[284,275] For $(Ba_{1-x}Ho_x)Ti_{1-x/4}O_3$ with a Ba/Ti ratio < 1, the solubility limit is $x = 0.014$, while for $Ba(Ti_{1-x}Ho_x)O_{3-x/2}$ with Ba/Ti > 1, it is $x < 0.03$.[93,294] However, in $(Ba_{1-x}Ho_x)(Ti_{1-x}Ho_x)O_3$ with a Ba/Ti ratio = 1, a larger number of $Ho^{3+}$ ions can enter the BTO host, but the extent of self-compensation of $Ho^{3+}$ is much weaker than that of $Dy^{3+}$ ($x = 0.07$), and Tb ($x = 0.12$).[275,284] In Ho-doped BTO ceramics with Ba/Ti = 1 and within the solubility limit of $x = 0.03$, $Ho^{3+}$ ions in $(Ba_{1-x}Ho_x)(Ti_{1-x}Ho_x)O_3$ simultaneously replace the $Ba^{2+}$ and $Ti^{4+}$ sites indicating that $Ho^{3+}$ is amphoteric. The solubility limit in $(Ba_{1-x}Ho_x)(Ti_{1-x}Ho_x)O_3$ is about four times higher than that in nominal $(Ba_{1-x}Ho_x)Ti_{1-x/4}O_3$, where Ba/Ti < 1.[296] The XRD and EPR results showed that the solubility limit for $Ba(Ti_{1-x}Ho_x)O_{3-x/2}$ with Ba/Ti > 1 was less than $x = 0.01$, under identical experimental conditions, with no O vacancies observed. This was significantly lower than the solubility of $Ba(Ti_{1-x}Ho_x)O_{3-x/2}$ sintered for several days at 1350–1550 °C.[93,295] Thus, the solubility limit of $Ho^{3+}$ ions in stoichiometric $(Ba_{1-x}Ho_x)(Ti_{1-x}Ho_x)O_3$ with Ba/Ti = 1 ($x = 0.03$) was highest at 1400 °C for 12 h.

The self-compensated $Ho^{\bullet}_{Ba} + Ho'_{Ti}$ complexes dominate the site occupations of $Ho^{3+}$ in $(Ba_{1-x}Ho_x)(Ti_{1-x}Ho_x)O_3$:

$$Ho_2O_3 \rightarrow Ho^{\bullet}_{Ba} + Ho'_{Ti} + O^{x}_{O} \quad (28)$$

for $x \geq 0.02$, the Ba vacancies disappear and only Ti vacancies are present in $(Ba_{1-x}Ho_x)(Ti_{1-x}Ho_x)O_3$. This indicates that the amount of Ba-rich $Ho^{3+}$ is larger than that of Ti-rich $Ho^{3+}$, leading to a Ba-rich case. The additional $Ho^{3+}$ dopants at the $Ba^{2+}$-site, which exclude $Ho^{\bullet}_{Ba} + Ho'_{Ti}$ complexes, lead to Ti vacancies:

$$Ho_2O_3 + 3TiO_2 \rightarrow 2Ho^{\bullet}_{Ba} + V''_{Ba} + 3Ti_{Ti} + 9O_O \quad (29)$$

The point defects in $(Ba_{1-x}Ho_x)(Ti_{1-x}Ho_x)O_3$ for $x \geq$ 0.02 include $Ba^{2+}$-site $Ho^{3+}$ ($Ho^{\bullet}_{Ba}$), $Ti^{4+}$-site $Ho^{3+}$ ($Ho'_{Ti}$), and Ti vacancies ($V''''_{Ti}$). The actual formula is then $(Ba_{1-x}Ho_{x+\delta})(Ti_{1-x}Ho_{x-\delta})O_3$, where $\delta$ is a small value. In self-compensation mode, $Ho^{3+}$ ions favor the substitution of the $Ba^{2+}$-site. By adjusting the Ba/Ti ratio, it is difficult to ensure that uniform doping of Ho at $Ba^{2+}$- and $Ti^{4+}$-sites is achieved. EPR studies showed that two forms of cation vacancies coexist in $(Ba_{1-x}Ho_x)(Ti_{1-x}Ho_x)O_3$ at $x = 0.01$, comparable to Lu-doped BTO.[301]

A similar occurrence was reported for $(Ba_{1-x}Er_x)(Ti_{1-x}Er_x)O_3$ ($x = 0.01$), but the two forms of cation vacancies for $Dy^{3+}$ are absent. This indicates that $Dy^{3+}$ in BTO achieves complete self-compensation without the formation of action vacancies, unlike $Ho^{3+}$ and $Er^{3+}$.[93,284,293] The $V_0$ of $(Ba_{1-x}Er_x)(Ti_{1-x}Er_x)O_3$ was also lower than that of tetragonal BTO. It increased with the increase of $x$ from 0.01 to 0.02 and then decreased slightly at $x =$ 0.03. This fact indicates that it is not easy for $Ho^{3+}$ to incorporate into $Ti^{4+}$-sites, because the size of $Ho^{3+}$ and $Ti^{4+}$ ions do not match.[43] In contrast, the tetragonality of $(Ba_{1-x}Er_x)(Ti_{1-x}Er_x)O_3$ shows an anomalous increase with increasing $x$. This tendency contrasts with the variation of $c/a$ for the self-compensation mode of certain heavy Ln ions, including $(Ba_{1-x}Dy_x)(Ti_{1-x}Dy_x)O_3$ and $(Ba_{1-x}Tb_x)(Ti_{1-x}Tb_x)O_3$.[275]

There are only a few documented perovskite phosphors for green light-emitting diodes (LEDs). Singh et al. synthesized $Ho^{3+}$-doped BTO using the sol-gel method at 1100 °C, demonstrating its potential for solid-state lighting technology.[297] The optimal performance was achieved at a doping concentration of 0.015 mol $Ho^{3+}$ in the range of 0.005-0.10 mol. The XRD analysis confirmed a hexagonal structure of the Ho-doped BTO phase (s.g. $P6_3/mmc$), with shifts in the Bragg reflections indicating an influence of the $Ho^{3+}$-doping concentration (Figure 18b). Singh et al. suggested that the Ho-doping scheme in BTO is characterized by the possible occupation of $Ba^{2+}$ interstitial sites by $Ho^{3+}$, which has an ionic radius of 1.12 Å for CN = 10. This substitution was justified by the similarity of the ionic radii of $Ho^{3+}$ and

$Ba^{2+}$ ions. Nevertheless, the $Ti^{4+}$-sites with an ionic radius of 0.86 Å, remained unsubstituted due to the discrepancy in ionic radii, which explains their exclusion from the substitution process.

Marjanović et al. investigated the effects of $Ho^{3+}$-doping (0.01, 0.1, 0.5, and 1.0 wt% Ho) on the (micro)structure and electrical properties of BTO ceramics prepared by solid-state sintering at 1380 °C and explained the complex interplay between microstructure and properties.[302] The XRD analysis showed that $Ho^{3+}$ was incorporated at the $Ti^{4+}$-sites rather than at the $Ba^{2+}$-sites in the BTO host, while increasing the $Ho^{3+}$-doping level led to the formation of $Ho_2Ti_2O_7$ in the samples doped with 0.5 wt% Ho. The relative density of Ho-doped BTO was between 82% and 91% of the theoretical density. The average grain size of the samples doped with a low doping level (0.01 wt% Ho and 0.1 wt% Ho) was between 20 – 40 μm. With increasing $Ho^{3+}$-doping level, the porosity increased and the density decreased, so that the highest density was achieved for the samples doped with 0.01 wt% (91% of the theoretical density). As a result, the average grain size at 0.5 wt% Ho was between 10 μm and 15 μm, and for the samples doped with 1.0 wt% Ho, the grain size was between 2 μm and 5 μm. Furthermore, increasing the $Ho^{3+}$-doping level leads to the appearance of $Ho^{3+}$-rich regions between the grains. In addition, the effects of $Ho^{3+}$-doping level and microstructure on the dielectric behavior of $Ho^{3+}$-doped BTO were analyzed in detail based on the permittivity-temperature dependence. The highest value of the dielectric constant at RT and the largest change in dielectric constant as a function of temperature was measured for the sample with the lowest $Ho^{3+}$-doping level. At RT, the value of the relative dielectric constant for 0.01 wt % Ho-doped BTO is 2160. For samples with a higher $Ho^{3+}$-doping level, the changes in the dielectric constant as a function of temperature are only weakly pronounced ($\epsilon r_{max}/\epsilon r_{min} \approx 2$). The Curie constant decreases as the degree of $Ho^{3+}$-doping increases, with the sample containing 0.01 wt.% Ho exhibiting the highest values.

From the above, it is evident that the sintering temperature must be adjusted to achieve a balance between phase stability, dielectric performance, and ferroelectric properties of Ho-doped BTO. Choosing the right sintering temperature improves the performance of $Ho^{3+}$-doped BTO by leading to a high dielectric constant, low loss, strong polarization, and low leakage current. From a (micro)structural point of view, lower temperatures can lead to incomplete phase evolution or secondary phases, which can affect performance, while higher temperatures can favor a transition from the tetragonal to the cubic phase and reduce ferroelectricity. At moderate sintering temperatures, the tetragonal phase predominates, increasing spontaneous polarization and improving ferroelectric properties. If sintering is carried out at too high a temperature, a phase transition to cubic BTO occurs, which reduces the remand polarization and the coercive field. In short, there is also a close relationship between sintering temperature, density, and porosity; sintering at low temperatures produces porous structures with poor grain boundaries, whereas sintering at high temperatures results in excessive grain development, which compromises mechanical stability. Furthermore, the dielectric constant is influenced by the phase purity and grain size—higher sintering temperatures generally lead to larger grain sizes, reducing grain boundaries, which can decrease dielectric loss. However, excessive sintering can cause grain coarsening, leading to leakage currents. The dielectric constant in particular is controlled by the phase purity and the particle size. Higher sintering temperatures often result in larger grain sizes, minimizing grain boundaries and potentially reducing dielectric loss. However, excessive sintering can lead to coarsening of the grains, resulting in leakage currents.

### 2.11. The Case of Er-Doped BTO

Among the Ln ions, $Y^{3+}$ and $Dy^{3+}$ are critical dopants in the production of MLCCs with base metal electrodes.[303,304] Since erbium, Er, has a similar ionic radius (0.89 Å, CN = 6 and 1.062 Å, CN = 9) and comparable properties to these ions, its doping behavior is of significant technological interest.[43] $Er^{3+}$ is particularly suitable for optical applications due to its high-intensity green emission bands, which arise from the thermally coupled energy levels $^2H_{11/2}$ and $^4S_{3/2}$. The narrow energy gap between these levels allows population via both up-conversion or down-conversion processes, as extensively discussed in the literature.[305–313] $Er^{3+}$ is a promising phosphor for luminescent devices owing to its strong intra-4*f* transitions in the green and red spectral regions characterized by a long intrinsic lifetime. Its stable 3+ oxidation state enables $Er^{3+}$ to substitute either the A- or the B-site in the perovskite lattice, influenced by ionic radius of 1.004 Å (CN = 8), which lies between that of $Ba^{2+}$ and $Ti^{4+}$.[43,78,299,310,314,315]

In the early 2000s, Buscaglia et al. conducted pioneering research on the incorporation mechanisms and defect chemistry of Er-doped BTO ceramics.[78,315,314] Using the extended X-ray absorption fine structure (EXAFS) method, which is highly sensitive to the local atomic environment, they investigated the site preference of $Er^{3+}$ dopants in the BTO lattice. The EXAFS analysis of the Er–$L_{III}$ edge revealed that in the $BaEr_{0.08}Ti_{0.92}O_{2.96}$ composition, $Er^{3+}$ predominantly substitutes the $Ti^{4+}$-site. In contrast, the composition $Ba_{0.96}Er_{0.08}Ti_{0.96}O_3$ showed nearly equal occupation of $Er^{3+}$ at the $Ba^{2+}$- and $Ti^{4+}$-sites, indicating that stoichiometry plays a crucial role in controlling the doping mechanism. While neither doping process was exclusive in these samples, increased substitution of $Er^{3+}$ at the $Ba^{2+}$-site in $Ba_{0.96}Er_{0.08}Ti_{0.96}O_3$ was accompanied by greater structural disorder. This observation aligns with the amphoteric behavior of $Er^{3+}$ in the BTO lattice, as detailed by Takada et al., Xue et al., Buscaglia et al., and later by Chen et al.[65,315,316,317] Specifically, Takada et al. demonstrated that when the Ba/Ti ratio, *R* is less than 1, $Er^{3+}$ acts as an acceptor, favoring substitution at the Ti-site. Conversely, when $R > 1$, $Er^{3+}$ acts as a donor, favoring substitution at the Ba-site. When $R = 1$, $Er^{3+}$ occupies both cationic sites simultaneously, leading to self-compensation and an electrical conductivity comparable to that of undoped BTO. Further studies by Chen et al. revealed that that Er-doped BTO thin films with A-site substitution have smaller lattice constants, larger grain sizes, and smoother surfaces compared to those with B-site substitution.[317] In addition, A-site doped films showed higher integrated green emission intensity and weaker red emission than the B-site counterparts. However, the quantitative analysis of the effects of Er content remains limited, leaving room for further investigation.

Xue et al. highlighted the critical influence of the Ba/Ti ratio on the electrical properties of BTO doped with trivalent

impurities.[65] In Er-doped BTO, an excess of $TiO_2$ promotes Er substitution at $Ba^{2+}$-sites, resulting in the formation of $Er^{\bullet}_{Ba}$ and donor-like behavior. Conversely, an excess of BaO drives Er dopants to occupy $Ti^{4+}$-sites, leading to the formation of $Er'_{Ti}$ and acceptor-type behavior. The possible modes of incorporation of Er incorporation into the BTO lattice, as proposed by Kröger and Vink, can be summarized as follows:[299]

*i*) $Er^{3+}$ substitution at $Ba^{2+}$-site (Ba/Ti < 1): donor mechanism

$$Er_2O_3+2TiO_2 \rightarrow 2Er^{\bullet}_{Ba}+2Ti_{Ti}+6O_O+1/2O_2+2e' \quad (30)$$

$$Er_2O_3+3TiO_2 \rightarrow 2Er^{\bullet}_{Ba}+3Ti_{Ti}+V''_{Ba}+9O_2 \quad (31)$$

$$2Er_2O_3+3TiO_2 \rightarrow 4Er^{\bullet}_{Ba}+3Ti_{Ti}+V''''_{Ti}+12O_2 \quad (32)$$

$$3Er_2O_3+6TiO_2 \rightarrow 6Er^{\bullet}_{Ba}+6Ti_{Ti}+V''_{Ba}+V''''_{Ti}+21O_2 \quad (33)$$

*ii*) $Er^{3+}$ substitution at $Ti^{4+}$-site (Ba/Ti > 1): acceptor mechanism

$$2BaO + Er_2O_3 \rightarrow 2Ba_{Ba}+2Er'_{Ti}+5O_O+V^{\bullet\bullet}_O \quad (34)$$

*iii*) equal population of $Er^{3+}$ at $Ba^{2+}$- and $Ti^{4+}$-sites (Ba/Ti = 1): self-compensation mechanism

$$Er_2O_3 \rightarrow Er^{\bullet}_{Ba}+Er'_{Ti}+3O_o \quad (35)$$

Buscaglia et al. conducted a comprehensive study on Er-doped BTO ceramics with dopant concentrations of 0.25, 0.5, 1, 2, 8, and 10 at.% sintered at temperatures ranging from 1350 to 1550 °C.[315] The authors investigated the evolution of microstructure, unit cell parameters, and RT resistivity as a function of $Er^{3+}$ dopant concentration and Ba/Ti ratio. These properties were analyzed in the context of the mechanisms of $Er^{3+}$ incorporation. The study involved the preparation of five distinct series of Er-doped BTO samples, each corresponding to one of the following possible incorporation mechanisms:

A. $Ba_{1-x}Er_xTiO_3$, Ba substitution, electron compensation $[Er^{\bullet}_{Ba}] = [e']$
B. $Ba_{1-x}Er_xTi_{1-x/4}O_3$, Ba substitution, Ti vacancy compensation $[Er^{\bullet}_{Ba}] = 4[V'''Ti]$
C. $Ba_{1-3/2x}Er_xTi_xO_3$, Ba substitution, Ba compensation $[Er^{\bullet}_{Ba}] = 2[V''Ba]$
D. $Ba_{1-x/2}Er_xTi_{1-x/2}O_3$, self-compensation $[Er^{\bullet}_{Ba}] = [Er'_{Ti}]$
E. $BaEr_xTi_{1-x}O_{3-x/2}$, Ti substitution, O vacancy compensation $[Er'_{Ti}] = 2[V^{\bullet\bullet}_O]$

In mechanisms A, B, and C, the $R < 1$, with the lowest $R$ value observed in mechanism C. For mechanisms D and E, $R = 1$ and $R > 1$ respectively.

For $Er^{3+}$ concentrations $x \leq 0.01$, the behavior of the dopant is largely independent of $R$. The observed behavior for formulations A, B, D, and E is very similar. However, for mechanism C, which has the lowest $R$ value (0.985 for $x = 0.01$), the trend of $(a^2c)^{1/3}$ was slightly different. These results up to $x = 0.01$ indicate that $Er^{3+}$ ions are incorporated into both cation sites ($Ba^{2+}$ and $Ti^{4+}$) and favor substitution at the Ba-site, as described by the following mechanism:

$$(1-y_1)BaO + (1-y_2)TiO_2+1/2\,(y_1+y_2)\,Er_2O_3 \rightarrow$$
$$Ba_{(1-y_1)}Er_{(y_1+y_2)}Ti^{3+}_{(y_1-y_2)}Ti^{4+}_{(1-y_1)}O_3+1/4\,(y_1-y_2)\,O_2 \quad (36)$$

Here, $y_1$ represents the proportion of $Er^{3+}$ occupying the Ba-site, $y_2$ the proportion occupying the Ti-site, and $x = y_1 + y_2$, where $y_1 > y_2$. The substitution of $Er^{3+}$ at the Ba-sites ($y_1$–$y_2$) results in a net excess of $Er^{3+}$ dopants at the $Ba^{2+}$-site, which is directly linked to the generation of conduction electrons through the formation of $Ti^{3+}$. This mechanism explains the semiconducting properties of Er-doped ceramics over a wider range of dopant concentrations than is typically observed for donor dopants. An initial decrease in the unit cell parameter can be attributed to the predominant substitution at the $Ba^{2+}$-site ($y_1 >> y_2$). A further decrease in the cell parameter corresponded to continued Ba substitution, while an increase is expected upon self-compensation. At dopant concentrations in the range of $0.01 < x \leq 0.02$, significant changes in behavior were observed for the different incorporation mechanisms. In mechanisms A to D, the pyrochlore phase $Er_2Ti_2O_7$ was formed, while the samples remained slightly semiconducting. In formulations A, B, and C, the grain size increased, but formulation E resulted in phase-pure, insulating ceramics with significantly reduced tetragonality compared to the other formulations. The observed behavior for mechanisms A to C ($R < 1$) likely correlates with reaching the maximum solubility of $Er^{3+}$ on the $Ba^{2+}$-site when the total dopant content is between 0.01 and 0.02. Beyond this range, the additional $Er^{3+}$ increasingly occupied $Ti^{4+}$-sites, leading to a state where $y_2 \approx y_1$. Excessive doping beyond this threshold results in the formation of secondary phases, such as the pyrochlore phase and $Ba_6Ti_{17}O_{40}$.

The slightly semiconducting character of the samples with $x = 0.02$ indicates a slight excess of $Er^{3+}$ on the $Ba^{2+}$-site. At $x = 0.08$, the samples transitioned to an insulating state, corresponding to an even distribution of $Er^{3+}$ dopants on both sublattices. This behavior aligns with a self-compensation mechanism described by the following equation:

$$M_2O_3 \rightarrow M^{\bullet}_{Ba} + M'_{Ti}+3O_o \quad (37)$$

Alternatively, the compensation of the net excess of $Er^{3+}$ on the Ba-site can be attributed to the formation of cation vacancies, as expressed by the following relations:

$$M_2O_3+3TiO_2 \rightarrow 2M^{\bullet}_{Ba} + V''_{Ba}+3Ti_{Ti}+9O_O \quad (38)$$

$$2M_2O_3+3TiO_2 \rightarrow 4M^{\bullet}_{Ba} + V''''_{Ti}+3Ti_{Ti}+12O_O \quad (39)$$

For mechanism E ($R > 1$), a predominant substitution of $Er^{3+}$ at the Ti-site was expected for $x \geq 0.02$, although a minor substitution at the Ba-site cannot be excluded. The incorporation of $Er^{3+}$ in this mechanism can be described as follows:

$$(1-y_1)BaO + (1-y_2)TiO_2+1/2\,(y_1+y_2)\,Er_2O_3 \rightarrow$$
$$Ba_{(1-y_1)}Er_{(y_1+y_2)}Ti_{(1-y_2)}D_{((y_2-y_1)/2)}O_{3-((y_2-y_1)/2)} \quad (40)$$

where $y_2 >> y_1$. To compensate for the excess negative charge of $Er^{3+}$, O vacancies are formed (Δ), as shown in the following reaction:

$$M_2O_3 + 2BaO \rightarrow 2M'_{Ti} + V_O^{\cdot\cdot} + 2Ba_{Ba} + 5O_O \quad (41)$$

At high dopant concentrations ($x = 0.08, 0.1$), $Er^{3+}$ is incorporated at the $Ti^{4+}$-site by the formation of $Ba_{12}Er_{4.67}Ti_8O_{35}$, while in mechanism E there is an excess of BaO and BTO. When the temperature exceeds 1400 °C, $Er^{3+}$ is preferentially incorporated into the B-site of the BTO host. Samples with $R > 1$ were single-phase and insulating at doping concentrations of ≥ 2 at.%. In these cases, the incorporation of $Er^{3+}$ occurred predominantly at the Ti-site, compensating for O vacancies. This incorporation reduces the tetragonality (transitioning to a cubic structure at doping concentrations of ≥ 8 at.%), expands the unit cell, and reduces the particle size (~1 μm). The solubility of $Er^{3+}$ at the $Ti^{4+}$-site was at least 10%, comparable to that of $Y^{3+}$ (≈ 12%) and $Dy^{3+}$ (≈ 9 at.%).[303] It was also found that BTO ceramics doped with $Er^{3+}$ at the $Ti^{4+}$-site contain a significant concentration of O vacancies. At $R = 1$, complete incorporation of $Er^{3+}$ into the perovskite lattice was not achieved, even for heavily doped samples, leading to the presence of a minor pyrochlore phase. This behavior was attributed to the preferential incorporation of $Er^{3+}$ at the $Ti^{4+}$-site once the maximum solubility of $Er^{3+}$ at the $Ba^{2+}$-site was reached. Buscaglia et al. concluded that sintering conditions play an important role in determining the properties of Ln-doped BTO. Low dopant concentrations in combination with short-term sintering at lower temperatures (1400 °C) improved the integration of the dopants at the Ba-sites. However, to achieve a uniform distribution of $Er^{3+}$ at the $Ti^{4+}$-sites in heavily doped samples, higher temperatures (above 1400 °C) and longer sintering times (up to 100 h) are required. Deviations of the Ba/Ti ratio from the nominal value and impurities in the raw materials also influence the incorporation of the dopant at low concentrations. Previous studies have provided additional insight into the incorporation of Er in BTO. Hwang et al. investigated the defect chemistry associated with Er-doping in the BTO lattice.[68]Their work demonstrated that the replacing Ti with $Er^{3+}$ in $Ba(Ti_{1-x}Er_x)O_{3-0.5x}$ resulted in significant shift in the conductivity minimum and altered acceptor-donor behavior. The authors found that the solubility of $Er^{3+}$ ions at the $Ti^{4+}$-site was less than 3 mol%, while its poor solubility at the $Ba^{2+}$-site (< 1.0 mol%) prevented donor-doped behavior in $(Ba_{1-x}Er_x)O_{3-0.5x}$, which typically compensates electrons for cation vacancies above 0.5 mol% donor concentration. In stoichiometric BTO with up to 2.0 mol% Er, the dopant simultaneously occupied both Ba and $Ti^{4+}$-sites, leading to donor-acceptor equilibrium. However, at concentrations higher than 3 mol%, the conductivity curve shifted similarly to that of $Ba(Ti_{1-x}Er_x)O_{3-0.5x}$, but to a lesser extent. This acceptor-donor behavior, coupled with low-oxygen non-stoichiometry in samples doped with Er concentrations above 3.0 mol% was attributed to the different solubility of $Er^{3+}$ at $Ba^{2+}$- and $Ti^{4+}$-sites within the BTO lattice. Lu et al. advanced the understanding of the defect chemistry of Er-doped BTO by detecting strongly enhanced and anomalous Raman signals in nominal $(Ba_{1-x}Er_x)Ti_{1-x/4}O_3$ ($x = 0.01$) ceramics. These observations were closely related to the site occupancies of $Er^{3+}$.[300] The defect chemistry of Er-doped BTO was found to be very similar to that of Dy-doped BTO, as mentioned earlier. In particular, BTO doped with $Er^{3+}$ at $Ti^{4+}$-sites showed predominantly typical Raman phonon modes characteristic of tetragonal symmetry. A significant increase in the intensity of the Raman bands showed a hundredfold selectivity for $Ba^{2+}$-site $Er^{3+}$ dopants over $Ti^{4+}$-site $Er^{3+}$ dopants. Additionally, an intense EPR signal at $g = 1.974$ was associated with ionized Ba vacancy defects. Based on these results, the defect chemistry suggests that the formula for Er-doped BTO could be represented as $(Ba_{1-x}Er_{3x/4})(Ti_{1-x/4}Er_{x/4})O_3$. The anomalous Raman signals are attributed to a fluorescence effect associated with the $Er^{3+}$ ions at the $Ba^{2+}$-site. Lu et al. emphasized the importance of their results proposing that Raman spectra could serve as a probe for the detection of Ba-site $Er^{3+}$ occupancy in BTO co-doped with $Er^{3+}$ ions and other dopants.[290]

From a theoretical perspective, Zulueta et al. investigated the defect energies and conductive properties of 1 mol% $Er_2O_3$-doped BTO using lattice statics, molecular dynamics, and experimental measurements of dielectric and electrical properties.[318] The calculation of defect energies for different incorporation modes showed that self-compensation is the preferred mechanism. However, mixed mechanisms, in which dopants simultaneously occupy $Ba^{2+}$- and $Ti^{4+}$-sites, leading to the formation of O vacancies, could also be active under certain conditions. The incorporation of $Er^{3+}$ into the BTO lattice was found to reduce the DC conductivity at high temperatures compared to the undoped BTO. This reduction was attributed to the interaction of the Ln dopants with cation and O vacancies, which effectively trap charge carriers and hinder conductivity. In recent years, Clabel and colleagues have significantly advanced the study of Er-doped BTO thin films using techniques such as SEM, XPS, and XRD, to investigate the role of O vacancies in BTO and Er-doped BTO thin films with grain sizes ranging from 40 to 60 nm.[319–321] XRD profiles and XPS analyses showed that $Er^{3+}$ predominantly replaces the $Ti^{4+}$-sites in the BTO lattice, leading to the formation of the tetragonal phase. Furthermore, doping at low concentrations was shown to reduce the $Ti^{4+}$ ions to $Ti^{3+}$. The emission mechanism in both BTO and Er-doped BTO thin films was proposed to be related to chemical defects such as hydroxyl radicals and excess or unoccupied $O^{2-}$-sites. These defects in turn lead to the recombination of self-trapped excitons within the band gap of Er-doped thin films, providing valuable insights into the luminescence properties of these materials. Among other things, Clabel et al. showed an increase from 8.92 nm for the BTO film to 29.31 nm for the Er-doped BTO film, associated with the enhancement of the grain growth, which is attributed to the increase in the thermal temperature.[320] The author explained this phenomenon as follows: due to the difference in the values of the radius of the ions $Er^{3+}$ (0.100 nm) and $Ti^{4+}$ (0.061 nm) it can be assumed that i) either $Er^{3+}$ could replace some $Ti^{4+}$ sites, leading to distortions in the octahedral coordination environment, or ii) the $Er^{3+}$ ions replacing the $Ti^{4+}$-sites could have a stabilizing effect on the Ti–O bond. Because of the more electropositive character of $Er^{3+}$, a strengthening of the bond between $O^{2-}$ and the less electropositive $Ti^{4+}$ ions would take place. Thus, after substitution with the $Er^{3+}$ dopants, a larger lattice is expected, as well as agglomeration, due to which the largest grain sizes are achieved. Considering that the optimization of electrical properties of both Ho and Er-doped BTO requires a microstructure with high density and homogeneous grains, Mitić et al. investigated the influ-

ence of $Er_2O_3$ and $Ho_2O_3$ on the microstructure of BTO ceramics and the corresponding electrical properties.[322] Namely, the increase of RE cations content inhibits the abnormal grain growth. From the microstructural point of view, it was shown that the grain size decreases with the increase of dopant concentration. Thus, the average grain size at 0.1 wt% Er was between 20 and 30 μm, and for the samples doped with 0.5 wt% Er, the grain size decreased to a value of 10 – 15 μm for Er-doped BTO and 3 – 5 μm for Ho-doped BTO.

### 2.12. The Case of Tm-Doped BTO

Besides Nd, thulium, Tm, is a highly desirable Ln dopant due to its absorption within the frequency range of affordable semiconductor lasers. However, research on $Tm^{3+}$-doped BTO remains limited, with only a few studies primarily focusing on its electrical properties and their correlation with doping.[39,323–326] Interestingly, the majority of studies on Tm-doped BTO were published in the first 15 years of the 2000s (Figure 2). For instance, Jing et al. explored Tm-doped BTO opals, achieving blue upconversion PL and a photonic band gap in BTO opals doped with 3 at.%Tm.[325] As previously mentioned in the text, Tsur et al. classified the behaviors of various Ln element (including Tm) in BTO, addressing the challenges of Ln cation substitution in the BTO lattice. Due to its relatively small ionic radius (0.88 Å, CN = 6, 1.052 Å, CN = 9) $Tm^{3+}$ predominantly occupies the B-site in the BTO host.[39,40,77] Tsur et al. also suggested the possibility of amphoteric behavior and the presence of mixed valence states at RT, with a higher concentration of $Tm^{2+}$ (1.03 Å, CN = 6 and 1.09 Å, CN = 7) expected at lower temperatures.[39] The most recent work on this topic was published over a decade ago by Cernea et al., who investigated the morphology, in which they linked the morphology, structure, and optical properties of 5 at.% Tm-doped BTO powders and ceramics.[276] The powders exhibited a single-phase cubic symmetry, while the sintered ceramics displayed a tetragonal structure. The PL spectra revealed characteristic transitions of $Tm^{3+}$ ions, confirming the successful incorporation of $Tm^{3+}$ ions into the BTO host lattice. In general, doping with Tm reduces the grain size of BTO. This reduction is attributed to the influence of Tm ions on surface, mechanical stresses, and grain boundary effects. As Tm concentration increases, these factors combine to suppress grain growth, resulting in smaller grains.[323]

### 2.13. The Case of Yb-Doped BTO

Similar to the chemistry of Tm-doped BTO systems, there are few limited references for ytterbium, Yb-doped BTO materials. Although $Yb^{3+}$ is relatively small (0.868 Å, CN = 6 and 1.042 Å, CN = 9) and typically occupies the B-site as a trivalent ion, it exhibits a slight degree of amphoteric behavior, with $Yb^{\bullet}_{Ba}$ being more common in Ti-containing systems as noted by Tsur et al.[39] $Yb^{3+}$ is expected to behaves as an acceptor, behavior also observed in Tm-doped BTO materials.

Murillo et al. investigated the structural and morphological properties of BTO co-doped with Er and Yb, while Li et al. emphasized the dielectric properties and tunability of Yb and other Ln-doped BTO materials.[327,328] Dunbar et al. conducted EPR studies on various Ln elements, including Yb-doped BTO.[45] Yao et al. demonstrated that co-doping with Bi and Yb significantly effects the microstructural and dielectric properties of BTO.[329] Tan et al. reported the modulation of upconversion in BTO:$Yb^{3+}$, $Er^{3+}$ inverse opal structures, while Kumari et al. explored the yellow–orange upconversion emission in $Eu^{3+}$–$Yb^{3+}$ co-doped BTO phosphor.[330,331] Although these studies are commendable, in most of the experiments, the $Yb^{3+}$ was co-doped with another foreign ion. Research on Yb, which is individually incorporated into the BTO host, has primarily focused on electrical and optical applications.[332–335]

Ganguly et al. prepared Yb-doped BTO, specifically, $Ba(Ti_{1-x}Yb_{4x/3})O_3$ ($x$ = 0.02, 0.04, 0.06, 0.08, and 0.10), using the solid-state method.[335] Structural studies revealed a transition from tetragonal to cubic symmetry with increasing $Yb^{3+}$ content, which is confirmed by Rietveld refinements (**Figure 19a–c**). The presence of (002) and (200) peaks at $x$ = 0.00–0.04 indicates tetragonal symmetry (s.g., *P*4 *mm*), but for $x \geq 0.06$ the merging of these peaks suggests better indexing with cubic symmetry (s.g., *Pm*-3*m* ). The shift of the peak to lower angles indicates changes in lattice properties with increasing Yb concentration. The tetragonality of the lattice decreases as $Yb^{3+}$ content increases, eventually leading to a cubic symmetry. This was further confirmed by Fourier Transform Infrared (FTIR) spectroscopy measurements, Raman spectroscopy, and temperature-dependent dielectric studies. In addition, FTIR analysis revealed a deformation of the $TiO_6$ octahedra due to Yb substitution. As the $Yb^{3+}$ concentration increased, the intensity of tetragonal Raman modes diminished and new peaks with higher frequencies appeared alongside existing peaks (Figure 19d). The presence of Yb was also found to significantly affect the microstructure—with higher Yb concentrations ($x \geq 0.06$) leading to a notable reduction in grain size. To be more specific, the microstructural properties are primarily influenced by the transfer of materials during the heating process. The solid-state synthesis begins with the milling of raw materials, which leads to a reduction in the average particle size. During heat treatment, diffusion sets in at the contact points of the particles, leading to grain formation during sintering. The transport of materials over long distances leads to the development of larger grains. The grain size in the Yb-doped BTO decreases as the Yb content increases. The diffusion of $Yb^{3+}$ ions in the BTO lattice decreases accordingly. The replacement of larger ions at the B-site can lead to a reduction in grain size when the degree of doping increases, as the diffusion of larger ions is slower in the presence of smaller ions. The presence of the secondary phase $Yb_2Ti_2O_7$ can hinder grain development in the heavily doped samples. $Yb^{3+}$-doped BTO exhibits segregation of the secondary Yb-rich phase at the grain boundary, which limits the solubility of Yb in BTO. In short, doping BTO with $Yb^{3+}$ causes a reduction in grain size by inhibiting the movement of grain boundaries and restricting atomic diffusion. The exact effects depend on the $Yb^{3+}$ content and the sintering conditions.

More recently, Alshoaibi et al. used theoretical simulations to investigate the effects of Yb incorporation at the Ti and Ba-sites in BTO, modifying the structural geometry, electronic structure, and dielectric constants.[334] Their comprehensive study revealed that Yb-doping slightly alters the lattice parameters compared to pure BTO, resulting in shorter Ba–O and Ti–O bond lengths.

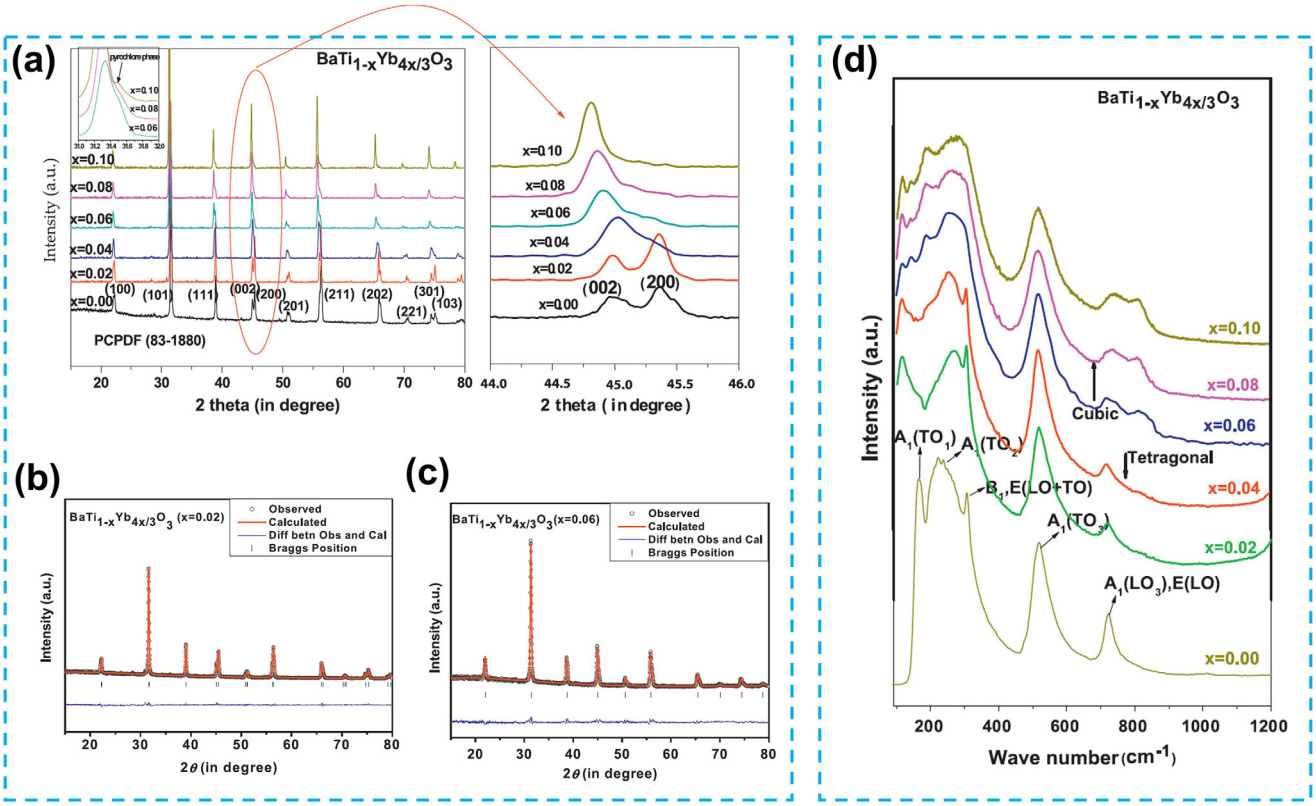


**Figure 19.** a) Cascade XRD patterns of $Ba(Ti_{1-x}Yb_{4x/3})O_3$ along with the shifting and merging of the peaks of $Ba(Ti_{1-x}Yb_{4x/3})O_3$ with increasing doping concentration, final Rietveld refinements of $Ba(Ti_{1-x}Yb_{4x/3})O_3$ for b) $x = 0.02$ (s.g. *P4mm*) and c) $x = 0.06$ (s.g. *Pm-3m* ) and d) Raman spectra of $Ba(Ti_{1-x}Yb_{4x/3})O_3$ at RT. Modified with permission.[335] Copyright 2013, Elsevier.

Band structure analysis showed that Yb-doping modifies the electrical properties of BTO by introducing magnetism. Additionally, Yb-doping significantly enhanced the dielectric constants of BTO at both the Ba and Ti-sites. While the influence of Yb-doping on the dielectric properties of $Yb^{3+}$-doped BTO, in which $Yb^{3+}$ replaces Ti-sites in the BTO host, has been extensively documented, empirical studies that thoroughly investigate the behavior of the dielectric constant after the incorporation of $Yb^{3+}$ at $Ba^{2+}$ sites are extremely scarce in the literature. Strong evidence for such behavior is provided by Tsur et al.[39,40,77] who show that $Yb^{3+}$ is relatively small and therefore mainly occupies the B-site, but that some degree of amphotericity is still possible. Namely, in their studies, the authors show that a signal of $Yb^{3+}$ in BTO doped with 1 at.% Yb is observed with EPR at 10 K. EPR showed that Yb was on the B-site and that the signal intensity was the same whether the sample was Ba (Ba/Ti = 1.01) or Ti-rich (Ba/Ti = 0.99) or not. In addition, no signal was observed for $Yb^{3+}$ on the A-site.

Looking at the perovskite structure of BTO host, the incorporation of trivalent Ln cations ($Ho^{3+}$, $Dy^{3+}$, $Er^{3+}$, $Yb^{3+}$) changes the microstructural and electrical properties of doped BTO. At low donor concentrations (<0.5 wt%), the ceramic forms a bimodal microstructure with anomalous grain development, resulting in semiconducting characteristics at RT and a positive temperature coefficient effect.[64,336–338] On the other hand, a higher donor concentration leads to dielectric properties of the ceramics with high breakdown voltage. For example, a low $Ho^{3+}$-doping level leads to the substitution of $Ba^{2+}$, resulting in the formation of $Ba_{(1-x)}Ho_xTiO_3$ solid solutions. If the concentration of Ln dopants is higher than 1.0 wt%, substitution of $Ba^{2+}$ or $Ti^{4+}$ ions can occur. However, in this case the electrical resistance is very high.[69,339]

## 3. Conclusion

Understanding the defect chemistry of Ln-doped BTO and the distribution of Ln ions in the BTO host, has long opposed a significant challenge in the study of functional perovskite oxides. In this review, we provide a comprehensive overview of the structural and microstructural features of BTO materials doped with members of Ln family. We emphasize their correlation with superior properties that surpass those of the pure BTO and, in particular, highlight the potential of 2D ferroelectric BTO materials that are emerging on the horizon, but are still in their infancy. Notably, defects located at different positions within BTO host can affect the piezocatalytic reactions in low-dimensional BTO in distinct ways. In addition, different sintering temperatures and holding times throughout the synthesis procedures result in different microstructures with different grain sizes and morphologies, leading to improved dielectric, ferroelectric, and piezoelectric responses in the Ln-doped BTO materials. Therefore, the intricate (micro)structure-property relationships in these materials must be thoroughly researched in order to design intelligent systems. On the other hand, the growing need for ceramic

formulations with superior microstructure necessitates the use of very precise mathematical models. To construct credible ceramic modeling, one must first comprehend conventional synthesis methodologies as well as defect chemistry principles.

The defect chemistry is summarized systematically and the underlying doping mechanisms of each Ln member are explored from both, experimental and theoretical perspectives, from early-stage studies to the latest findings published in 2024.

It is well-established that the position of the individual dopants is influenced by their ionic radius. However, the formation of individual defects induced by doping, such as vacancies, significantly impacts the ferroelectric, ferromagnetic, luminescent properties, and piezocatalytic properties of BTO. These effects are strongly dependent on the sample preparation methods and dopant concentrations. To comprehend the distribution and influence of Ln ions within the BTO lattice, it is essential to determine the preferred doping site, the solubility limit at each site, and the effects of Ln concentration on these properties. Understanding the atomic arrangement around the Ln ions and the neighboring host ions is crucial, as well as identifying defects arising from charge-compensation mechanisms such as cation and anion vacancies.

In addition to the collection of XRD data, Raman spectroscopy, and EPR measurements, complementary techniques such as XAS and PDF analyses would undoubtedly provide deeper insights into the short-range order of these materials. When combined with cutting-edge technologies, such as artificial intelligence and machine learning, these methods could unlock new avenues for Ln-doped BTO-based materials in the future. The addition of Ln dopants to BTO improves the dielectric response, reduces the dissipation factor, and controls $T_c$, grain formation, and electrical resistivity. However, under high pressure, Ln-doped BTO may achieve metallic conductivity. From a critical perspective, the application of mechanical pressure to these systems presents untapped opportunities. The relationship between the structural and physicochemical properties of Ln-doped BTO under high pressure, has rarely been explored, with Eu-doped BTO being the only reported example. Discrete changes in the crystal structure and electronic landscape of Ln-doped BTO under high pressure may yield intricate features worthy of further exploration.

Nonetheless, it is undeniable that the most important insights into the structural and defect chemistry of Ln-doped BTO were gained at the beginning of this century, particularly in the study of La-doped BTO and Ce-doped BTO. This raises an obvious question: why? First, no other group of elements in the periodic table exhibits the same degree of self-similarity as the lanthanides. Second, Ln oxides are widely utilized in both established markets (e.g., catalysts, glass manufacturing, lighting, metallurgy) and emerging markets (e.g., battery alloys, ceramics, magnets), which account for about 60% and 40% of total RE consumption, respectively. In the traditional market sectors, La and Ce constitute about 80% of the RE elements used, while in newer applications Dy, Nd and Pr make up roughly 85%. Within the established end-use markets for Ln oxides (e.g., catalysts, glass industry, metallurgy – excluding battery alloys and phosphors) Ce (45%), La (39%), and Y (8%) oxides dominate. Dy, Gd, Nd, Pr, and other Ln oxides collectively account for the remaining 7% of the total Ln oxide usage in these industries. Looking ahead, further research on the incorporation of Ln dopants into perovskite structures can undoubtedly be expected, although probably not on the same scale or at the same fundamental level as during the late 1990s and early 2000s. Future research is expected to align closely with low-carbon transition strategies and renewable technologies which will drive the demand for use of Ln-doped BTO. These advancements will rely heavily on the principles of structural and defect chemistry.

## Acknowledgements

This work was supported by the Beijing Natural Science Foundation (No. IS24025). The authors thank the European Union and the Ruđer Bošković Institute in Zagreb for their financial support under the NextGenerationEU. The Cyprus University of Technology in Cyprus is gratefully acknowledged.

## Conflict of Interest

The authors declare no conflict of interest.

## Keywords

barium titanate, charge compensation schemes, crystal structure, defect chemistry, lanthanides, microstructure, rare-earth elements

Received: January 19, 2025
Revised: April 5, 2025
Published online: May 12, 2025

[1] X. Cai, Y. Luo, B. Liu, H. M. Cheng, *Chem. Soc. Rev.* **2018**, *47*, 6224.
[2] C. Tan, X. Cao, X. J. Wu, Q. He, J. Yang, X. Zhang, J. Chen, W. Zhao, S. Han, G. H. Nam, *Chem. Rev.* **2017**, *117*, 6225.
[3] R. Liu, X. R. Shi, Y. Wen, X. Shao, C. Su, J. Hu, S. Xu, *J. Energy Chem.* **2022**, *74*, 149.
[4] Y. Zhu, L. Peng, Z. Fang, C. Yan, X. Zhang, G. Yu, *Adv. Mater.* **2018**, *30*, 1706347.
[5] X. Zhang, L. Hou, A. Ciesielski, P. Samorì, *Adv. Energy Mater.* **2016**, *6*, 1600671.
[6] X. Zhang, C. Sun, S. Xu, M. Huang, Y. Wen, X. R. Shi, *Nano. Res.* **2022**, *15*, 8897.
[7] C. C. Jin, D. M. Liu, L. X. Zhang, *Small* **2023**, *19*, 2303586.
[8] W. Liu, X. Ren, *Phys. Rev. Lett.* **2009**, *103*, 257602.
[9] C. Yu, J. He, M. Tan, Y. Hou, H. Zeng, C. Liu, H. Meng, Y. Su, L. Qiao, T. Lookman, Y. Bai, *Adv. Funct. Mater.* **2022**, *32*, 2209365.
[10] J. Wei, J. Xia, X. Liu, P. Ran, G. Zhang, C. Wang, X. Li, *Appl. Catal. B* **2023**, *328*, 122520.
[11] C. Yu, S. Lan, S. Cheng, L. Zeng, M. Zhu, *J. Hazard. Mater.* **2022**, *424*, 127440.
[12] J. Lei, C. Wang, X. Feng, L. Ma, X. Liu, Y. Luo, L. Tan, S. Wu, C. Yang, *J. Chem. Eng.* **2022**, *435*, 134624.
[13] P. Wang, X. Li, S. Fan, X. Chen, M. Qin, D. Long, M. O. Tadé, S. Liu, *Appl. Catal. B* **2020**, *279*, 119340.
[14] D. M. Liu, J. T. Zhang, C. C. Jin, B. B. Chen, J. Hu, R. Zhu, F. Wang, *Nano Energy* **2022**, *95*, 106975.
[15] C. C. Jin, J. D. Ai, D. M. Liu, L. N. Tan, L. Cao, B. L. Shen, X. T. Qiu, L. X. Zhang, *J. Mater. Chem. A Mater.* **2023**, *11*, 10360.
[16] X. Xue, R. Chen, H. Chen, Y. Hu, Q. Ding, Z. Liu, L. Ma, G. Zhu, W. Zhang, Q. Yu, J. Liu, J. Ma, Z. Jin, *Nano. Lett.* **2018**, *18*, 7372.

[17] M. Ji, J. H. Kim, C. H. Ryu, Y. I. Lee, *Nano Energy* **2022**, *95*, 106993.
[18] K. Hagiwara, K. N. Byun, S. Morita, E. Yamamoto, M. Kobayashi, X. Liu, M. Osada, *Adv. Electron. Mater.* **2023**, *9*, 2201239.
[19] H. I. Hsiang, Y. L. Chang, J. S. Fang, F. S. Yen, *J. Alloys Compd.* **2011**, *509*, 7632.
[20] T. Kubo, M. Hogiri, H. Kagata, A. Nakahira, *J. Am. Ceram. Soc.* **2009**, *92*, S172.
[21] H. Katsuki, S. Komarneni, *JCS-Japan* **2011**, *119*.
[22] K. K. Lee, Y. C. Kang, K. Y. Jung, J. H. Kim, *J. Alloys Compd.* **2005**, *395*, 280.
[23] M. Kubin, P. Makreski, M. Zanoni, L. Gasperini, G. Selleri, D. Fabiani, C. Gualandi, A. Bužarovska, *Polym. Test.* **2023**, *126*, 108158.
[24] D. S. Jung, S. K. Hong, J. S. Cho, Y. C. Kang, *J. Eur. Ceram. Soc.* **2008**, *28*, 109.
[25] W. Zhu, S. A. Akbar, R. Asiaie, P. K. Dutta, *Jpn. J. Appl. Phys.* **1997**, *36*, 214.
[26] P. K. Dutta, R. Asiaie, S. A. Akbar, W. Zhu, *Chem. Mater.* **1994**, *6*, 1542.
[27] H. Xu, L. Gao, *J. Am. Ceram. Soc.* **2003**, *86*, 203.
[28] W. Luan, L. Gao, J. Guo, *Ceram. Int.* **1999**, *25*, 727.
[29] P. Zheng, J. L. Zhang, Y. Q. Tan, C. L. Wang, *Acta. Mater.* **2012**, *60*, 5022.
[30] I. Fujii, M. Ugorek, S. Trolier-Mckinstry, *J. Appl. Phys.* **2010**, *107*, 104116.
[31] C. Zhao, Y. Huang, J. Wu, *InfoMat* **2020**, *2*, 1163.
[32] C. Deng, Y. Zhang, D. Yang, H. Zhang, M. Zhu, *Adv. Sens. Res.* **2024**, *3*, 2300168.
[33] M. Zhu, Z. Du, S. S. Chng, S. H. Tsang, E. H. T. Teo, *J. Mater. Chem. C Mater.* **2018**, *6*, 12919.
[34] F. D. Morrison, D. C. Sinclair, A. R. West, *J. Appl. Phys.* **1999**, *86*, 6355.
[35] K. M. Batoo, R. Verma, A. Chauhan, R. Kumar, M. Hadi, O. M. Aldossary, Y. Al Douri, *J. Alloys Compd. 883*, 160836.
[36] M. Arshad, H. Du, M. S. Javed, A. Maqsood, I. Ashraf, S. Hussain, W. Ma, H. Ran, *Ceram. Int.* **2020**, *46*, 2238.
[37] J. K. Lee, K. S. Hong, J. W. Jang, *J. Am. Ceram. Soc.* **2001**, *84*, 2001.
[38] M. A. Rahman, *J. Asian Ceram. Soc.* **2015**, *11*, 215.
[39] Y. Tsur, T. D. Dunbar, C. A. Randall, *J. Electroceram.* **2001**, *7*, 25.
[40] Y. Tsur, A. Hitomi, I. Scrymgeour, C. A. Randall, *JJAP, Part 1: Regular Papers and Short Notes and Review Papers* **2001**, *40*, 255.
[41] Y. Feng, J. Wu, Q. Chi, W. Li, Y. Yu, W. Fei, *Chem. Rev.* **2020**, *120*, 1710.
[42] V. Sharma, G. Pilania, G. A. Rossetti, K. Slenes, R. Ramprasad, *Phys. Rev. B Condens. Matter Mater Phys.* **2013**, *87*, 134109.
[43] R. D. Shannon, *Acta Crystallogr. Section A* **1976**, *32*, 751.
[44] D. Y. Lu, M. Toda, M. Sugano, *J. Am. Ceram. Soc.* **2006**, *89*, 3112.
[45] T. D. Dunbar, W. L. Warren, B. A. Tuttle, C. A. Randall, Y. Tsur, *J. Phys. Chem. B* **2004**, *108*, 908.
[46] M. M. Vijatović Petrović, A. Radojković, J. D. Bobić, A. Dzunuzovic, N. Ilic, B. D. Stojanović, *J. Mater. Sci.* **2019**, *54*, 6038.
[47] J. B. Yin, X. P. Zhao, *J. Solid State. Chem.* **2004**, *177*, 3650.
[48] M. García-Hernández, A. García-Murillo, F. D. J. Carrillo-Romo, Á. D. J. Morales-Ramírez, M. A. Meneses-Nava, B. Gonzalez-Penguelly, V. G. Febles, *Mater. Trans.* **2013**, *54*, 806.
[49] M. Cernea, O. Monnereau, P. Llewellyn, L. Tortet, C. Galassi, *J. Eur. Ceram. Soc.* **2006**, *26*, 3241.
[50] M. Cernea, B. S. Vasile, P. Ganea, R. Radu, V. Mihalache, A. Husanu, *J. Am. Ceram. Soc.* **2011**, *94*, 736.
[51] Q. Sun, Q. Gu, K. Zhu, R. Jin, J. Liu, J. Wang, J. Qiu, *Sci. Rep.* **2017**, *7*, 42274.
[52] Z. Yang, J. Wang, Y. Hu, C. Deng, K. Zhu, J. Qiu, *Compos. Part A Appl. Sci. Manuf.* **2020**, *128*, 105675.
[53] M. García-Hernández, A. García-Murillo, J. De, F. Carrillo-Romo, D. Jaramillo-Vigueras, G. Chadeyron, E. De La Rosa, D. Boyer, *Int. J. Mol. Sci.* **2009**, *10*, 4088.
[54] M. Cernea, C. Galassi, B. S. Vasile, P. Ganea, R. Radu, G. Ghita, *J. Mater. Res.* **2010**, *25*, 1057.
[55] X. Chou, J. Zhai, H. Jiang, X. Yao, *J. Appl. Phys.* **2007**, *102*, 084106.
[56] S. Hao, J. Li, W. Wang, D. Fu, C. Wang, Q. Shang, *Res. Chem. Intermediat.* **2013**, *39*, 2705.
[57] H. Beltrán, E. Cordoncillo, P. Escribano, D. C. Sinclair, A. R. West, *J. Am. Ceram. Soc.* **2004**, *87*, 2132.
[58] Z. Xinle, M. Zhimei, X. Zuojiang, C. Guang, *J. Rare Earths* **2006**, *24*, 82.
[59] J. B. Liu, W. C. Li, Z. M. Wang, C. P. Zheng, *Mater. Sci. Technolog.* **2001**, *17*, 606.
[60] H. Zu, Q. Fu, C. Gao, T. Chen, D. Zhou, Y. Hu, Z. Zheng, W. Luo, *J. Eur. Ceram., Soc.* **2018**, *38*, 113.
[61] M. A. Gomes, Á. S. Lima, K. I. B. Eguiluz, G. R. Salazar-Banda, *J. Mater. Sci.* **2016**, *51*, 4709.
[62] F. A. Ismail, R. A. M. Osman, M. S. Idris, *AIP Conf. Proc.* **2016**, *1756*, 090005.
[63] V. Paunović, L. Živković, L. Vračar, V. Mitić, M. Miljković, , *Serb. J. Electr. Eng.* **2004**, *1*, 89.
[64] H. Kishi, N. Kohzu, J. Sugino, H. Ohsato, Y. Iguchi, T. Okuda, *J. Eur. Ceram. Soc.* **1999**, *19*, 1043.
[65] L. A. Xue, Y. Chen, R. J. Brook, *Mate. Sci. Eng. B* **1988**, *1*, 193.
[66] F. A. Ismail, R. A. M. Osman, M. S. Idris, N. A. M. A. Hambali, *Ceramics, Solid State Phenom.* **2018**, *280*, 127.
[67] J. Chun, J. Heo, K. S. Lee, B. U. Ye, B. S. Kang, S. H. Yoon, *Sci. Rep.* **2024**, *14*, 616.
[68] J. H. Hwang, Y. H. Han, *JJAP, Part 1: Regular Papers and Short Notes and Review Papers* **2001**, *40*, 676.
[69] V. V. Mitić, Z. S. Nikolić, V. B. Pavlović, V. Paunović, M. Miljković, B. Jordović, L. Živković, *J. Am. Ceram. Soc.* **2010**, *93*,132.
[70] H. Moriwake, C. A. J. Fisher, A. Kuwabara, *Jpn. J. Appl. Phys.* **2009**, *48*, 09KC03.
[71] A. Honda, S. Higai, Y. Motoyoshi, N. Wada, H. Takagi, *Jpn. J. Appl. Phys.* **2011**, *50*, 09NE01.
[72] X. Cheng, Y. C. Zhen, P. Zhao, K. Hui, M. Xiao, L. Guo, Z. Fu, X. Cao, L. Li, X. Wang, *J. Am. Ceram. Soc.* **2023**, *106*, 5294.
[73] H. Lee, M. Ouk, I. Kim, B. Kim, S. Bae, S. D. Roh, I. Tanaka, M. Choi, *Curr. Appl. Phys.* **2024**, *68*, 238.
[74] Y. Wang, S. Shi, Q. Dong, C. Xu, S. Zhu, X. Zhang, Y. T. Chow, X. Wang, G. Zhang, L. Zhu, D. Xu, *Mater. Charact.* **2021**, *172*, 110859.
[75] R. N. Schwartz, B. A. Wechsler, *Phys. Rev. B Condens. Matter Mater Phys.* **2000**, *61*, 8141.
[76] E. Possenriede, O. F. Schirmer, G. Godefroy, *Phys. Status Solidi B* **1990**, *161*, K55
[77] Y. Tsur, A. Hitomi, I. Scrymgeour, C. A. Randall, *Jpn. J. Appl. Phys* **2001**, *40*, 255.
[78] M. T. Buscaglia, V. Buscaglia, M. Viviani, P. Nanni, M. Hanuskova, *J. Eur. Ceram. Soc.* **2000**, *20*, 1997.
[79] G. V. Lewis, C. R. A. Catlow, *J. Phys. Chem. Solids* **1986**, *47*, 89.
[80] M. T. Buscaglia, V. Buscaglia, M. Viviani, P. Nanni, *J. Am. Ceram. Soc.* **2001**, *84*, 376.
[81] S. Makishima, K. Hasegawa, S. Shionoya, *J. Phys. Chem. Solids* **1962**, *23*, 749.
[82] L. Ben, D. C. Sinclair, *Appl. Phys. Lett.* **2011**, *98*, 092907.
[83] J. A. Dawson, D. C. Sinclair, J. H. Harding, C. L. Freeman, *Chem. Mater.* **2014**, *26*, 6104.
[84] F. A. Rabuffetti, S. P. Culver, J. S. Lee, R. L. Brutchey, *Nanoscale* **2014**, *6*, 2909.
[85] M. C. Ferrarelli, C. C. Tan, D. C. Sinclair, *J. Mater. Chem.* **2011**, *21*, 6292.
[86] F. D. Morrison, A. M. Coats, D. C. Sinclair, A. R. West, *J. Electroceram.* **2001**, *6*, 219.
[87] F. D. Morrison, D. C. Sinclair, A. R. West, *J. Am. Ceram. Soc.* **2001**, *84*, 474.

[88] C. L. Freeman, J. A. Dawson, J. H. Harding, L. B. Ben, D. C. Sinclair, *Adv. Funct. Mater.* **2013**, *23*, 491.
[89] S. Guillemet-Fritsch, Z. Valdez-Nava, C. Tenailleau, T. Lebey, B. Durand, J. Y. Chane-Ching, *Adv. Mater.* **2008**, *20*, 551.
[90] X. He, H. J. Lee, S. S. Ryu, Y. K. Choi, H. Ju, *J. Korean Phys. Soc.* **2014**, *65*, 404.
[91] C. L. Freeman, J. A. Dawson, H. R. Chen, J. H. Harding, L. B. Ben, D. C. Sinclair, *J. Mater. Chem.* **2011**, *21*, 4861.
[92] G. V. Lewis, C. R. A. Catlow, *J. Phys. C: Solid State Phys.* **1985**, *18*, 1149.
[93] D. Makovec, Z. Samardžija, M. Drofenik, *J. Am. Ceram. Soc.* **2004**, *87*, 1324.
[94] L. Rimai, G. A. DeMars, *Phys. Rev.* **1962**, *127*, 702.
[95] M. Yashima, T. Hoshina, D. Ishimura, S. Kobayashi, W. Nakamura, T. Tsurumi, S. Wada, *J. Appl. Phys.* **2005**, *98*, 014313.
[96] R. D. Burbank, H. T. Evans, *Acta. Cryst.* **1948**, *1*, 330.
[97] S. Tsunekawa, S. Ito, T. Mori, K. Ishikawa, Z.-Q. Li, Y. Kawazoe, *Phys. Rev. B Condens. Matter Mater. Phys.* **1997**, *67*, 019901.
[98] S. Wada, M. Narahara, T. Hoshina, H. Kakemoto, T. Tsurumi, *J. Mater. Sci.* **2003**, *38*, 2655.
[99] S. Wada, H. Yasuno, T. Hoshina, S. M. Nam, H. Kakemoto, T. Tsurumi, *JJAP, Part 1: Regular Papers and Short Notes and Review Papers* **2003**, *42*, 6188.
[100] G. H. Kwei, A. C. Lawson, S. J. L. Billinge, S. W. Cheong, *J. Phys. Chem.* **1993**, *97*, 2368.
[101] C. H. Perry, D. B. Hall, *Phys. Rev. Lett.* **1965**, *15*, 700.
[102] M. Deluca, A. Gajović, *Raman Spectroscopy of Nanostructured Ferroelectric Materials, Nanoscale Ferroelectrics and Multiferroics: Key Processing and Characterization Issues, and Nanoscale Effects*, Vol. *I* & *II* (Eds: M. Algueró, J. Marty Gregg, L. Mitoseriu), John Wiley & Sons **2016**, https://onlinelibrary.wiley.com/doi/10.1002/9781118935743.ch11.
[103] S. Miao, J. Pokorny, U. M. Pasha, O. P. Thakur, D. C. Sinclair, I. M. Reaney, *J. Appl. Phys.* **2009**, *106*, 114111.
[104] B. Ravel, E. A. Stern, R. I. Vedrinskii, V. Kraizman, *Ferroelectrics* **1998**, *206*, 407.
[105] N. Inoue, T. Okamatsu, A. Ando, H. Takagi, T. Hashimoto, C. Moriyoshi, Y. Kuroiwa, *Jpn. J. Appl. Phys.* **2009**, *48*, 09KF03.
[106] M. Gaudon, *Polyhedron* **2015**, *88*, 6.
[107] C. J. Xiao, C. Q. Jin, X. H. Wang, *Mater. Chem. Phys.* **2008**, *111*, 209.
[108] V. Buscaglia, C. A. Randall, *J. Eur. Ceram. Soc.* **2020**, *40*, 3744.
[109] T. M. Shaw, S. Trolier-McKinstry, P. C. McIntyre, *Annu. Rev. Mater. Sci.* **2000**, *30*, 263.
[110] J. F. Ihlefeld, D. T. Harris, R. Keech, J. L. Jones, J. P. Maria, S. Trolier-McKinstry, *J. Am. Ceram. Soc.* **2016**, *99*, 2537.
[111] J. E. Spanier, A. M. Kolpak, J. J. Urban, I. Grinberg, L. Ouyang, W. S. Yun, A. M. Rappe, H. Park, *Nano Lett.* **2006**, *6*, 735.
[112] R. D. Burbank, H. T. Evans, *Acta Crystallogr.* **1948**, *1*, 330.
[113] H. Wang, B. Liu, X. Wang, *J. Alloys Compd.* **2020**, *817*, 152804.
[114] Y. Meng, K. Liu, X. Zhang, X. Lei, J. Chen, Z. Yang, B. Peng, C. Long, L. Liu, C. Li, *J. Am. Ceram. Soc.* **2022**, *105*, 5725.
[115] J. B. MacChesney, P. K. Gallagher, F. V. DiMarcello, *J. Am. Ceram. Soc.* **1963**, *46*, 197.
[116] O. Saburi, *J. Phys. Soc. Jpn.* **1959**, *14*, 1159.
[117] G. H. Jonker, E. E. Havinga, *Mater. Res. Bull.* **1982**, *17*, 345.
[118] N. G. Eror, D. M. Smyth, in *Chemistry of Extended Defects in Non-Metallic Solids, Proc Inst for Advanced Study*, Vol. *62* (Eds: L. Eyring, M. O'Keefe), North-Holland, Amsterdam **1970**.
[119] D. Makovec, Z. Samardžija, U. Delalut, D. Kolar, *J. Am. Ceram. Soc.* **1995**, *78*, 2193.
[120] H. M. Chan, M. R. Harmer, D. M. Smyth, *J. Am. Ceram. Soc.* **1986**, *69*, 507.
[121] D. M. Smyth, *J. Electroceram.* **2002**, *9*, 179.
[122] A. Ianculescu, Z. V. Mocanu, L. P. Curecheriu, L. Mitoseriu, L. Padurariu, R. Truc, *J. Alloys. Compd.* **2011**, *509*, 10040.
[123] G. H. Jonker, *Solid State Electron* **1964**, *7*, 895.
[124] L. Liu, H. Guo, H. Lü, S. Dai, B. Cheng, Z. Chen, *J. Appl. Phys.* **2005**, *97*, 054102.
[125] H. J. Sumona, M. S. Sultan, S. A. Urmi, M. A. Gafur, *Mater. Sci. Eng. B* **2023**, *298*, 116844.
[126] C.-J. Peng, H.-Y. Lu, *J. Am. Ceram. Soc.* **1988**, *71*, C44.
[127] S.-M. Hwang, J.-C. Lim, S.-I. l Kim, J.-Y. Kim, J. Hwang, C.-H. Lee, N. Kwon, I. Kim, K. Lee, S. Park, S.-M. Bae, J.-H. Hwang, K. Lee, H.-S. Kim, *J. Eur. Ceram. Soc.* **2024**, *44*, 5471.
[128] W. J. Choi, D. Yang, S. C. Jeon, K. S. Moon, *J. Alloys Compd.* **2022**, *916*, 165388.
[129] M. D. Glinchuk, I. P. Bykov, S. M. Kornienko, V. V. Laguta, A. M. Slipenyuk, A. G. Bilous, O. I. V'yunov, O. Z. Yanchevskii, *J. Mater. Chem.* **2000**, *10*, 941.
[130] X. Zhu, J. Zhu, S. Zhou, Z. Liu, N. Ming, D. Hesse, *J. Cryst. Growth* **2005**, *283*, 553.
[131] M. Ganguly, S. K. Rout, T. P. Sinha, S. K. Sharma, H. Y. Park, C. W. Ahn, I. W. Kim, *J. Alloys Compd.* **2013**, *579*, 473.
[132] Z. Valdez-Nava, S. Guillemet-Fritsch, C. Tenailleau, T. Lebey, B. Durand, J. Y. Chane-Ching, *J. Electroceram.* **2009**, *22*, 238.
[133] F. D. Morrison, D. C. Sinclair, A. R. West, *Int. J. Inorg. Mater.* **2001**, *3*, 1205.
[134] J. Long, L. Yang, X. Wei, *J. Alloys Compd.* **2013**, *549*, 336.
[135] H. Gao, J. Cao, L. Liu, Y. Yang, *J. Mol. Struct.* **2011**, *1003*, 75.
[136] D. D. Gulwade, S. M. Bobade, A. R. Kulkarni, P. Gopalan, *J. Appl. Phys.* **2005**, *97*, 074106.
[137] K. Aliouane, A. Guehria-Laidoudi, A. Simon, J. Ravez, *Solid State Sci.* **2005**, *7*, 1324.
[138] H. A. Ávila, L. A. Ramajo, M. M. Reboredo, M. S. Castro, R. Parra, *Ceram. Int.* **2011**, *37*, 2383.
[139] A. Yamaji, Y. Enomoto, K. Kinoshita, T. Murakami, *J. Am. Ceram. Soc.* **1977**, *60*, 97.
[140] Y. Wang, K. Miao, W. Wang, Y. Qin, *J. Eur. Ceram. Soc.* **2017**, *37*, 2385.
[141] N. Wongdamnern, N. Triamnak, T. Sareein, R. Yimnirun, *Integr. Ferroelectr.* **2021**, *223*, 258.
[142] R. Ranjitha Mathiarasu, K. Panneerselvam, B. Selvaraj, S. Dharmaraj, V. Ashokkumar, P. L. Show, M. George, *Sustain. Energy Technol. Assess.* **2022**, *53*, 102604.
[143] R. R. Mathiarasu, A. Manikandan, J. N. Baby, K. Panneerselvam, R. Subashchandrabose, M. George, Y. Slimani, M. A. Almessiere, A. Baykal, *Phys. B: Condens. Matter.* **2021**, *615*, 413068.
[144] D. Makovec, Z. Samardžija, D. Kolar, *J. Solid State Chem.* **1996**, *123*, 30.
[145] L. P. Curecheriu, C. E. Ciomaga, V. Musteata, G. Canu, V. Buscaglia, L. Mitoseriu, *Ceram. Int.* **2016**, *42*, 11085.
[146] L. P. Curecheriu, M. Deluca, Z. V. Mocanu, M. V. Pop, V. Nica, N. Horchidan, M. T. Buscaglia, V. Buscaglia, M. Van Bael, A. Hardy, *Ph. Transit.* **2013**, *86*, 703.
[147] C. Ang, Z. Yu, Z. Jing, R. Guo, A. S. Bhalla, L. E. Cross, *Appl. Phys. Lett.* **2002**, *80*, 3424.
[148] Y. Park, Y. Kim, *J. Mater. Res.* **1995**, *10*, 2770.
[149] D. Y. Lu, X. Y. Sun, M. Toda, *J. Phys. Chem. Solids* **2007**, *68*, 650.
[150] K. Watanabe, H. Ohsato, H. Kishi, Y. Okino, N. Kohzu, Y. Iguchi, T. Okuda, *Solid State Ion.* **1998**, *108*, 129.
[151] D. Padalia, G. Bisht, U. C. Johri, K. Asokan, *Solid State Sci.* **2013**, *19*, 122.
[152] Y. Zhuang, Z. Xu, F. Li, Z. Liao, W. Liu, *RSC Adv.* **2015**, *5*, 55269.
[153] C. Ang, Z. Jing, Z. Yu, *J. Condens. Matter Phys.* **2002**, *14*, 8901.
[154] Y. Zhuang, Z. Xu, X. Fu, F. Li, J. Li, Z. Liao, W. Liu, *Semicond. Sci. Technol.* **2017**, *32*, 074002.

[155] G. Canu, G. Confalonieri, M. Deluca, L. Curecheriu, M. T. Buscaglia, M. Asandulesa, N. Horchidan, M. Dapiaggi, L. Mitoseriu, V. Buscaglia, *Acta Mater.* **2018**, *152*, 258.
[156] G. Confalonieri, V. Buscaglia, G. Capitani, G. Canu, N. Rotiroti, A. Bernasconi, A. Pavese, M. Dapiaggi, *J. Appl. Crystallogr.* **2018**, *51*, 1283.
[157] D. Y. Lu, D. D. Han, X. Y. Sun, X. L. Zhuang, Y. F. Zhang, *Jpn. J. Appl. Phys.* **2013**, *52*, 111501.
[158] R. V. K. Mangalam, N. Ray, U. V. Waghmare, A. Sundaresan, C. N. R. Rao, *Solid State Commun.* **2009**, *149*, 1.
[159] A. Sundaresan, R. Bhargavi, N. Rangarajan, U. Siddesh, C. N. R. Rao, *Phys. Rev. B Condens. Matter Mater. Phys.* **2006**, *74*, 161306(R).
[160] P. Senthilkumar, S. Dhanuskodi, J. Karthikeyan, P. Murugan, *Phys. Chem. Chem. Phys.* **2019**, *21*, 4032.
[161] A. R. Albuquerque, A. Bruix, I. M. G. Dos Santos, J. R. Sambrano, F. Illas, *J. Phys. Chem. C* **2014**, *118*, 9677.
[162] P. Senthilkumar, S. Dhanuskodi, M. Muneeswaran, N. V. Giridharan, S. Kuila, P. N. Vishwakarma, *J. Appl. Phys.* **2018**, *123*, 244101.
[163] K. C. Verma, R. K. Kotnala, *Phys. Chem. Chem. Phys.* **2016**, *18*, 5647.
[164] J. Dhanalakshmi, S. Iyyapushpam, S. T. Nishanthi, M. Malligavathy, D. P. Padiyan, *Adv. Nat. Sci.: Nanosci.* **2017**, *8*, 015015.
[165] S. Fuentes, N. Barraza, E. Veloso, R. Villarroel, J. Llanos, *J. Alloys Compd.* **2013**, *569*, 52.
[166] P. Senthilkumar, D. A. Jency, T. Kavinkumar, D. Dhayanithi, S. Dhanuskodi, M. Umadevi, S. Manivannan, N. V. Giridharan, V. Thiagarajan, M. Sriramkumar, et al., *ACS Sustainable Chem. Eng.* **2019**, *7*, 12032.
[167] C. Ang, Z. Yu, Z. Jing, P. M. Vilarinho, J. L. Baptista, *J. Eur. Ceram. Soc.* **1997**, *17*, 1217.
[168] J. Hyun Hwang, Y. Ho Han, *J. Am. Ceram. Soc.* **2004**, *84*, 1750.
[169] K. Brajesh, A. K. Kalyani, R. Ranjan, *Appl. Phys. Lett.* **2015**, *106*, 012907.
[170] S. Liu, L. Zhang, J. Wang, Y. Zhao, X. Wang, *Ceram. Int.* **2017**, *43*, 10683.
[171] X. Moya, S. Kar-Narayan, N. D. Mathur, *Nat. Mater.* **2014**, *13*, 439.
[172] S. P. Alpay, J. Mantese, S. Trolier-Mckinstry, Q. Zhang, R. W. Whatmore, *MRS Bull.* **2014**, *39*, 1099.
[173] A. Kumar, A. Thakre, D. Y. Jeong, J. Ryu, *J. Mater. Chem. C* **2019**, *7*, 6836.
[174] S. G. Lu, Q. Zhang, *Adv. Mater.* **2009**, *21*, 1983.
[175] S. Xie, Y. Bai, F. Han, S. Qin, J. Li, L. Qiao, D. Guo, *J. Alloys Compd.* **2017**, *724*, 163.
[176] F. Han, Y. Bai, L. J. Qiao, D. Guo, *J. Mater. Chem. C* **2016**, *4*, 1842.
[177] S. Mahboob, A. B. Dutta, C. Prakash, G. Swaminathan, S. V. Suryanarayana, G. Prasad, G. S. Kumar, *Mater. Sci. Eng. B* **2006**, *134*, 36.
[178] J. Li, Y. J. Wu, M. Kuwabara, *Key Eng. Mater.* **2006**, *301*, 197.
[179] T. Wei, N. Haiyong, Z. Qiuhong, D. Jianhong, *RSC Adv.* **2018**, *8*, 23996.
[180] M. M. Bućko, A. Wilk, J. Lis, A. Toczek, L. Kozielski, *Process. Appl. Ceram.* **2020**, *14*, 77.
[181] M. K. Adak, D. Dhak, *Mater. Res. Express* **2019**, *6*, 125082.
[182] H. Zou, D. Peng, G. Wu, X. Wang, D. Bao, J. Li, Y. Li, X. Yao, *J. Appl. Phys.* **2013**, *114*, 073103.
[183] A. S. Chabungbam, D. E. Kim, G. Kim, M. Kim, H. S. Lee, S. W. Kim, H. H. Park, *Int. J. Energy Res.* **2024**, *2024*, 197160.
[184] L. Wang, W. Bai, X. Zhao, Y. Ding, S. Wu, P. Zheng, P. Li, J. Zhai, *J. Mater. Sci.: Mater. Electron.* **2020**, *31*, 6560.
[185] Z. Wang, H. Hao, F. Peng, W. Zhang, C. Su, Q. Guo, Z. Yao, M. Cao, H. Liu, *J. Alloys Compd.* **2023**, *945*, 169211.
[186] G. Panchal, D. K. Shukla, R. J. Choudhary, V. R. Reddy, D. M. Phase, *J. Appl. Phys.* **2017**, *122*, 085310.
[187] Y. Iriani, A. Suparmi, A. Marzuki, D. K. Sandi, *Int. J. Thin Film Sci. Technol.* **2022**, *11*, 307.
[188] D. Y. Lu, X. Y. Sun, B. Liu, J. L. Zhang, T. Ogata, *J. Alloys Compd.* **2014**, *615*, 25.
[189] C. Ostos, L. Mestres, M. L. Martínez-Sarrión, J. E. García, A. Albareda, R. Perez, *Solid State Sci.* **2009**, *11*, 1016.
[190] X. Diez-Betriu, J. E. Garcia, C. Ostos, A. U. Boya, D. A. Ochoa, L. Mestres, R. Perez, *Mater. Chem. Phys.* **2011**, *125*, 493.
[191] R. Sagar, S. Madolappa, N. Sharanappa, R. L. Raibagkar, *Mater. Chem. Phys.* **2013**, *140*, 119.
[192] A. P. A. Moraes, A. G. S. Filho, P. T. C. Freire, J. M. Filho, J. C. M'Peko, A. C. Hernandes, E. Antonelli, M. W. Blair, R. E. Muenchausen, L. G. Jacobsohn, et al., *J. Appl. Phys.* **2011**, *109*, 124102.
[193] D. W. Goodwin, *Phys. Bull.* **1979**, *30*, 525.
[194] S. Hufner, B. R. Judd, *Phys. Today* **1979**, *32*, 76.
[195] Y. G. Choi, B. J. Park, K. H. Kim, J. Heo, *Chem. Phys. Lett.* **2003**, *368*, 625.
[196] P. Boutinaud, R. Mahiou, E. Cavalli, M. Bettinelli, *J. Lumin* **2007**, *122*, 430.
[197] M. Schrader, D. Mienert, T. S. Oh, H. I. Yoo, K. D. Becker, *Solid State Sci.* **2008**, *10*, 768.
[198] M. F. Lin, V. K. Thakur, E. J. Tan, P. S. Lee, *J. Mater. Chem.* **2011**, *21*, 16500.
[199] K. Woong Lee, K. Siva Kumar, G. Heo, M.-J. Seong, J.-W. Yoon, *J. Appl. Phys.* **2013**, *114*, 134303.
[200] C. L. Freeman, J. A. Dawson, H. R. Chen, L. Ben, J. H. Harding, F. D. Morrison, D. C. Sinclair, A. R. West, *Adv. Funct. Mater.* **2013**, *23*, 3925.
[201] M. S. Alkathy, F. P. Milton, M. K. Gatasheh, F. L. Zabotto, H. A. Kassim, K. C. J. Raju, J. A. Eiras, *Appl. Phys. A Mater. Sci. Process.* **2024**, *130*, 402.
[202] S. Althobaiti, M. Alghamdi, B. Alamri, A. Madani, *Optik* **2023**, *275*, 170534.
[203] F. Wang, H. Mao, X. Chen, W. Li, Z. Liu, W. Zhang, S. Bai, *J. Mater. Sci.: Mater. Electron.* **2023**, *34*, 1062.
[204] A. S. Shaikh, R. W. Vest, *J. Am. Ceram. Soc.* **1986**, *69*, 689.
[205] Z. Yao, H. Liu, Y. Liu, Z. Wu, Z. Shen, Y. Liu, M. Cao, *Mater. Chem. Phys.* **2008**, *109*, 475.
[206] N. Hirose, J. M. S. Skakle, A. R. West, *J. Electroceram.* **1999**, *3*, 233.
[207] P. Murugaraj, T. R. N. Kutty, M. S. Rao, *J. Mater. Sci.* **1986**, *21*, 3521.
[208] Q. Liu, J. Liu, D. Lu, W. Zheng, *Ceram. Int.* **2018**, *44*, 7251.
[209] S. Sasikumar, T. K. Thirumalaisamy, S. Saravanakumar, S. Asath Bahadur, D. Sivaganesh, I. B. Shameem Banu, *J. Mater. Sci.: Mater. Electron.* **2020**, *31*, 1535.
[210] Q. Liu, J. Liu, D. Lu, W. Zheng, C. Hu, *J. Alloys Compd.* **2018**, *760*, 31.
[211] Z. Raddaoui, R. Lahouli, S. E. L. Kossi, J. Dhahri, K. Khirouni, K. Taibi, *J. Alloys Compd.* **2019**, *771*, 67.
[212] Y. Li, X. Yao, L. Zhang, *Ceram. Int.* **2004**, *30*, 1325.
[213] D. F. K. Hennings, C. Metzmacher, B. S. Schreinemacher, *J. Am. Ceram. Soc.* **2001**, *84*, 179.
[214] D. Hamdi, D. Talantikite-Touati, A. Manseri, A. T. Khodja, A. Souici, *Opt. Mater.* **2024**, *152*, 115387.
[215] X. Cheng, X. Li, G. Chen, H. Cui, *Ceram. Int.* **2017**, *43*, S249.
[216] D. Zhou, X. Cheng, Q. Fu, S. Gong, D. Zhao, *Ceram. Int.* **2012**, *38*, 6389.
[217] N. Zhang, L. Li, J. Yu, *Mater. Lett. 160*, 128.
[218] A. Kumari, K. Kumari, F. Ahmed, A. Alshoaibi, P. A. Alvi, S. Dalela, M. M. Ahmad, R. N. Aljawfi, P. Dua, A. Vij, et al., *Vacuum* **2021**, *184*, 109872.
[219] O. P. Thakur, C. Prakash, *Ph. Transit.* **2003**, *76*, 567.
[220] S. K. Jo, J. S. Park, Y. H. Han, *J. Alloys Compd.* **2010**, *501*, 259.
[221] D. Fu, S. Hao, J. Li, L. Qiang, *J. Rare Earths* **2011**, *29*, 164.
[222] F. Es-saddik, K. Limame, S. Sayouri, T. Lamcharfi, *J. Mater. Sci.: Mater. Electron.* **2019**, *30*, 1821.

[223] I. J. Park, Y. H. Han, *Met. Mater. Int.* **2014**, *20*, 1157.
[224] J. S. Park, Y. H. Han, *Ceram. Int.* **2006**, *32*, 673.
[225] S. Van Der Gijp, M. H. J. Emond, A. J. A. Winnubst, H. Verweij, *J. Eur. Ceram. Soc.* **1999**, *19*, 1683.
[226] V. I. Hernández, D. I. García-Gutiérrez, J. A. Aguilar-Garib, R. J. Nava-Quintero, *Ceram. Int.* **2021**, *47*, 310.
[227] G. Okuma, N. Saito, K. Mizuno, Y. Iwazaki, H. Kishi, A. Takeuchi, M. Uesugi, K. Uesugi, F. Wakai, *Acta Mater.* **2021**, *206*, 116605.
[228] Z. Luo, H. Hao, C. Chen, L. Zhang, Z. Yao, M. Cao, M. Emmanuel, H. Liu, *J. Alloys Compd.* **2019**, *794*, 358.
[229] W. Peng, L. Li, S. Yu, P. Yang, K. Xu, *Ceram. Int.* **2021**, *47*, 29191.
[230] M. Wang, K. Xue, K. Zhang, L. Li, *Ceram. Int.* **2022**, *48*, 22212.
[231] K. Ohnuma, N. Ozaki, Y. Mizuno, T. Hagiwara, K. I. Kakimoto, H. Ohsato, *Ferroelectrics* **2006**, *332*, 7.
[232] H. Feng, H. Wen, Y. Huang, B. Wu, W. Wu, X. Wu, M. Gao, T. Lin, C. Lin, C. Zhao, *J. Alloys Compd.* **2022**, *989*, 174362.
[233] Q. Liu, J. Liu, D. Lu, T. Li, W. Zheng, *Materials* **2019**, *12*, 678.
[234] H. Sun, X. Wang, X. Yao, *Ferroelectrics* **2010**, *404*, 99.
[235] M. Achkar, D. Fasquelle, B. Duponchel, C. Poupin, A. Hadj Sahraoui, S. Longuemart, *Ceram. Int.* **2024**, *50*, 13794.
[236] P. Guan, Y. Zhang, J. Yang, M. Zheng, *Ceram. Int.* **2023**, *49*, 11796.
[237] D. Han, D. Lu, F. Meng, *RSC Adv.* **2019**, *9*, 4469.
[238] I. Sakaguchi, S. Hirose, T. Furuta, K. Watanabe, K. Kageyama, S. Hishita, H. Haneda, N. Ohashi, *Key Eng. Mater.* **2014**, *582*, 189.
[239] N. Kang, M. Kim, H. Song, J. Ryu, *J. Korean Ceram. Soc.* **2024**, *61*, 1070.
[240] M. K. Rath, G. K. Pradhan, B. Pandey, H. C. Verma, B. K. Roul, S. Anand, *Mater. Lett.* **2008**, *62*, 2136.
[241] D. Y. Lu, T. Ogata, H. Unuma, X. C. Li, N. N. Li, X. Y. Sun, *Solid State Ion* **2011**, *201*, 6.
[242] D. Y. Lu, T. Koda, H. Suzuki, M. Toda, *J. Ceram. Soc. Jpn.* **2005**, *113*, 721.
[243] D. Padalia, U. Kumar, P. Bhandari, J. Dalal, L. Ranakoti, T. Singh, *J. Mater. Sci.: Mater. Electron.* **2024**, *35*, 1375.
[244] S. Sasikumar, H. Fan, W. Wang, S. Saravanakumar, D. Sivaganesh, K. Aravinth, *J. Mater. Sci.: Mater. Electron.* **2021**, *32*, 12253.
[245] L. V. Maneeshya, S. S. Lekshmy, P. V. Thomas, K. Joy, *J. Mater. Sci.: Mater. Electron* **2021**, *25*, 2507.
[246] F. A. Rabuffetti, R. L. Brutchey, *J. Am. Chem. Soc.* **2012**, *134*, 9475.
[247] V. Petkov, V. Buscaglia, M. T. Buscaglia, Z. Zhao, Y. Ren, *Phys. Rev. B Condens. Matter Mater. Phys.* **2008**, *78*, 054107.
[248] P. Serna-Gallén, H. Beltrán-Mir, E. Cordoncillo, A. R. West, R. Balda, J. Fernández, *J. Mater. Chem. C* **2019**, *7*, 13976.
[249] V. Mishra, A. Sagdeo, V. Kumar, M. K. Warshi, H. M. Rai, S. K. Saxena, D. R. Roy, V. Mishra, R. Kumar, P. R. Sagdeo, *J. Appl. Phys.* **2017**, *122*, 065105.
[250] S. H. Wemple, *Phys. Rev. B* **1970**, *2*, 2679.
[251] M. K. Mahata, T. Koppe, K. Kumar, H. Hofsäss, U. Vetter, *Sci. Rep.* **2020**, *10*, 8775.
[252] D. Kumar Singh, K. Mondal, J. Manam, *Ceram. Int.* **2017**, *43*, 13602.
[253] A. De, M. A. Hernández-Rodríguez, A. N. Carneiro Neto, V. Dwij, V. Sathe, L. D. Carlos, R. Ranjan, *J. Mater. Chem. C* **2023**, *11*, 6095.
[254] Z. Xing, H. Suo, F. Chun, X. Wei, F. Wang, *ACS Appl. Mater. Interfaces* **2024**, *16*, 13972.
[255] T. Kolodiazhnyi, *Phys. Rev. B Condens. Matter Mater. Phys.* **2008**, *78*, 045107.
[256] A. P. Aslla-Quispe, R. H. Miwa, J. D. S. Guerra, *Phys. B: Condens. Matter.* **2021**, *615*, 413107.
[257] X. Chi, K. Rubi, A. Chaudhuri, L. M. Wong, X. Yu, C. Diao, A. Kumar, M. B. H. Breese, S. Wang, R. Mahendiran, A. Rusydi, *Phys. Rev. B* **2018**, *98*, 085152.
[258] A. Chaudhuri, K. Rubi, T. C. Asmara, X. Chi, X. J. Yu, R. Mahendiran, A. Rusydi, *Phys. Rev. B* **2018**, *98*, 165303.
[259] A. S. Bhalla, R. Guo, R. Roy, *Mater. Res. Innov.* **2000**, *4*, 3.
[260] B. Poojitha, K. Rubi, S. Sarkar, R. Mahendiran, T. Venkatesan, S. Saha, *Phys. Rev. Mater.* **2019**, *3*, 024412.
[261] M. Sahu, B. Ghosh, B. Joseph, A. K. Mishra, G. D. Mukherjee, *J. Chem. Phys.* **2024**, *161*, 094202.
[262] T. Takeda, A. Watanabe, *J. Phys. Soc. Jpn.* **1962**, *19*, 1742.
[263] R. Kumari, S. Kumari, E. Sharma, S. Kumari, J. Dalal, D. Padalia, *Opt. Mater.* **2023**, *143*, 114244.
[264] Y. Tsur, C. A. Randall, *High Temperature Corrosion and Materials Chemistry, High Temperature Corrosion and Materials Chemistry: Proceedings of the Per Kofstad Memorial Symposium* (Eds: P. Y. Hou, T. Marayama, M. J. McNallan, T. Narita, E. J. Opila, D. A. Shores), The Electrochemical Society, Inc., USA, **2000**.
[265] T. Okamatsu, H. Nishimura, N. Inoue, H. Sano, H. Takagi, *Key Eng. Mater.* **2010**, *301*.
[266] S. Bhaskar Reddy, K. Prasad Rao, M. S. Ramachandra Rao, *J. Alloys Compd.* **2011**, *509*, 1266.
[267] L. Li, M. Wang, D. Guo, R. Fu, Q. Meng, *J. Electroceram.* **2013**, *30*, 129.
[268] M. Arshad, W. Khan, M. Abushad, S. Mohanta, S. Husain, D. K. Shukla, A. Ansari, V. K. Chakradhary, *Mater. Res. Bull.* **2024**, *169*, 112504.
[269] L. Ben, L. Li, J. H. Harding, C. L. Freeman, D. C. Sinclair, *Open Ceram.* **2022**, *9*, 100250.
[270] X. Pu, J. Yang, T. Wang, S. Cheng, Q. Cao, J. Zhao, H. Chen, Y. Zhang, T. Xu, I. Tojiboyev, H. Salari, X. Li, *J. Energy Chem.* **2022**, *70*, 9.
[271] R. Wang, J. Wu, S. Wei, J. Zhu, M. Guo, Q. Zheng, M. Wei, S. Cheng, *J. Power Sources* **2022**, *544*, 231870.
[272] P. Wang, L. Hao, Z. Wang, Y. Wang, M. Guo, P. Zhang, *ACS Appl. Mater. Interfaces* **2020**, *12*, 49464.
[273] D. Y. Lu, *Solid State Ion.* **2015**, *276*, 98.
[274] Y. X. Li, X. Yao, X.-S. Wang, Y.-B. Hao, *Ceram. Int.* **2012**, *38* S29.
[275] D. Y. Lu, Y. Y. Peng, *J. Ceram. Soc. Jpn.* **2016**, *124*, 455.
[276] M. Cernea, M. Secu, R. Radu, P. Ganea, V. A. Surdu, R. Trusca, E. T. Vasile, E. C. Secu, *J. Alloys Compd.* **2021**, *878*, 160380.
[277] P. Wang, X. Huang, S. Luan, J. Zhao, B. Li, J. Yang, Z. Fu, X. Cao, L. Zhang, S. Yu, R. Sun, *J. Mater. Chem. C* **2024**, *12*, 13131.
[278] Z. Li, S. Yan, J. Xia, F. Cao, X. Chen, Y. X. Song, Y. Chen, Z. S. Lin, G. Wang, *Ceram. Int.* **2022**, *48*, 27439.
[279] J. Kim, T. Noh, S. Jeon, S. Park, H. Chun, H. Lee, *Ceram. Int.* **2012**, *38*, 6837.
[280] Z. Cai, L. Cheng, X. Huang, P. Wang, X. Fu, J. Yang, R. Sun, Z. Fu, X. Cao, L. Zhang, *Ceram. Int.* **2024**, *50*, 53744.
[281] S. P. Culver, V. Stepanov, M. Mecklenburg, S. Takahashi, R. L. Brutchey, *Chem. Commun.* **2014**, *50*, 3480.
[282] F. D. Morrison, D. C. Sinclair, A. R. West, *J. Am. Ceram. Soc.* **2001**, *84*, 531.
[283] E. J. Lee, J. Jeong, Y. H. Han, *Jpn. J. Appl. Phys., Part* **2004**, *43*, 8126.
[284] D. Y. Lu, S. Z. Cui, *J. Eur. Ceram. Soc.* **2014**, *34*, 2217.
[285] H. T. Langhammer, T. Müller, K. H. Felgner, H. P. Abicht, *J. Am. Ceram. Soc.* **2000**, *83*, 605.
[286] E. Mashkina, C. McCammon, F. Seifert, *J. Solid State Chem.* **2004**, *177*, 262.
[287] D. D. Han, D. Y. Lu, X. Y. Sun, *J. Alloys Compd.* **2013**, *576*, 24.
[288] Q. Sun, Q. Gu, K. Zhu, J. Wang, J. Qiu, *Ceram. Int.* **2016**, *42*, 3170.
[289] J. Chun, J. Kim, W. W. Lee, E. Jang, Y. Lee, K. Kim, W. J. Choi, W. Jo, W. Kim, B. S. Kang, *Ceram. Int.* **2024**, *50*, 42963.
[290] L. Xia, X. Liu, Z. Mao, Y. Cai, J. Zhu, J. Xie, W. Hu, *J. Materiomics* **2024**, *10*, 1117.
[291] H. Kishi, N. Kohzu, Y. Mizuno, Y. Iguchi, J. Sugino, H. Ohsato, T. Okuda, *Jpn. J. Appl. Phys.* **1999**, *38*, 5452.
[292] H. Kishi, Y. Mizuno, H. Chazono, *Jpn. J. Appl. Phys.* **2003**, *42*, 1.
[293] J. Jeong, E. J. Lee, Y. H. Han, *Jpn. J. Appl. Phys.* **2005**, *44*, 4047.
[294] J. Jeong, E. J. Lee, Y. H. Han, *Mater. Chem. Phys.* **2006**, *100*, 434.
[295] Y. Liu, A. R. West, *J. Eur. Ceram. Soc.* **2009**, *29*, 3249.

[296] D. Y. Lu, D. X. Guan, *Sci. Rep.* **2017**, *7*, 6125.
[297] V. Singh, A. A. Bhat, C. M. Mehare, S. J. Dhoble, *J. Electron. Mater.* **2024**, *53*, 4857.
[298] D. Y. Lu, X. L. Gao, S. Wang, *Results Phys.* **2019**, *12*, 585.
[299] F. A. Kröger, H. J. Vink, *Solid State Phys.* **1956**, *3*, 307.
[300] D. Lu, W. Cheng, X. Sun, Q. Liu, D. Li, Z. Li, *J. Raman Spectrosc.* **2014**, *45*, 963.
[301] D. Y. Lu, T. T. Liu, *J. Alloys Compd.* **2017**, *698*, 967.
[302] M. Marjanović, D. Dimitrijević, V. Paunović, Z. Prijić, *Serb. J. Electr. Eng.* **2014**, *11*, 35.
[303] W. H. Lee, W. A. Groen, H. Schreinemacher, D. Hennings, *J. Electroceram.* **2000**, *5*, 31.
[304] S. Sato, Y. Nakano, A. Sato, T. Nomura, *J. Eur. Ceram. Soc.* **1999**, *19*, 1061.
[305] X. Yang, Z. Fu, Y. Yang, C. Zhang, Z. Wu, T. Sheng, *J. Am. Ceram. Soc.* **2015**, *98*, 2595.
[306] D. K. Singh, J. Manam, *Ceram. Int.* **2018**, *44*, 10912.
[307] G. C. Yi, B. A. Block, G. M. Ford, B. W. Wessels, *Appl. Phys. Lett.* **1998**, *73*, 1625.
[308] H. X. Zhang, C. H. Kam, Y. Zhou, X. Q. Han, S. Buddhudu, Y. L. Lam, *Opt. Mater. 15*, 47.
[309] P. Ghosh, S. Sadhu, T. Sen, A. Patra, *Bull. Mater. Sci.* **2008**, *31*, 461.
[310] L. V. Maneeshya, P. V. Thomas, K. Joy, *Opt. Mater.* **2015**, *46*, 304.
[311] M. Vega, S. Fuentes, I. R. Martín, J. Llanos, *Mater. Res. Bull.* **2017**, *86*, 95.
[312] J. Zou, S. Hao, P. Gemeiner, N. Guiblin, O. Ibder, B. Dkhil, C. Paillard, *J. Mater. Chem. C* **2023**, *12*, 600.
[313] Y. Zhang, J. Hao, C. L. Mak, X. Wei, *Opt. Express* **2011**, *19*, 1824.
[314] M. T. Buscaglia, V. Buscaglia, P. Ghigna, M. Viviani, G. Spinolo, A. Testino, P. Nanni, *Phys. Chem. Chem. Phys.* **2004**, *6*, 3710.
[315] M. T. Buscaglia, M. Viviani, V. Buscaglia, C. Bottino, P. Nanni, *J. Am. Ceram. Soc.* **2002**, *85*, 1569.
[316] K. Takada, E. Chang, D. M. Smyth, *Rare Earth Additions to $BaTiO_3$, Advances in Ceramicsm*, Vol. *17* (Eds: J. B. Blum, W. R. Cannon), American Ceramic Society, **1986**, Westerville, OH, p. 147.
[317] L. Chen, X. Wei, X. Fu, *Trans. Nonferrous Met. Soc. China* **2012**, *22*, 1156.
[318] Y. A. Zulueta, F. Guerrero, Y. Leyet, J. Anglada-Rivera, R. L. González-Romero, J. J. Meléndez, *Phys. Status Solidi B Basic Res.* **2015**, *252*, 508.
[319] L. J. Clabel H, I. T. Awan, V. A. G. Rivera, I. C. Nogueira, M. A. Pereira-da-Silva, M. S. Li, S. O. Ferreira, E. Marega, *Appl. Surf. Sci.* **2019**, *493*, 982.
[320] J. L. Clabel H, I. T. Awan, G. Lozano, M. A. Pereira-Da-Silva, R. A. Romano, V. A. G. Rivera, S. O. Ferreira, E. Marega, *Phys. Chem. Chem. Phys.* **2020**, *22*, 15022.
[321] J. L. Clabel H, S. N. Nazrin, C. G. Lozano, M. Pereira da Silva, M. Siu Li, E. Marega, *Vacuum* **2021**, *194*, 110562.
[322] V. V. Mitić, Z. S. Nikolić, V. B. Pavlović, V. Paunović, M. Miljković, B. Jordović, L. j. Zivković, *J. Am. Ceram. Soc.* **2010**, *93*, 132.
[323] M. Cernea, C. E. Secu, B. S. Vasile, M. Secu, *Curr. Appl. Phys.* **2013**, *13*, 137.
[324] J. Wang, T. Zhang, R. Pan, Z. Ma, J. Wang, *Appl. Surf. Sci.* **2012**, *258*, 3283.
[325] J. Cao, J. Zhou, B. Li, M. Fu, R. L. Zong, *Key Eng. Mater.* **2007**, *561*, 336.
[326] Y. Liu, W. A. Pisarski, S. Zeng, C. Xu, Q. Yang, *Opt. Express* **2009**, *17*, 9089.
[327] A. García Murillo, F. J. Carrillo Romo, M. García Hernández, J. Ramírez Salgado, M. A. Domínguez Crespo, S. A. Palomares Sánchez, H. Terrones, *J. Solgel. Sci. Technol.* **2010**, *53*, 121.
[328] Y. Li, Y. Hao, X. Wang, X. Yao, *Ferroelectrics* **2010**, *407*, 134.
[329] G. Yao, X. Wang, Y. Yang, L. Li, *J. Am. Ceram. Soc.* **2010**, *93*, 1697.
[330] T. Tan, Y. Han, C. Zhang, Y. Ji, F. Zhang, Q. Chen, C. Wang, Y. Mei, P. Xu, L. Li, Y. zhu, J. Wang, *J. Lumin.* **2017**, *183*, 448.
[331] A. Kumari, V. K. Rai, K. Kumar, *Spectrochim. Acta A Mol. Biomol. Spectrosc.* **2014**, *127*, 98.
[332] D. W. Hahn, Y. H. Han, *Jpn. J. Appl. Phys.* **2009**, *48*, 111406.
[333] J. Amami, D. Hreniak, Y. Guyot, R. Pazik, C. Goutaudier, G. Boulon, M. Ayadi, W. Strek, *J. Lumin.* **2006**, *383*, 119.
[334] A. Alshoaibi, M. B. Kanoun, B. Ul Haq, S. AlFaify, S. Goumri-Said, *Results Phys* **2020**, *18*, 103257.
[335] M. Ganguly, S. K. Rout, C. W. Ahn, I. W. Kim, M. Kar, *Ceram. Int.* **2013**, *39*, 9511.
[336] V. Paunović, L. Živković, V. Mitić, *Sci. Sinter.* **2010**, *42*, 69.
[337] R. Zhang, J. F. Li, D. Viehland, *J. Am. Ceram. Soc.* **2004**, *87*, 864.
[338] P. W. Rehrig, S. E. Park, S. Trolier-McKinstry, G. L. Messing, B. Jones, T. R. Shrout, *J. Appl. Phys.* **1999**, *86*, 1657.
[339] D. Y. Lu, X. Y. Sun, M. Toda, *Jpn. J. Appl. Phys.* **2006**, *45*, 8782.

**Takeshi Nakagawa** is an Associate Staff Scientist at the Center for High Pressure Science & Technology Advanced Research (HPSTAR) in Beijing, China. He received his Ph.D. in chemistry from the Faculty of Science, University of Durham, UK in 2010. He has been working closely with leading research institutions and universities in Japan, China, and Europe. His primary research interest is focused on the investigation of physical properties of carbon-rich organic molecular solids, combining synthetic chemistry and high-pressure science to search for new properties and improve their functionality.

**Melita Menelaou** is an Assistant Professor in the Department of Mechanical and Materials Science and Engineering at the Cyprus University of Technology in Limassol. She received her Ph.D. in chemical engineering from the Aristotle University of Thessaloniki, Greece in 2009. She has collaborated with leading research institutions in Asia and Europe, including the WPI-AIMR at Tohoku University in Japan, the Central European Institute of Technology in the Czech Republic, the University of Barcelona in Spain, and her alma mater, the Aristotle University of Thessaloniki. Dr. Menelaou specializes in the synthesis and research of (advanced) nano/materials.

**Martina Vrankić** is a Senior Research Associate at the Ruđer Bošković Institute, Zagreb, Croatia. She received her Ph.D. in inorganic and structural chemistry from the Faculty of Natural Sciences, University of Zagreb, Croatia in 2014. She has worked closely with WPI-AIMR at Tohoku University in Japan, Bergische Universität Wuppertal in Germany, and HPSTAR-Beijing in PR China. Her research interests encompass powder X-ray diffraction under both ambient and non-ambient conditions to clarify the structure-property link in functional oxides, doped ceramics, and hybrid organic-inorganic molecular ferroelectrics.